Structural and Catalytic Analysis of Gold-Palladium Composite Nanoalloys

D I S S E R T A T I O N

zur Erlangung des akademischen Grades
d o c t o r r e r u m n a t u r a l i u m
(Dr. rer. nat.)
im Fach Chemie
eingereicht an der

Mathematisch-Naturwissenschaftlichen Fakultät I
der Humboldt-Universität zu Berlin
von

Dipl. Chem. Julian Winfried Kaiser

Präsident der Humboldt-Universität zu Berlin:
Prof. Dr. Jan-Hendrik Olbertz

Dekan der Mathematisch-Naturwissenschaftlichen Fakultät:
Prof. Stefan Hecht, PhD

Gutachter: 1. Prof. Dr. Matthias Ballauff

2. Prof. Dr. Klaus Rademann

Eingereicht am: 25.09.2012
Tag der mündlichen Prüfung: 31.01.2013

"It is not too less time we have, but too much time not used."

Lucius Annaeus Seneca

to my brothers Peter and Theo

Abstract

The present thesis describes studies on gold-palladium nanoalloys which have been synthesized and stabilized in spherical polyelectrolyte brushes (SPB) as composite particles (AuPd@SPB). Different compositions with atomistic ratios of 25:75, 50:50, and 75:25 (Au:Pd) have been synthesized as well as neat Au@SPB and Pd@SPB nanoparticles. Detailed structural analyses have been performed by high resolution transmission electron microscopy (HR-TEM) and extended X-ray absorption fine structure (EXAFS) spectroscopy. The AuPd@SPB nanoalloys appear as well-defined facetted metallic crystals in a size range of 1 – 3 nm. No phase segregation or core-shell structure has been observed neither by HR-TEM nor by EXAFS.

By HR-TEM analysis some steps appear at the edge of the facetted nanoalloys atall Au:Pd ratios that have been synthesized. A semi-quantitative analysis has been applied to calculate an index for the frequency of surface defects for these nanoalloys. It is found that the AuPd@SPB particles with an atomistic ratio of 75:25 (Au:Pd) contain the highest number of surface defects,as derived fromthis semi-quantitative analysis.

The atomistic arrangement of gold and palladium in the nanoalloys has beenanalyzedby EXAFS measurements.It turned out that there are slight enrichments of palladium at the surface of the particles which is attended by an increasing gradient of gold towards the center of the nanoalloys. This effect is significant for the alloy compositions of 25 molar % and 50 molar % of gold. For the alloy system with 75 molar % of gold this effect is negligible. In this case the atomistic arrangement is equal to a homogeneous randomly mixed bimetallic nanoalloy. Furthermore palladium atoms of the species Pd^{2+} are observed among metallic palladium in the bimetallic nanoalloys and the palladium nanoparticles by EXAFS spectroscopy.

In addition, the EXAFS analysis gives evidence of shortening of interatomic distances in metallic nanoparticles. To gain further insight about the impact of the stabilizing system on the metal nanoparticles,gold nanoparticles with different sizes (1.8 – 2.7 nm) have been synthesized inside SPBand analyzed by EXAFS. In this case the lattice parameter depends linear on the inverse particles size which accords

well with the literature for metal nanoparticles stabilized by different supporting systems. However, it turned out that the slope of this linear correlationdependson the type of the stabilizer system. Thus, an influence of the stabilizer system on the metal nanoparticles is found.

Thenanoalloys have been applied as catalysts for the reduction of 4-nitrophenol by sodium borohydride which has been chosen as model reaction to study the catalytic behavior of metal nanoparticles. The AuPd@SPB nanoalloys show an enhanced catalytic performance compared to the neat metal nanoparticles, *e.g.*, Au@SPB, Pd@SPB, and Pt@SPB. A maximum in the catalytic activity is observed for a nanoalloy system with the atomistic ratio of 75:25 (Au:Pd). The catalytic behavior of this alloy composition has been studied in terms of the Langmuir-Hinshelwood model which has been developed in previous studies on SPB stabilized metal nanoparticles.[1] Furthermore a delay time appears for the applied model reaction in the case of the AuPd@SPB nanoalloys which accords well with previous results of Au@SPB nanoparticles where this induction period is related to a surface restructuring at the catalyst.[1]

Moreover, to study the impact of the SPB stabilizing system on catalysis, support-free gold nanoparticles which have been generated by laser ablation were applied as catalyst for the previous described model reaction. The catalytic behavior of these gold nanoparticles is analyzed in terms of the Langmuir-Hinshelwood model and compared to SPB stabilized metal nanoparticles. A central result of this investigation is that the polymeric stabilizer does not influence the catalytic activity of the metal nanoparticles but the induction period.

Zusammenfassung

Die vorliegende Arbeitbefasst sich mit Gold-Palladium Nanolegierungen, die in sphärischen Polyelektrolytbürsten (SPB) als Komposite (AuPd@SPB) synthetisiert und stabilisiert wurden. Die Aufgabe bestand darin Nanolegierungen unterschiedlicher Zusammensetzungenmit dem atomaren Verhältnissen von 25:75, 50:50 und 75:25 (Au:Pd), ebenso wie Au@SPB und Pd@SPB Nanopartikel zu synthetisieren. Die Partikel wurdenmit Hilfe hochauflösender Elektronenmikroskopie (HR-TEM) und Röntgenabsorptionsspektroskopie zur kantennahen Feinstruktur (extended X-ray absorption fine structure,EXAFS)analysiert. Die AuPd@SPB Nanolegierungen erscheinen dabei als klare, facettierte metallische Kristalle in der Größenordnung von 1 – 3 nm. Weder durch HR-TEM noch mittels EXAFS wurde eine Phasenseparation oder eine Kern-Schale Struktur festgestellt.

Durch die HR-TEM Analyse wurden bei allen hier synthetisierten Au:Pd Zusammensetzungen Stufen an den Partikelkanten sichtbar. Die Berechnung eines Indices zur Häufigkeit dieser Oberflächendefekte konnte durch die Anwendung einer semi-quantitativen Analyse durchgeführt werden. Hierbei stellte sich heraus, dass die AuPd@SPB Nanopartikel mit einer Zusammensetzung von 75:25 (Au:Pd) den höchsten Index bezüglich der Oberflächendefekte beinhalten.

Die atomare Anordnung der Gold und Palladium Atome in den Nanolegierungen wurde durch EXAFS Messungen bestimmt. Dabei stellte sich eine geringfügige Anreicherung von Palladium auf der Partikeloberfläche heraus.Dies gehtmit einem erhöhten Gold-Konzentrationsgradienten zum Partikelmittelpunkteinher. Dieser Effekt ist für die Legierungen mit einem Goldanteil von 25 mol-% und 50 mol-% signifikant. Für die Nanolegierungen mit einem Goldanteil von 75 mol-% ist der Effekt jedoch vernachlässigbar. In diesem Fall ist die Atomanordnung in der Legierung annähernd der einer homogenen, statistisch gemischten Legierung. Zusätzlich wurde durch EXAFS Messungen neben metallischem Palladium auch Palladium im Zustand Pd^{2+} für alle Nanolegierungen und den Palladiumnanopartikeln festgestellt.

Des Weiteren konnte eine Verringerung des interatomaren Abstands durch EXAFS Messungen in Metallnanopartikeln nachgewiesen werden. Dieses Phänomen eignet

sich um den Einfluss despolymeren Trägersystems auf die metallischen Nanopartikel zu untersuchen. Dafür wurden Au@SPB Nanopartikel unterschiedlicher Größe (1,8 – 2,7 nm) synthetisiert und mittels EXAFS analysiert. Dabei konnte eine lineare Beziehung zwischen dem Netzebenenabstand und der inversen Partikelgröße hergestellt werden.Diese stimmt mit Resultaten aus der Literatur bezüglich metallischer Nanopartikel mit verschiedenartigenStabilisatoren überein. Abhängig von der Wahl des Stabilisatorsystems wurden hierbei im Vergleich mit Literaturdaten verschiedene Steigungen für die lineare Abhängigkeit gefunden.

Die hergestellten Nanolegierungen wurden als Katalysatoren für die Reduktion von 4-Nitrophenol mit Natriumborhydrid verwendet, welche als Modellreaktion zum Vergleich des katalytischen Verhaltens verschiedener Nanopartikel gewählt wurde. Diese AuPd@SPB Nanolegierungen zeichneten sich durch eine erhöhte katalytische Effizienz im Vergleich zu monometallischen Nanopartikeln, wie zum Beispiel Au@SPB, Pd@SPB und Pt@SPB aus. Die katalytische Aktivität der Nanolegierungen erreicht bei einer Zusammensetzung von 75:25 (Au:Pd) ein Maximum. Die Nanolegierung dieser Zusammensetzung wurde mit Hilfe des Langmuir-Hinshelwood Modells näher untersucht, wobei ähnliche Resultate wie bei früheren Arbeiten im Bereich SPB stabilisierter Nanopartikel erzielt wurden.[1] Ferner trat bei der Katalyse der angewendeten Modellreaktion mit Nanolegierungen eine Verzögerung des Reaktionsbeginns auf. Dieses Verhalten steht in Analogie zu früheren Ergebnissen an Au@SPB Nanopartikeln bei denen diese Verzögerungszeit mit einer Oberflächenrestrukturierung der Katalysatoroberfläche in Verbindung gebracht wurde.[1]

Zusätzlich wurde der Einfluss des SPB Stabilisators auf die Katalyse untersucht. Hierfür wurden, durch Laserablation hergestellte,stabilisator-freie Goldnanopartikel als Katalysatoren für die beschriebene Modellreaktion verwendet. Anschließend fand eine Untersuchung des katalytischen Verhaltensmit Hilfe des Langmuir-Hinshelwood Modells statt,welche mit den Ergebnissen der SPB stabilisierten Nanopartikeln verglichen wurde. Hierbei stellte sich heraus, dass der Stabilisator keinen Einfluss auf die katalytische Aktivität hat. Jedoch konnte ein Einfluss des Stabilisators auf die Induktionszeit, die vor Reaktionsbeginn auftritt, festgestellt werden.

Table of Contents

1. Introduction

Since a decade, nanoparticles have drawn increasing attention from researchers due to high variety of properties, compositions and structures.[2,3,4,5,6,7] Nanoparticles are in the size range of a few nanometers.[3] They fill the gap between atoms or molecules and bulk materials.[3]Nowadays, these particles are used in many new technologies in the field of physics, chemistry, material science and electrical and chemical engineering.[8]Metal nanoparticles constitute anew research area because of two main effects: The quantum-size effect and the high surface-to-volume ratio.[2,3,4,5,6]These properties make them suitable for broad technological applications like sensors,[9] optical devices,[10] microelectronics,[11] data storage[12] and catalysis.[7,11,13,14,15,16,17,18,19,20]

1.1 Bimetallic Nanoparticles

Bimetallic nanoparticles consisting of two different elements are of greater interest compared to monometallic nanoparticles.[7,21,22,23]For example, CoPt core-shellnanoalloys are used as biomedical magnetic sensors and ultrahigh-density memory devices, due to their superparamagnetic properties.[7] The properties of bimetallic nanoalloys rest on their atomistic arrangement andelectronic structure.[7,21]Depending on the composition, the synthesis route, as well as the reaction conditions, different structural arrangements of the two metals are accessible for bimetallic nanoalloys.[7,24] In principle, core-shell structures, randomly mixed alloys and segregated particles are the main classifications of bimetallic nanoalloy mixing patterns. Furthermore formations of intermediates of these structures are possible.[7] In addition, stabilizing systems likepolymer matrix, activated carbon ormetal oxide playa rule on the arrangement of elements in nanoalloys.[15]

The most common methods for structural characterization of bimetallic nanoalloys are diffraction (*e.g.*, X-ray diffraction), microscopy (especially transmission electron microscopy), X-ray spectroscopy (*e.g.*, X-ray absorption spectroscopy and X-ray photoelectron spectroscopy), and energy-disperse X-ray

microanalysis.[7]Determination of the chemical composition and degree of ordering of bimetallic nanoalloys is also possible byUV-Vis spectroscopy due to its sensitivity to the surface plasmon resonance, especially for noble metal nanoalloys.[7]In addition, high resolution transmission electron microscopy (HR-TEM) is a powerful method to determine the morphology of metal nanoparticles.[25,26]The difference in the contrast of gold and palladium in the HR-TEM is high enough to discriminate between core-shell structure and random mixed alloys.[7,26,27]Furthermore extended X-ray absorption fine structure (EXAFS) spectroscopy can be used to evaluate the atomistic arrangement of bimetallic nanoalloys.[7,28] For this method, the absorption edges of the two elements must differ at least by 1500 eV to avoid overlapping of absorption signals.[29,30] In contrast to HR-TEM, also slight enrichments of elements and the oxidation state of the metal atoms can be detected by EXAFS. HR-TEM and EXAFS are important methods in this work to analyze the atomistic arrangement of gold and palladium in AuPd nanoalloys and will be explained in more detail in the Theory part of this thesis.

1.2 Synthesis of Mono- and Bimetallic Nanoparticles

Various synthesis routes have been developed for the fabrication of nanoparticles and bimetallic nanoalloys.[7]In principle, two methods are applied:[8] The top-down approach, where bulk material is subdivided,*e.g.*, by colloid mills,[31,32] evaporation techniques[33,34,35,36] or laser ablation,[37,38,39,40,41,42]and the bottom up approach, where nanoparticles are synthesized, starting from molecules, metal atoms or precursors.[8]Normally, the particles aresynthesized in presence of additives whichstabilize the nanoparticles.[3,4,6]However, for the fabrication of gold nanoparticles by laser ablation in aqueous environment, for example, the system is stable without any additives due to the presence of OH^- ions which adsorb onto the surface of the particles and cause electrostatic repulsion between the nanoparticles.[43]

1.3 Stabilization of Mono- and Bimetallic Nanoparticles

The most common polymeric stabilizing materials are dendrimers,[44,45] microgels,[46]and polyelectrolyte brushes.[47]Spherical polyelectrolyte brushes(SPB)have been successfully applied in previous work to synthesize and stabilizenoble metal nanoparticles like gold,[48] platinum,[49] palladium, silver,[50] and bimetallic nanoalloys, *e.g.*, AuPt[51]in the size range of 1 – 4 nm.[47,48,49,51,52,53,54]Figure 1 shows the synthesis and stabilization of AuPt nanoalloys inSPB.[53]

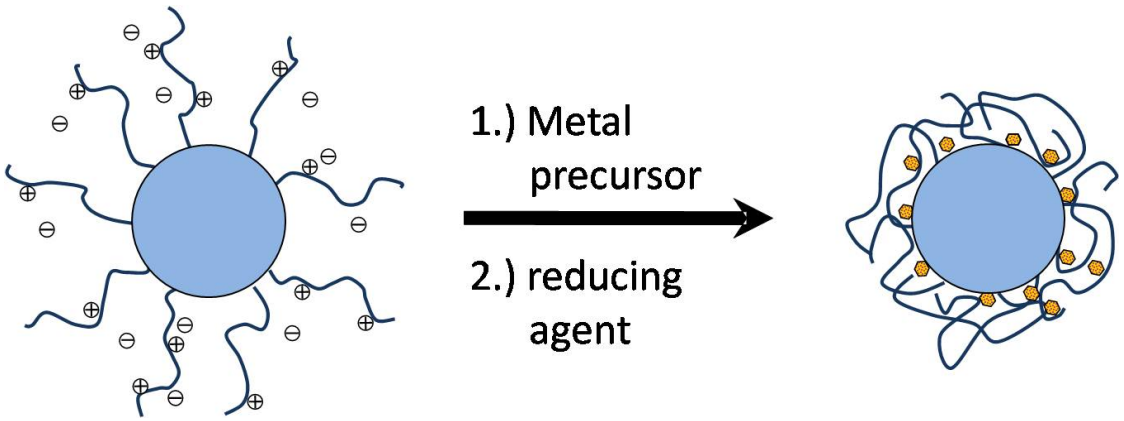

Figure 1: Schematic representation of the formation of AuPt nanoalloys immobilized in SPB. The positively charged polyelectrolyte chains and the counterions are represented by "+" and "-" in the scheme, respectively.[53]

The SPB systemconsists of a polystyrene core, onto which polyelectrolyte chains are polymerized.[55] The polyelectrolyte chains contain either positive or negative charges, depending on the monomers which were used. Positive brush systems are synthesized by cationic polyelectrolytes, *e.g.*,PAEMH (poly(2-aminoethyl methacrylate hydrochloride)), whereas negative brush systems contain anionic polyelectrolytes, such as PSS (poly(styrene sulfonate)).[47,49,53,55]For the synthesis of metal nanoparticles in SPBs, a metal salt is first added to an aqueous SPB suspension as precursor. The metal salt ions are immobilized in the SPB carrier system as counterions electrostatically. Subsequently, a reducing agent (sodium borohydride) is added to the suspension, which causes the reduction of the immobilized metal precursors tothe respective metal nanoparticles.[53]

Metal nanoparticles stabilized in SPB show high colloidal stability.[47,53,54]The SPB

system does not block the surface of the nanoparticles.[47] Thus, these carrier systems are used for catalytic applications.[48,49]In the present study, spherical polyelectrolyte brushes are employed as stabilizing system for the synthesis of bimetallic AuPd nanoalloys.

1.4 Bimetallic Nanoparticles as Catalysts

A main application of bimetallic nanoalloys is their use as catalysts.[15,56] They offer a high surface-to-volume ratio and show enhanced catalytic activity compared to monometallic nanoparticles.[7,21]The effect of improved catalysis may lay in changes of the electronic states of the two elements in bimetallic nanoalloys[13] and in the atomistic arrangement of the two elements in bimetallic catalysts.[21]An overview of the catalytic applications of bimetallic AuPd nanoalloys as catalysts and some insight on the promotional effect of the two different elements is given in the following paragraphs:

Bimetallic AuPd nanoalloys show high catalytic performance in hydrogenation reactions, *e.g.*, the hydrogenation of buta-1,3-diene,[57]styrene[28] and 3-hexyn-1-ol.[58] The enhanced catalytic activity seems to be caused by the modified electronic structure due to high differences in the atomic electron configurations and electronegativities compared to their neat metals.[7] Another application for Au_{core}-Pd_{shell} nanoalloys is the hydrodechlorination of trichlorethene.[59] The reason for the enhanced catalytic activity is not understood yet, but might be due to electronic or geometric effects.[7]

In addition, AuPd alloys are used for degradation reactions, *e.g.*, the decomposition of phenol,[60] N_2O[61] and *p*-nitroaniline.[62] For the latter, it turned out that the sum of the rate constants of Au and Pd nanoparticles accord well with the rate constant of AuPd nanoalloys stabilized on silicon nanowires.[62]

Furthermore, the acetylene cyclotrimerization to benzene is improved by AuPd alloys compared to Pd catalysts due to reduced hydrocarbon decomposition and enhanced desorption of benzene.[63,64,65] Especially for Au_{core}-Pd_{shell} nanoalloys, the

generation of this promotion effect is assumed to be caused by a small number of Au surface atoms breaking the arrangement of Pd atoms at the surface of the catalyst.[65]

Bimetallic AuPd nanoparticles stabilized on different support materials show high efficiency in the synthesis of hydrogen peroxide from hydrogen and oxygen.[66,67,68] For the use of neat Pd catalysts, a competitive reaction is known which leads to the formation of water by the dissociation of dioxygen.[68] This dissociation process is blocked by Au atoms at the surface of AuPd nanoalloys which leads to enhanced catalytic activity.[21,68]

AuPd nanoalloys are widely used for oxidation reactions, *e.g.*, the oxidation of ethanol,[69]various aromatic alcohols,[70,71,72] toluene,[73] propene[73] and propanediol.[74] Recently, Hutchings and co-workers published the high activity and selectivity of AuPd nanoalloys for the oxidative dehydrogenation of toluene and alcohols.[13,27] Analysis by high-resolution scanning transmission electron microscopy indicates enrichments of Au in the core and Pd at the surface of the AuPd nanoalloys.[27] Au surface atoms that change the electronic structure at the surface are supposed to generate the promoting effect to high catalytic performance in this case.[21]

In studies on the synthesis of vinyl acetate, Chen and Goodman[75,76,77] investigated the promotional effect of Au in AuPd alloy-catalysts compared to neat Pd catalysts by combination of different analyzing methods, *e.g.*, low energy ion scattering spectroscopy, high resolution electron energy loss spectroscopy and infrared reflection adsorption spectroscopy.[75] It is found that Au breaks the arrangement of Pd atoms in contiguous Pd surface into isolated Pd monomers on the alloy surface.[75] Thus, much more active sites of Pd are available compared to monometallic Pd catalysts.[21,75] In the synthesis of vinyl acetate, CO is a byproduct that is known to poison Pd catalysts.[75] The adsorption site of AuPd alloys for CO adsorption has been analyzed in previous studies.[64,78,79,80,81,82,83] It turned out that the bonding strength of CO is much weaker for Pd monomer sites than for contiguous Pd surfaces which results in less catalyst poisoning by CO in the case of AuPd alloys.[75,76,77,84] In addition, for the synthesis of vinyl acetate by ethylene the contiguous Pd sites are active for ethylene decomposition.[75]The application

ofAuPd nanoalloys for this catalytic reaction leads to hindrance of the degradation of ethylene due to the absence of Pd-bridging to vicinal Pd atoms which results in higher selectivity and catalytic activity of AuPd alloys.[75,77]

From previous publications, discussed in the paragraphs above, it is clear that the adsorption of substrates on the catalyst shows a high impact on the catalytic performance. Concerning the adsorption behavior and catalytic activity, the properties of different catalysts are only comparable by working at the same experimental conditions. Thus, values which are measured in catalytic tests should always be normalized to the total surface of the catalyst in the reaction mixture. Furthermore comparison of different catalysts is much easier by employing a benchmark reaction.

Recently, the reduction of 4-nitrophenol by sodium borohydride in presence of metal nanoparticles as catalyst has been chosen as a benchmark reaction and has been applied to metal nanoparticles which are stabilized in SPB.[1,48,49]This reaction is easy to monitor by UV-Vis absorption at mild conditions, *e.g.*, it takes place at room temperature in an aqueous environment. No side reactions are observed and no reaction takes place without the presence of a catalyst.[48,49] Thus, the reduction of 4-nitrophenol to 4-aminophenol by sodium borohydride in the presence of metal nanoparticles has been chosen as model reaction in previous studies.[1] Detailed explanation of this model reaction has been published in a tutorial review in 2012 (see Ref.[1]).The nanoparticles which have been synthesized in SPB show narrow size distributions.[48,49] Thus, parameters which show high impact on the reaction kinetics like the surface area of the nanoparticles are known with high precision.[48] Therefore the model reaction can be studied with high accuracy in the field of heterogeneous catalysis.[1]In the UV-Vis spectra of this model reaction a linear dependence of $\ln(A/A_0)$ on the reaction time occurs where the apparent rate constant k_{app} of the reaction is directly obtained. It is found in previous work that $k_{app}$is sensitive to variations of the concentration of reactants.[48,49] These different k_{app} values can be fitted by a kinetic model where the catalytic activity and the adsorption behavior of the substrates is analyzed with high precision.[1]Moreover, an induction period is observed in the UV-Vis spectra. In studies on SPB stabilized gold nanoparticles a correlation between this delay time and a restructuring of the surface of the metal nanoparticle is found.[48,49] This surface restructuring is necessary to

activate the metal surface of the catalyst for the reaction.[1] The mechanism of this model reaction and the adsorption of its substrates onto the catalyst are explained in more detail in the Theory part of this thesis.

2. Objectives of this Thesis

The objectiveof this thesis is to synthesize bimetallic gold-palladium (AuPd) nanoalloys in spherical polyelectrolyte brushes (SPB) and totest the catalytic behavior. Palladium has been chosen due to its efficiency to catalyze C-C couplings,*e.g.*, the Suzuki cross-coupling reaction.[85]Gold is one of the most studied nanoparticlesapplied in catalysis in the recent years.[14,86] By employing SPB as stabilizing system, small bimetallic nanoalloys of every atomistic ratio can be synthesized.[51,53]The AuPd nanoalloys have been prepared in different Au:Pd ratios. The SPB stabilizer is the same carrier system as used in previous studies for neat metal nanoparticles and AuPt nanoalloys.[47,48,49,53,54] Thus, the nanoalloys of this work are stabilized by similar conditions of previous studies which allows a thorough comparison between the different systems.

For these synthesized AuPdnanoalloys structural investigationswill beperformed. By these structural investigations special emphasis is put on the atomistic arrangement of gold and palladium in the bimetallic metal nanoparticles.High resolution transmission microscopy (HR-TEM) and extended X-ray absorption fine structure (EXAFS) spectroscopy are chosen as the most important methodsto study the structure of AuPd nanoalloysin this work. By HR-TEM, the morphology, size distribution and lattice pattern of metal nanoparticles will be analyzed. Furthermore, by fast Fourier transformed (FFT) HR-TEM analysis of AuPd nanoalloys, the lattice parameter of the metal particles can be evaluated. The second main analyzing method will be EXAFS. In contrast to HR-TEM which allows the analysis of single particles this method gives average information on the system. Special emphasis is put on the evaluation of the average atomistic environment of Au and Pd in AuPd nanoalloys by EXAFS which is the key to determine the arrangement of the two different elements in bimetallic nanoalloys.

In thenext part of this thesis the catalytic behavior of AuPd nanoalloys will be investigated in detail. Bimetallic nanoalloys are generally known to be better catalysts than their neat metal nanoparticles. However, the reason for this enhanced catalytic activity is not fully understood yet.[21]The reduction of 4-nitrophenol by sodium borohydride will be applied as model reaction to gain deeper knowledge about the

catalytic behavior of AuPd@SPB nanoalloys. To compare this alloy system to its neat metal nanoparticles, palladium nanoparticles have to be synthesized in SPBand kinetic analysis will be performed. Results of the catalytic analysis of gold nanoparticles from previous work[48,49] will be compared as well.The focus is put on the mechanism of the heterogeneous catalytic reaction in the presence of AuPd nanoalloys.

In a next step it should be clarified whether the stabilizer influences the catalytic behavior in particular for the reduction of 4-nitrophenol. To analyze possible effects of the stabilizer system on the catalytic behavior of these nanoparticles, support-free gold nanoparticles will be analyzed. These gold nanoparticles have been generated by laser ablation without the addition of stabilizers which is described in more detail in the Theory part of this thesis. Previous described model reaction will be applied to those unsupported nanoparticles and compared to the catalytic behavior of SPB stabilized metal nanoparticles[48] and bimetallic nanoalloys.

3. Theory

3.1 Nanoparticles

An extremely high surface-to-volume ratio is supposed to be responsible for the unique behavior of nanoparticles, *e.g.*, their enhanced catalytic activity.[3,4,5,6,87]The ratio of surface atoms compared to bulk atoms rises enormously with decreasing particle size. For a spherical cluster of 1 µm diameter, for example, 1 % of the atoms are located at the surface of the cluster. In the case of 10 nm diameter, 25 % of all atoms are surface atoms containing low coordination numbers respectively. When the particle is approximately 1 nm or even less, the number of atoms located at the surface of the particlereaches up to 100 %.[5] This fact is illustrated inFigure 2 where the mean coordination number (CN) is illustrated as a function of the inverse particle radius ($N^{-1/3}$) and the total number of atoms (N).[6]

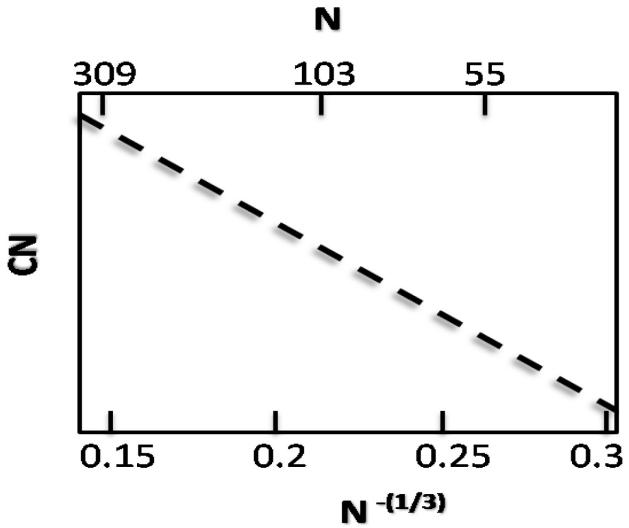

Figure 2:Dependence of the mean coordination number (CN) on the inverse particle size of nanoparticles.[6]

Figure 2 demonstrates that, especially for nanoparticles in the size of less than 10 nm, the surface-to-volume ratio increases extremely by decrease of the particle size. Therefore all effects those appear due to the surface properties of nanoparticles, *e.g.*, the enhanced catalytic activity, need to be normalized by the

surface area, if different nanoparticles are compared to each other.[1,48,49,51,53]

3.1.1 Stabilization of Nanoparticles

One disadvantage of nanoparticles is their tendency to agglomerate.Thus, stabilizers are employed to prevent nanoparticles from agglomeration.[3,4,6]In general, three different methods are known to stabilize nanoparticles: i) immobilization, ii) sterical hindrance and iii) electrostatic repulsion.[4,88]

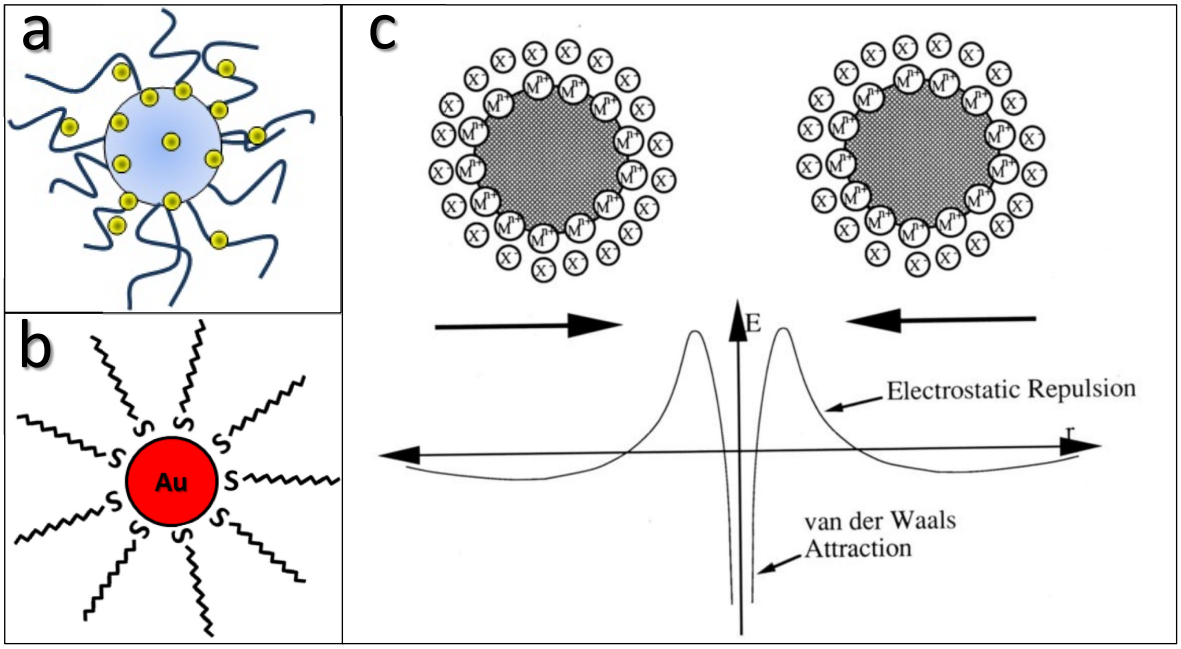

Figure 3: Stabilization of metal nanoparticles by immobilization on SPB (yellow spheres represent gold nanoparticles) (a),[47] sterical hindrance by thiols (b)[4] and electrostatic repulsion (c).[89]The forces in the case of electrostatic repulsion are illustrated in c, where attractive van der Waals forces are outweighed by repulsive electrostatic forces.[89]Permission from:Nanoparticles: From Theory to Application, John S. Bradley,Günter Schmid,Dmitri V. Talapin,Elena V.Shevchenko,Horst Weller,Copyright © 2004 Wiley-VCH Verlag GmbH & Co. KGaA

In Figure 3ananoparticles are immobilized in spherical polyelectrolyte brushes.[47] This approach is chosen in the present work. Another way of stabilization, namely sterical hindrance is achieved by grafting stabilizers, *e.g.* ligands, onto the surface of thenanoparticles (see Figure 3b).[4] These supports can form strong covalent bonds like thiol bonds to gold (Figure 3b) or non-covalent bonds as usualin the case of many polymeric stabilizers. These stabilizers keep a certain distance between the particles by forming a shell around the nanoparticle.[4]Often these stabilizers contain

ions, leading to repulsion between nanoparticles to other particles if neighboringnanoparticles approach. In this case, sterical hindrance and electrostatic repulsion are applied at once as a mixture of both (sterical and electrostatic)approach.[4,89]Usually electrostatic repulsion is achieved by adding small ionized molecules and ligands. These stabilizers are located at the surface of the nanoparticles and, thus, increase the charge density of the latter.[88]In contrast to sterical hindrance, these additives are often small molecules with the only task to create charges at the surface of the nanoparticles.An example of this kind of stabilization is shown in Figure 3c, where aqueous chlorauric acid has been reduced by sodium citrate.[89] The gold nanoparticle is surrounded by citrate which finally leads to electrical double layers at the surface of the particles. This surface charge causes electrostatic repulsion.[89] The physical forces of electrostatic repulsion and van der Waals attraction at very small distances are illustrated in the scheme at the bottom of Figure 3c.[89] In contrast to these approaches,surface charged metal nanoparticle in aqueous suspension without additional support materials can be fabricated, *e.g.*,by laser ablation,[43] which is explained in the following chapter.

3.1.2 Support-Free Gold Nanoparticles by Laser Ablation

The techniques to produce support-free nanoparticles are usually achieved by disintegrating bulk material. In this approach, colloid mills,[31,32] chemical vapor deposition and sputtering[34,35,36,72] are the standard methods. In addition, the production of metal and ceramic nanoparticles by laser ablation has been investigated as a useful tool[90] and reached already industrial application. In this technique, a target, existing of bulk material, *e.g.*, a gold foilis located at the bottom of a vial, filled with a liquid, *e.g.*, water or organic solvent. Subsequently, a pulsed laser beam is focused on the target material. The laser pulse penetrates the material surface, converts it to plasma and evaporates fragments of the target into the liquid environment.In the liquid, the ablated material cools down and condensates to nanoparticles.[40,91]The experimental setup for this method is shown in Figure 4a.[41]

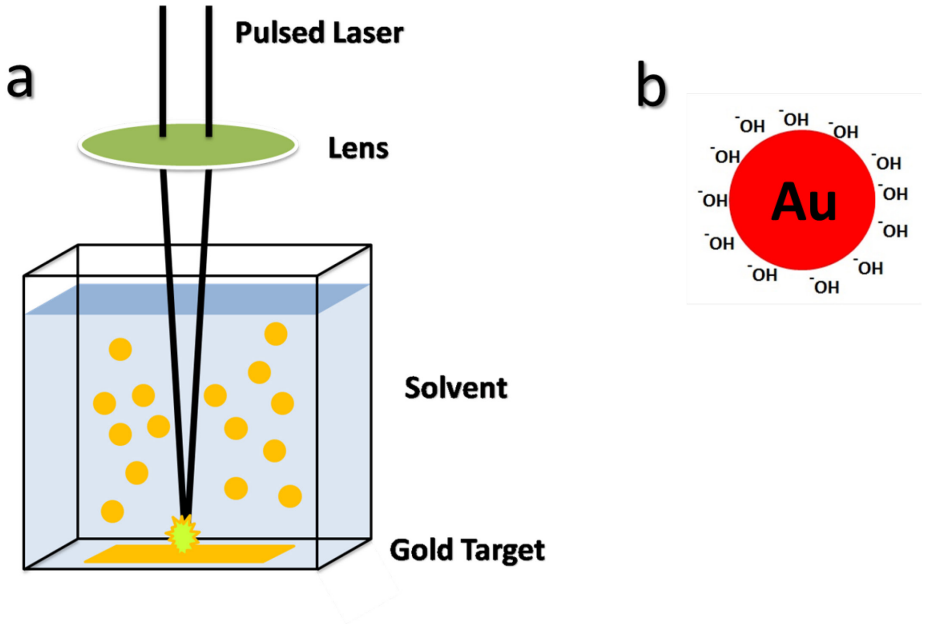

Figure 4: Scheme of the process of liquid laser ablation with the experimental setup (a)[41] and illustration of an unsupported metal nanoparticle (b).[43]

In principle, any type of metal can be used as target material in this technique. This method is also called rapid nanomaterial prototyping due to fast production of nanoparticles in a one-step formation.[92] The metal nanoparticles, prepared by laser ablation in liquids are negatively charged. Thus, suspensions containing these metal nanoparticles remain stable due to electrostatic repulsion. Recently, it turned out that,*e.g.*, in aqueous suspensions, hydroxide ions are attached at the surface of the nanoparticles which cause this negative charge.[43] Thus, no additional stabilizersneed to be added in this case. Thus, the particles can be fabricated with high purity.[93,94] Theseunsupported nanoparticles can be further applied as efficient catalysts which will be discussed in the Results and Discussion part of this thesis.

3.1.3 Bimetallic Nanoalloys

Nanoalloys differ in a lot of properties compared to their bulk alloys.[7] An alloy system of gold and platinum, for example, is not mixable in every ratio in the bulk phase. By generating nanoalloys of these two metals, alloy mixing has been observed in any ratio.[51] In their use as catalysts, it turned out that nanoalloys are much better catalysts than monometallic nanoparticles.[7,15] In the case of gold and

palladium, the bimetallic system is much more stable than the neat gold and palladium nanoparticles.[13]For most of the applications of nanoparticles, the arrangement of the two different elements in bimetallic nanoalloys shows significant impact. In general, there exist four structuralpossibilities regarding the pattern of bimetallic nanoalloys: Core-shell structure (a), subclusters (b), statistically mixed (c) and multipleshell (d) alloys. These mixing patterns are illustrated in Figure 5.[7]

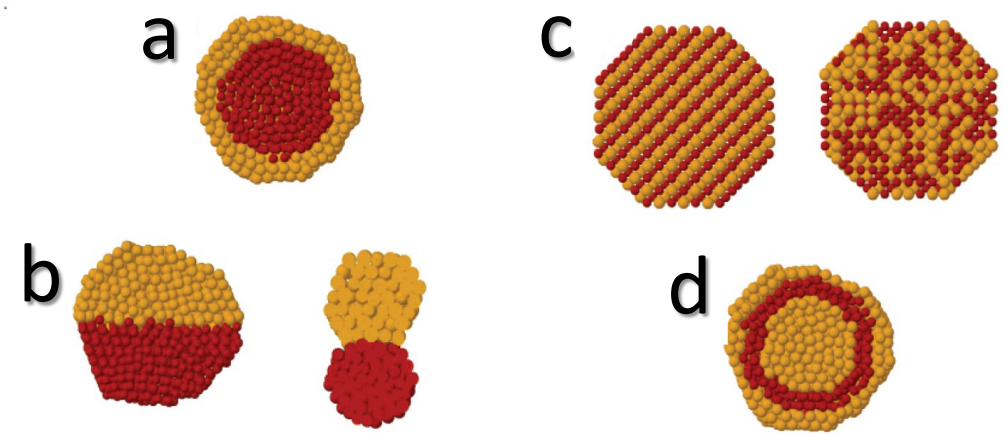

Figure 5: Scheme of different alloy mixing patterns of two metals A (yellow) and B (red): core-shell particle (a), segregated subclusters (b), mixed (c) and three shell nanoalloy (d).[7]Reprinted with permission from R. Ferrando, J. Jellinek and R. L. Johnston, Chem. Rev., 2008, 108, 845-910. Copyright ©2008 American Chemical Society.

Figure 5a shows a typical core-shell type of bimetallic nanoalloys. One type of metal forms a core, while the other one surrounds the core in an outer shell. Slight mixing at the interface of the two element phases is possible.[7]Due to the synthesis route and conditions, core-shell particles or randomly mixed alloys,*e.g.*, in the case of AuPd alloys are observed.[7,15] If the elements do not mix well, phase separation will occur. There may be particles which are not completely separated but form a small interface between the two metals as it is shown on the right hand side in Figure 5b, or sharing a larger interface while the two metals are still segregated (Figure 5b, left). Another type of structure is the complete mixing of both metals by ordered patterns (Figure 5c left) or randomly mixed alloys (Figure 5c right). Another possibility of atomistic arrangements in bimetallic nanoalloys is an onion-like structure (Figure 5d). Here one metal (*A*) forms a core, while metal *B* surrounds the core. Finally, the particle is again covered by *A*, forming the outer shell.[7]The reasons for atomistic arrangements in the cluster are manifold and usually depend on the reaction

conditions. However, if there are huge differences in the elemental properties of the two elements, general assumptions explain the type of alloy formation, as follows:[7] The most important aspect is the relative strength of the bonds between the elements *A* and *B* and between the same elements (*A*-*A* and *B*-*B* bonds). If *A*-*B* bonds are stronger than *A*-*A* or *B*-*B* bonds, the alloy will tend to statistical alloy mixing. Otherwise, segregation will be favored, if *A*-*A* and *B*-*B* bonds are similarly strong and stronger than *A*-*B* bonds. In the case that,*e.g.*,*A*-*A* bonds are stronger than *B*-*B* bonds, the element *A* will form the core of a core-shell structure with a shell containing *B*. Especially in the case of core-shell particles, the surface energy of bulk elements of *A* and *B* are important, due to the fact that the element containing the lower surface energy will be located at the surface of the alloy. Finally, the addition of stabilizers and substrates, whichbind or adsorb on the surface of the particle, will have an impact on which element tends to be located at the surface. If strong bonds between the stabilizer and the surface atoms are formed, the element which forms stronger bonds to the stabilizer will be favored as surface atom.[7]

3.2 CatalysiswithNeat Metal Nanoparticles and Bimetallic Nanoalloys

One of the most important applications of metal nanoparticles is their use as catalysts.[2,86,95]Gold for example is catalytically inactive in the bulk phase, but is applied as efficient catalyst in the size of approximately 10 nm or smaller.[3,4,6]Thus, gold nanoparticles have been used in different catalytic reactions,[96]*e.g.*, hydrogenations,[97,98,99] oxidations,[100,101,102] epoxidations[103] and C-C coupling reaction.[104]However, focusing on C-C bond formation in organic synthesis, palladium is one of the most important catalysts.[96]Palladium isused as catalyst, *e.g.*, for Heck-,Suzuki- and Sonogashira-couplings.[96]

In the last decade, alloy nanoparticles have attracted more and more interest.[7]The reasons therefore are various designs for different metal compositions, atomic ordering and different arrangement of elements in the nanoalloy.[7] In catalytic applications, these nanoalloys have the advantage of anextremely high catalytic activity compared to their neat metal nanoparticles. For systematic studies on the catalytic behavior of neat metal nanoparticles and nanoalloys, a well-studied model

reaction should be used to compare different types of catalysts. The reduction of 4-nitrophenol to 4-aminophenol by sodium borohydride is such a model reaction that can be monitored by UV-Vis absorptionprecisely.[1] Furthermore, no side reaction is observed in the case of this reaction and mild conditions, like room temperature and water as solvent,are warranted.[1] In previous studies on gold and palladium nanoparticles this model reaction has been applied to describe the adsorption behavior of the reactants onto the surface of the catalyst.[48,49] The reaction kinetics of this model reactionis explained in the following chapter. The catalytic behavior of gold-palladium nanoalloys is analyzed by this model reaction as well and discussedin the Results and Discussion part (chapter 4.2.1) ofthe present work.

3.2.1 Langmuir-Hinshelwood Kinetics

For the model reaction which has been chosen in the present work, the reduction of 4-nitrophenol, catalysis takes place after the two substrates in the liquid phase adsorb on the surface of the catalyst which is in a solid phase.[1] Therefore it is classified to the field of heterogeneous catalysis.[105] The reaction mechanism for this model reaction hypothesizes that both substrates have to adsorb on the surface of the catalyst in a first step prior to the reaction.[1,48] This adsorption process can be described by the Langmuir adsorption isotherm which implicates the following assumptions: It describes the equilibrium of adsorption and desorption of substrates. All active sites are equal and can only be occupied by one molecule. The surface coverage of the catalyst and the presence of vicinal occupied active sites do not influence the adsorption process.[105]

The Langmuir isotherm is expressed by following equation:[105]

$$\theta = \frac{K[A]}{1 + K[A]} \qquad (1)$$

where θ is the surface coverage, K is the adsorption equilibrium constant and [A] represents the concentration of the adsorbate, free in solution.Following the adsorption process the reaction takes place. The reaction rate$r$for the conversion of two molecules$A$ and Bwhich takes place on the surface of the catalystis given with

the frame of the Langmuir-Hinshelwood model as follows:[105]

$$r = kS\theta_A\theta_B = \frac{kS(K_A[A])(K_B[B])}{(1 + K_A[A] + K_B[B])^2} \quad (2)$$

where *r* is the reaction rate, *k* is the kinetic constant of the reaction oftwo molecules*A* and *B*, *S* is the total surface area of the catalyst, K_A and K_B are the adsorption constants of *A* and *B*, respectively and [*A*] and [*B*] represent the concentration of *A* and *B* in the reaction mixture. θ_A and θ_B is the surface coverage of the surface of the catalyst by *A* and *B*, respectively.

If the concentration of the starting material *B* is high in the reaction mixture, a pseudo first order reaction can be assumed. Then equation(1) and (2) can be modified as follows:[105]

$$r = \frac{kS(K_A[A])(K_B[B])}{(1 + K_A[A] + K_B[B])^2} = k_{app}\,[A] \quad (3)$$

where k_{app} is the apparent rate constant of the catalytic reaction.To apply this model to metallic nanoparticles as catalysts, irregularities of the metal surfaces have to be considered.[49] Therefore the Langmuir isotherm is modified by the Freundlich[106] ansatz. By implication empirical Freundlich exponents the Langmuir-Freundlich adsorption isotherm[107] is obtained. Thus, equation (3)is modified toequation(4):[105]

$$k_{app}\,[A] = \frac{kS(K_A[A])^n(K_B[B])^m}{(1 + (K_A[A])^n + (K_B[B])^m)^2} \quad (4)$$

where *n* and *m* are the Freundlich exponents for reactants *A* and *B*, respectively. These exponents describe the difference to ideal systems due to the heterogeneity of the sorbents.

This model is further simplified by an excess of one of the reactants, *e.g.*, *B* which leads to a pseudo first order reaction. Thus, the Langmuir-Hinshelwood model is

finally described by modification of equation (4) with $\frac{d[A]}{dt} = -k_{app}[A]$ to following equation:

$$k_{app} = \frac{kSK_A^n[A]^{1-n}(K_B[B])^m}{(1+(K_A[A])^n+(K_B[B])^m)^2} \quad (5)$$

The Langmuir-Hinshelwood model has been recently applied to the reduction of 4-nitrophenol by sodium borohydride in presence of metal nanoparticles.[1,48,49]

3.2.2 Induction Period

For the reduction of 4-nitrophenol by sodium borohydride in presence of SPB stabilized gold nanoparticles as catalysts, an induction period appears after mixing all reactants.[48,49] This period is in the range of several seconds up to several minutes.An induction time wasobserved by many groups independently.[108,109]Zhou *et al*.[110] found similar induction periods in a different reaction employing gold nanoparticles as catalysts. This phenomenon has been explained by the restructuring of the surface of the nanoparticle by the reactants.[110]In the past, restructuring of metal surface has already been known by gas phase reactions in catalysis.[111]The reason for this process lays in the so-called reconstruction of the surfaces of the catalyst containing no adsobate. Once, a critical coverage of the surface is reached, the adsorbates cause surface restructuring at the metal surface.[112,113,114,115,116,117,118,119]This surface restructuringinduces fluctuation of active sites on the surfaces and therefore activates the catalyst for the reaction.[120] Recently, it turned out that the inverse induction period at neat metal nanoparticles stabilized by SPB is traced back to the surface reconstruction on the surface of the catalyst caused by adsorbed reactants.[1,48,49]However, two aspects remain to be clarified:

i) How do nanoparticles without support act,concerning surface restructuring and
ii) how will the change from neat metal nanoparticles to bimetallic nanoalloys influence this phenomenon. These two aspects are discussed in the results and discussion part of this thesis.

3.3 High Resolution - Transmission Electron Microscopy

Transmission electron microscopy (TEM) is one of the most common characterization methods for metal nanoparticles.[7] Recently, high resolution TEM (HR-TEM) offers novel opportunities for structural analysis in nanoscience.[121] The high resolution nowadays has been achieved by great developments in aberration corrections in the last decades.[122]Spherical aberration, chromatic aberration and astigmatism show the highest impact on the resolution limit.[123]The correction of spherical aberration has improved the resolution to the sub-angstrom scale.[121] The aberration and its correction will be explained below. Chromatic aberration is due to the energy distribution of electrons. However, this aberration is negligible for thin specimens as it is the case for metallic nanoparticles. Another aberration, namely astigmatism, arises due to the impossibility of perfectly cylindrically symmetrically polepices that are used to focus the electron beam. Nowadays these aberrations are corrected by stigmators that correct the astigmatism.[123]

Spherical aberration has been the main aberration that limited the resolution of electron microscopy in the last decades.[122] Spherical aberration is caused by inhomogeneously acting electron lenses. The high angle electrons are too strongly bent back towards the center of the electron beam as shown in Figure 6a.[121] As a consequence, a point object is imaged as a broad disk-like dot at the focus plane.[121,122,123,124] The radius (*r*)of this diskscales linear with the spherical aberration constant (C_s) and α^3(where α is the angle of electron rays before crossing the lens) which is shown in Figure 6a[121] in a schematic fashion.

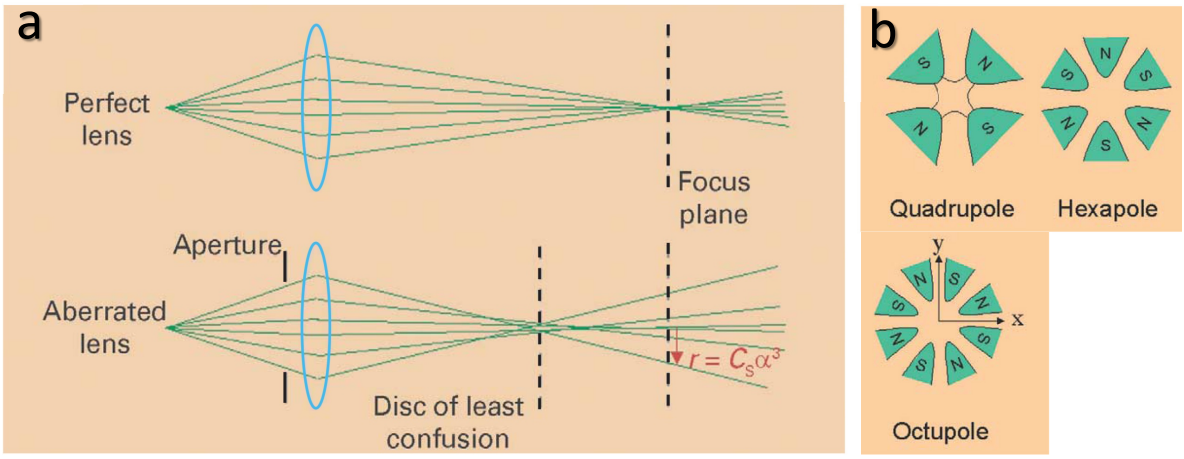

Figure 6: Comparison of a perfect lensand a spherical aberrated lens (a). Scheme of quatrupole, hexapole and octupole lenses(b).[121] Reprinted from:A. Bleloch and A. Lupini, Materials Today, 2004, 7, 42-48., with permission from Elsevier, Copyright © 2004 Elsevier.

The correction of this spherical aberration is achieved by C_s – correction arrays by employing quadrupole-octupole orhexapole correctors which are displayed in Figure 6b.[121] These lenses are breaking the rotational symmetry of commonly used lenses and cause negative spherical aberration. Finally, the spherical aberration and the negative spherical aberration result in C_s– corrected electron beams where sub-angstrom resolution is achievable. This high resolution by C_s– correction revolutionized structural analysis of nanomaterials by HR-TEM.[121,122,124]

3.4 Electronic Structure of Bimetallic Nanoalloys

The electronic properties of bimetallic nanoalloys are determined by theoretical calculations of the density of states (DOS).[125]The DOS is related to the model of atom orbitals and molecule orbitals. In this model the bond of two atoms is explained by the formation of two molecule orbitals by two single atom orbitals. The two molecule orbitals exist of one orbital on a higher energy level which is the lowest unoccupied molecule orbital (LUMO) and another orbital in a lower energy level than the two original atom orbitals which is the highest occupied molecule orbital (HOMO). Starting from this model with two atoms, the number of atoms are increased dramatically, as it is the case in metal bulk materials. As a consequence the discrete

molecule orbitals overlap to energy bands.[126]Electronic properties of nanoparticles constitute an intermediate situation of single molecules and bulk materials as it is illustrated by the DOS in Figure 7.[3]

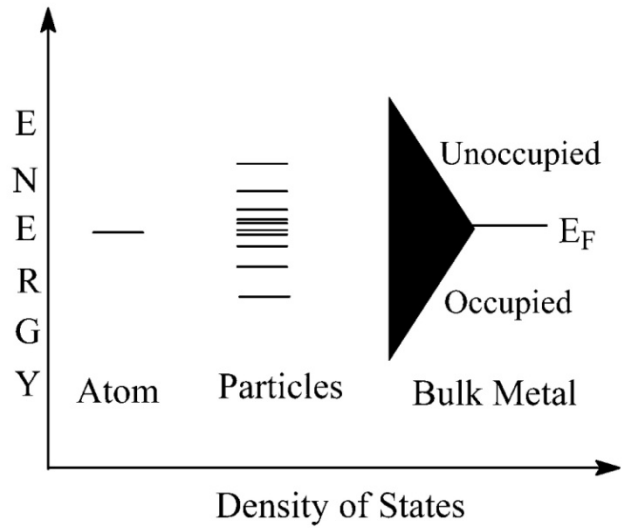

Figure 7: Energy levels of atoms, nanoparticles and bulk material. The energy level E_F denotes the Fermi energy.[3]Reprintedwith permission from: S. K. Ghosh and T. Pal, Chem. Rev., 2007, 107, 4797-4862. Copyright © 2007 American Chemical Society.

By DOS calculations of bimetallic nanoalloys certain energies of the energy band are obtained depending on the types of elements and composition. The local DOS of each element and the total DOS of both elements in an alloy composition change by variation of the atomistic ratio of both elements. In the case of CuPd random alloys for example the energy *d*-bands of the nanoalloys move closer to the Fermi energy and show wider peaks with increasing palladium concentration. This behavior is assumed to relate to the hybridization of copper and palladium energy bands in the alloy mixture.[125]

3.5 Extended X-Ray Absorption Fine Structure Analysis of Gold Nanoparticles and Bimetallic Nanoalloys

Extended X-ray absorption fine structure (EXAFS) spectroscopy and high resolution transmission electron microscopy (HR-TEM) are the most important methods for structural analysis in the present work. By HR-TEM it is possible to discriminate between core-shell structures and random alloy structure.[87] However, the evaluation of slight enrichments of different types of atoms and the detection of the oxidation state of the metal atoms is impossible by HR-TEM analysis.Therefore EXAFS is the method of choice for the structure determination of gold-palladium nanoalloys[28] and analysis of lattice parameters of gold nanoparticles[127] in the present study. This method is atom-specific and sensitive to the arrangement of atoms.[29] The environment of the analyzed element, *e.g.*, coordination number, bond distances and type of neighbor element, is available by the evaluation of the acquired EXAFS spectra.[128] Measurements are performed on a high number of particles. Therefore this method shows average results of the analyzed system.[29,30,128]Further information about EXAFS to clarify the structure of bimetallic nanoalloys is shown in following chapters. The EXAFS-equation[29] is shown and explained in the Experimental and Data Processing part in chapter 6.7.

3.5.1 Basics of EXAFS

X-ray absorption spectroscopy (XAS)offers element specific analysis by the absorption of X-rays at specific absorption energies depending on the type of element.A typical example of an absorption spectrum is displayed inFigure 8. It shows three regions: The pre edge region below the absorption edge, the region near to the absorption edge and the region above, where an oscillation can be clearly seen.[29]The latter region is the so-called EXAFS region and is the most important one in this thesis.

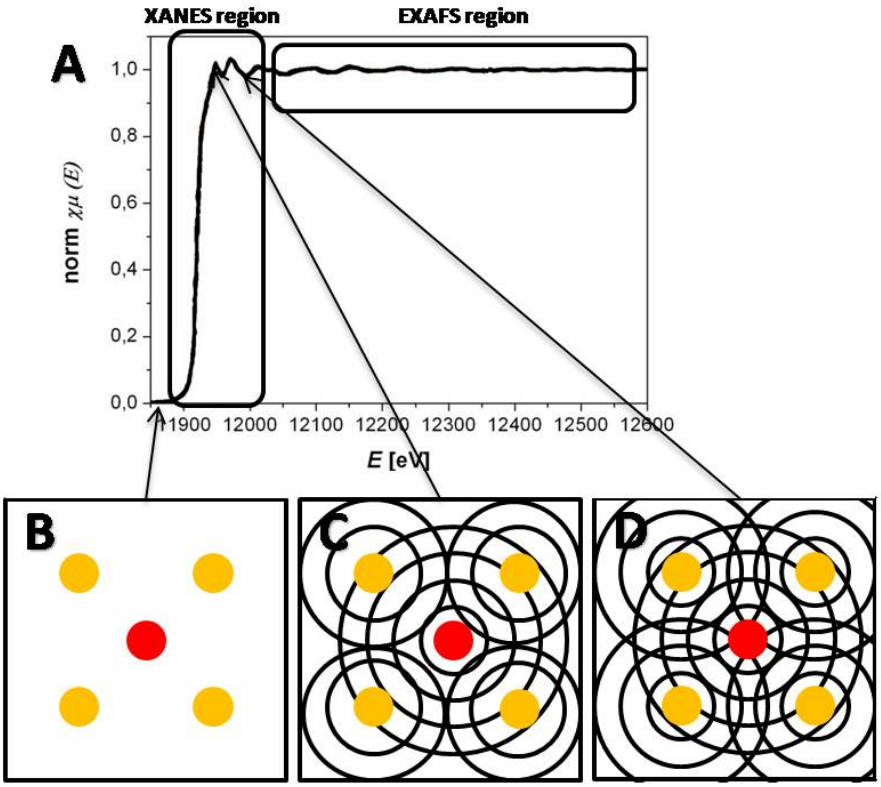

Figure 8: A) Absorption spectrum of gold nanoparticles at the Au-L_3 absorption edge showing typical regions of EXAFS and XANES. B) Red: absorbing element; yellow: rescattering neighbor atoms. No absorption occurs below the absorption edge. C)Constructive interference of absorber and rescattering neighbor causes maxima in the absorption spectrum.D) Destructive interference of absorber and rescattering neighbor causes minima in the spectrum.[29]

The absorption process is based on the photoelectric effect: The element absorbs a photon at a certain energy of the absorption edge and an electron of the inner orbital of the absorbing element is emitted. This electron is backscattered at neighbor atoms. Due to this effect, depending on the photon energy, constructive and destructive interference of electron waves between the absorbing atom and the backscattering atom appears as oscillations in the EXAFS region.[29,30] A scheme of this phenomenon is shown in Figure 8.

The photoelectric effect causes the absorption signal of the transmitting X-ray beam. The hole caused by the emitted electron,*e.g.*,in the K-shell of an atom can be filled by another electron of a higher shell, *e.g.*, the L-shell, by photon emission. Therefore it is possible to collect a fluorescence signal caused by the emitted photon as well. The analysis of the emitted fluorescence is compulsory for example for too thick samples,

where no transmission is achievable or too diluted samples, causing a too week transmission signal.[29,30,128]

3.5.2 Structural Analysis of Nanoalloys

Recently, it has been emphasized that the arrangement of gold and palladium in bimetallic AuPd nanoalloys can be well determined by EXAFS analysis.[28,72,129,130,131,132,133,134,135,136,137] In the literature evaluation of atomistic arrangements in bimetallic nanoalloys, *e.g.*, core-shell structure and randomly mixed alloy structure is performed by analysis on the coordination numbers (CN) of gold and palladium respectively.[28,72,129,130,131,132,133,134,135,136,137]Gold and palladium show face centered cubic (fcc) crystal lattice. Thus, the CN of both metals in bulk phase is 12.[28]In the case of nanoparticles, containing a high number of surface atoms, the average CN determined by EXAFS decreases with decreasing particle size due to an increase of low coordinating surface atoms. The CN for metal nanoparticles with particle size of 7 nm, for example, is decreased to approximately 9. For those with 1.5 nm size the CN is approximately 7.[138]

The atomistic arrangement of gold and palladium in AuPd@SPB composite nanoalloys has been analyzed by following general rules[28] for bimetallic nanoparticles consisting of the two metals Me1 and Me2:

If $N_{Me1\text{-}Me2}$ is low and the value of $N_{Me1\text{-}Me1}$ is close to 12 which is close to N_{total} (the sum of $N_{Me1\text{-}Me1}$ and $N_{Me1\text{-}Me2}$), most of the absorbing elements (Me1) form Me1-Me1 bonds. Therefore it is obvious that the first metal Me1 forms a core cluster inside the particle with approximately no inclusion of the second metal Me2. Consequentially, measurements of the absorption edge of the second element would contribute with high values of $N_{Me2\text{-}Me2}$ close to N_{total} (the sum of $N_{Me2\text{-}Me2}$ and $N_{Me2\text{-}Me1}$) at this absorption edge and low values for $N_{Me2\text{-}Me1}$. Furthermore N_{total} for this element will be much less than 12, indicating a high presence at the surface of theparticles for this element. In this case the structure can be predicted as a typical $Me1_{core}$-$Me2_{shell}$ structure.

Another scenario would contain N_{total} numbers lower than 12 for both elements, close to the values of $N_{Me1\text{-}Me1}$ at the Me1-absorption edge and $N_{Me2\text{-}Me2}$ at the Me2-absorption edge, respectively. In addition, values of $N_{Me1\text{-}Me2}$ and $N_{Me2\text{-}Me1}$ would be close to zero. This indicates that monometallic clusters of Me1 and Me2 are present and no metal mixing appears in the system.

Finally, in the case of typical randomly mixed alloy structures, the N_{total} values at both absorption edges would be similar. Additionally, a lot of Me1-Me2 bond would be present, resulting in high $N_{Me1\text{-}Me2}$ and $N_{Me2\text{-}Me1}$ values, respectively. As a rule for a strict random alloy structure, $N_{Me1\text{-}Me1}$ and $N_{Me1\text{-}Me2}$ has to be equal to the atomistic ratio of elements in the alloy. For example, for bimetallic alloys of 75 % Me1 and 25 % Me2, the ratio of $N_{Me1\text{-}Me1}$: $N_{Me1\text{-}Me2}$ has to be 75:25. Derivations of this rule tend to result in irregularities of the strictly random mixture of the alloy system.[28,72,129,131,132,136,139]

3.5.3 Lattice Contraction of Gold Nanoparticles

Contraction of lattice parameters for small gold particles is one special behavior that distinguishes nanoparticles from bulk material. In 1985 Balerna *et al.*[127] reported EXAFS studies on lattice parameters of gold nano clusters with different diameters in the range of 1.1 – 6.0 nm. An increase of lattice contraction has been found with decreasing particle size. A linear dependence of inverse particle size and lattice contraction has been identified which is shown in Figure 9.[127]

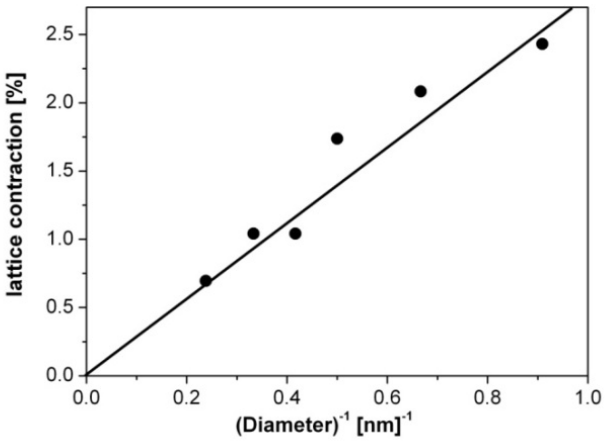

Figure 9: Dependence of the lattice contraction on the inverse particle size evaluated by EXAFS measurements. The solid line represents a surface tension of 3.5 N/m.[127]Reprinted from: A. Balerna, E. Bernieri, P. Picozzi, A. Reale, S. Santucci, E. Burattini and S. Mobilio, Surf. Sci., 1985, 156, 206-213.., with permission from Elsevier, Copyright © 1985 Elsevier.

Lattice contraction has been observed not only for small nanoparticles but also for thin metal films[140] which are often made of noble metals layers like gold, produced by sputtering gold on a glass surface.[141] A significant change in the lattice parameter measured by XRD measurements is reported for thin gold films less than 20 nm thickness.[141,142]To calculate the surface tension of metal nanoparticles, measurements about the lattice parameter is a well-known possibility.[127,143] Nanda *et al*.[34]produced a series of nanoparticles with different sizes, mainly gold nanoparticles, by evaporation. Free metal nanoparticles without polymeric stabilizers or carbon support are prepared by this approach where a linear correlation between the reciprocal of particle size and the lattice contraction was found. Furthermore, surface energies and surface tension were calculated. Both thermodynamicparameters were significant higher than that for bulk materials.[34,36,144,145,146,147,148] Xie *et al*.[149] developed a surface-to-volume depending ansatz to confirm Nanda's experimental results theoretically.[149] As there is a direct correlation ofinverse particle sizes and the surface-to-volume fraction, a lot of properties show this correlation.[6]A linear dependence between inverse particles size and surface energy was hard to find.[149]Furthermore the influence of stabilizers and support materials can play a role to physical parameters as for instance bond length shortening.[150] In the present study EXAFS is elected as the method of choice to evaluate the Au-Au bond length of gold nanoparticles which are stabilized on polymeric supportand compare it to different particle sizes and different particle supports reported in the literature.

4. Results and Discussion

4.1 Synthesis and Characterization of Gold-Palladium Nanoalloys in Spherical Polyelectrolyte Brushes

The task of this work is the synthesis and characterization of bimetallic AuPd nanoalloys using spherical polyelectrolyte brushes (SPB) as carrier system. This stabilizer system consists of a polystyrene core onto which polyelectrolyte chains are polymerized, which is shown in Figure 10in a schematic fashion. The polystyrene core contains a diameter of approximately 50 nm.The polyelectrolyte brushesare synthesized by using 2-aminoehtylmethacrylate hydrochloride (AEMH) and show an average thickness of 190 nm. This SPB is a cationic brush, where chloride is located between the polyelectrolyte chains as counterion.

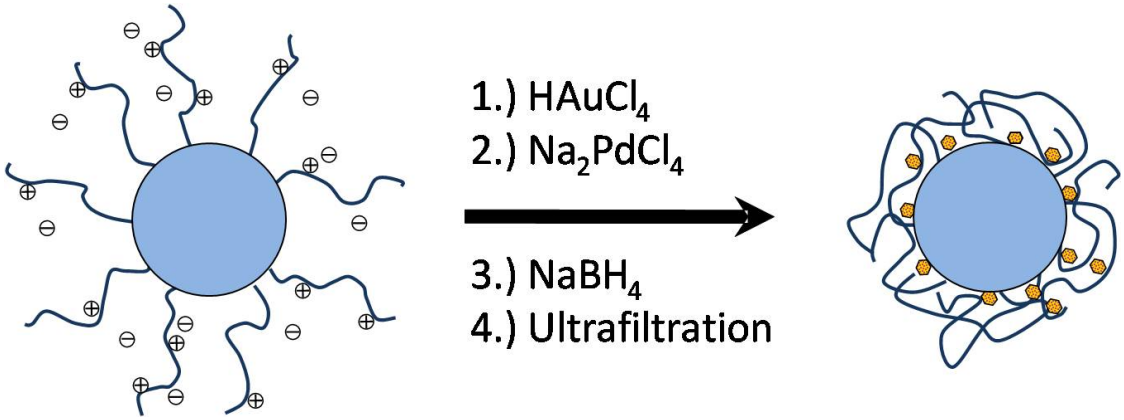

Figure 10: Scheme of the synthesis of AuPd nanoalloys in SPB.

The synthesis of AuPd nanoalloys is shown in the scheme of Figure 10 as follows: In a first step, solutions of$HAuCl_4$ and Na_2PdCl_4 are added slowly to an aqueous SPB suspension. The noble metal salts are immobilized into the polyelectrolyte chains by an ion exchange with the counterion chloride. In a second step, the reduction agent $NaBH_4$ is added to the suspension, which reduces the immobilized metal salts to bimetallic nanoalloys. Finally, the AuPd@SPB system is purified by ultrafiltration with Millipore water. The ratio between gold and palladium is adjusted by the molar ratio of the metal salts for gold and palladium at the first step of the synthesis. The nanoparticles are immobilized in the SPB stabilizerwhich can possibly be related to an interaction between the cationic polyelectrolyte chains and a negative charge of

the metal nanoparticles.[47,53]In this work, nanoalloys of 25:75, 50:50, and 75:25 molar ratios of Au:Pd have been synthesized. In addition, neat gold and palladium nanoparticles were fabricated. In this case, only one of the two noble metal salts ($HAuCl_4$ or Na_2PdCl_4) is added to the SPB suspension and reduced by $NaBH_4$. First analyses were made by transmission electron microscopy (TEM). The metal nanoparticles are observed as black dots in the TEM micrographs while the polystyrene core is visible as a large grey sphere. The polyelectrolyte chains collapse during the dryingprocess of the specimen preparation for the TEM measurement and thus, cannot be seen by TEM. Representative TEM images of the AuPd nanoalloy samples and the neat gold and palladium nanoparticles are shown in Figure 11together with their size distribution evaluated from TEM images.

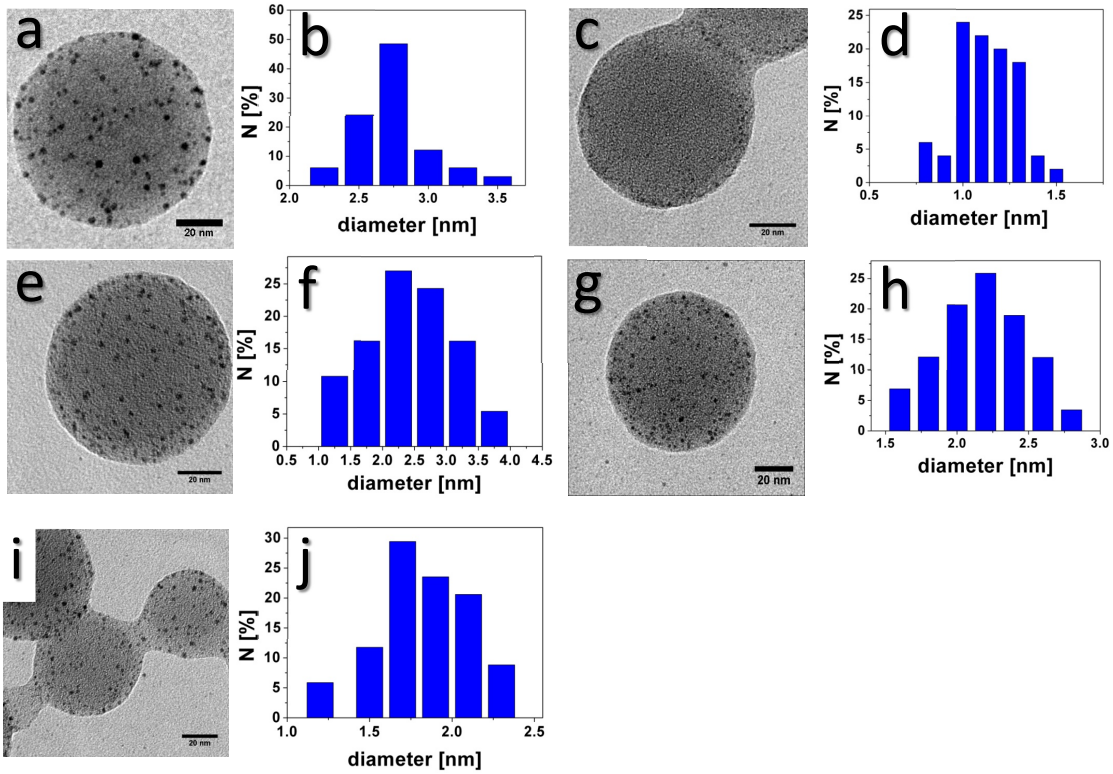

Figure 11: TEM micrographs of Au (a), $Au_{75}Pd_{25}$ (e), $Au_{50}Pd_{50}$ (g), $Au_{25}Pd_{75}$ (i) and Pd (c) nanoparticles stabilized in SPB. The size distribution is shown in the histograms (b, d, f, h, j) beside the TEM images.

The results of Figure 11 confirm the successful generation of metal nanoparticles in SPB. No coagulation of nanoparticles occurs. The particles are observed with a relatively narrow size distribution in all cases. The composition dependence in the

average diameter of the different AuPd nanoalloy compositions and their neat metal nanoparticles are shown in Figure 12.

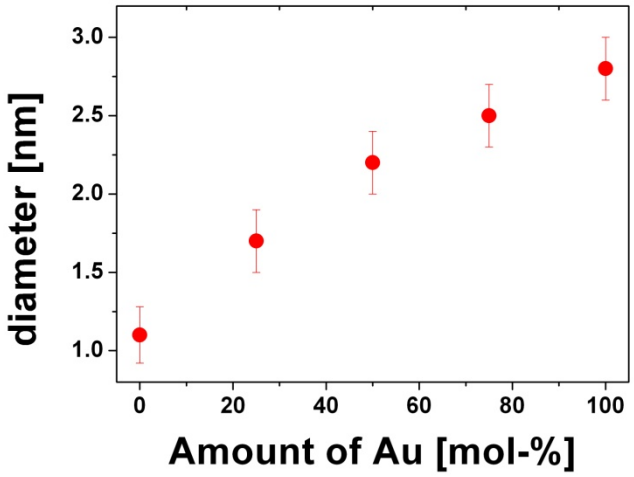

Figure 12: Dependence of the particle diameter for different AuPd@SPB compositions and the amount of gold in the particle.[Phys. Chem. Chem. Phys., 2012, 14, 6487-6495.] - Reproduced by permission of the PCCP Owner Societies.

Gold and palladium nanoparticles are observed with diameters of 2.8 ± 0.2 nm and 1.1 ± 0.2 nm, respectively. The particle diameters of the different AuPd nanoalloy compositions show values between those of gold and palladium nanoparticles. It is found that the particle size increases with increasing amount of gold. These results accord to previous studies on AuPt nanoalloys stabilized in SPB where the particle size varies from 4.0 nm with an molar ratio of 73:27 (Au:Pt) to 1.3 nm for a molar Au:Pt ratio of 25:75.[53]For AuPd nanoalloys stabilized on carbon support similar results are observed, *i.e.*, nanoalloys in the size range of 5.3 nm for an 89:11 (Au:Pd) alloy composition and 4.7 nm for an atomistic ratio of 10:90 (Au:Pd), respectively. However, the reason for this particle size variation is still not clear.[151]

Further analyses of AuPd@SPB nanoalloys by powder X-ray diffraction (PXRD) and energy disperse X-ray spectroscopy (EDX) have been performed. The atomistic ratio of gold and palladium has been determined by EDX and shows close values to the theoretical ratios. Detailed information of the bimetallic nanoalloys in Au:Pd ratios of 25:75 ($Au_{25}Pd_{75}$), 50:50 ($Au_{50}Pd_{50}$), and 75:25 ($Au_{75}Pd_{25}$) are summarized in Table 1. The PXRD spectra of the different AuPd@SPB alloy compositions are shown in Figure 13.

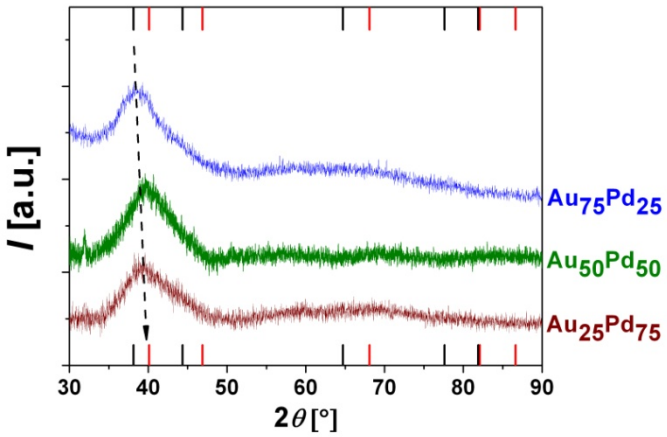

Figure 13: PXRD measurements of different AuPd@SPB compositions. The signal shifts between the values of neat palladium and gold with the atomistic ratio which is marked by the dashed line.[Phys. Chem. Chem. Phys., 2012, 14, 6487-6495.] - Reproduced by permission of the PCCP Owner Societies.

In the PXRD spectra of bimetallic nanoalloys (Figure 13), only one diffraction signal occurs in the range of 38 – 40 ° (2θ) which shifts between the literature values for neat palladium and gold. A linear dependence between the peak positions and the atomistic ratio of gold and palladium is found, which is called Vegard's law. This behavior gives evidence for the presence of bimetallic alloys without phase segregation.

Table 1: First analyses of the AuPd@SPB nanoalloys.[Phys. Chem. Chem. Phys., 2012, 14, 6487-6495.] - Reproduced by permission of the PCCP Owner Societies.

Sample	Molar ratio Au:Pd theoretical	Molar ratio Au:Pd experimental (by EDX)	Metal content [wt %] (by TGA)	Diameter [nm] (by TEM)
$Au_{25}Pd_{75}$	25:75	22:78	4.9	1.7 ± 0.2
$Au_{50}Pd_{50}$	50:50	54:46	5.7	2.2 ± 0.2
$Au_{75}Pd_{25}$	75:25	73:27	7.9	2.5 ± 0.2

The metal loads of the composite particles have been analyzed by thermogravimetric analysis (TGA).

For further evaluation of the structure of bimetallic nanoalloys special emphasis is paid on HR-TEM analysis. To perform HR-TEM measurements on SPB stabilized nanoparticles, the metal crystal has to be placed in a [111] crystal orientation at the

edge of the SPB particle where no additional background is caused by polymers from the SPB stabilizers as shown in Figure 14.

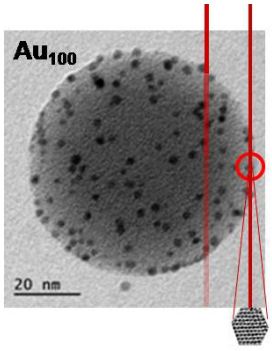

Figure 14: Scheme of the optimal orientation and arrangement of the metal crystal on the SPB carrier system for HR-TEM measurements. The red line represents the electron beam. The left electron beam has to be adjusted at the edge of the SPB (read line on the right hand side) to avoid additional background from the SPB (red line on the left hand side).[Phys. Chem. Chem. Phys., 2012, 14, 6487-6495.] - Reproduced by permission of the PCCP Owner Societies.

Representative HR-TEM images of AuPd@SPB alloys with different compositions and Au@SPB composite particles are shown in Figure 15.

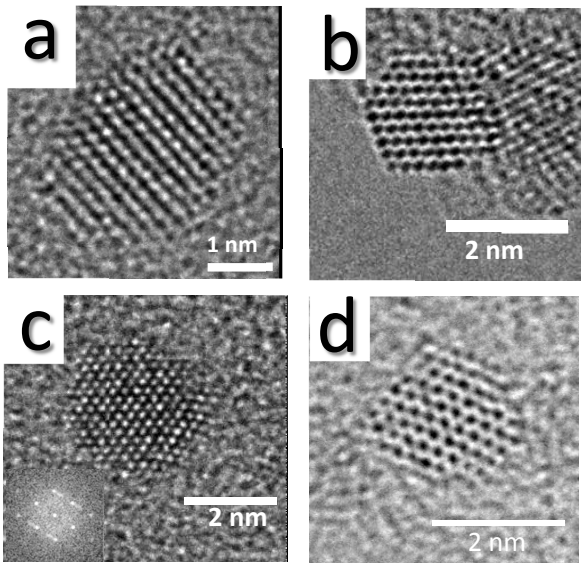

Figure 15: Representative HR-TEM micrographs of SPB stabilized $Au_{25}Pd_{75}$ (a), $Au_{50}Pd_{50}$ (b), $Au_{75}Pd_{25}$(c,) and Au (d) nanoparticles. A FFT image of the HR-TEM of $Au_{75}Pd_{25}$ is shown as an inset (c).[Phys. Chem. Chem. Phys., 2012, 14, 6487-6495.] - Reproduced by permission of the PCCP Owner Societies.

The metal crystals appear as well-defined facetted metalnanoparticles, where atom columns in a [111] crystal orientation can be seen as black dots (see Figure 15). The nanocrystals show a face-centered cubic (fcc) crystal structure and bound mainly by [111] and [001] facets.Thecontrast and the lattice spacing in the nanoparticles are observed consistent all over the whole particle as clearly seen in Figure 15. In the case of a core-shell structure the contrast would clearly differ according to the core-shell structure because of the large difference in the atomic number of the two elements.[152]Thus, no indication of a core-shell structure for the bimetallic nanoalloys of the recent work can be found.

Figure 16shows the lattice spacing of AuPd nanoalloys obtained by FFT analysis from HR-TEM images of the nanocrystals. Within the limits of error, a linear dependence is found between the lattice parameters and the atomistic ratio of Au and Pd which accords with the PXRD measurements.

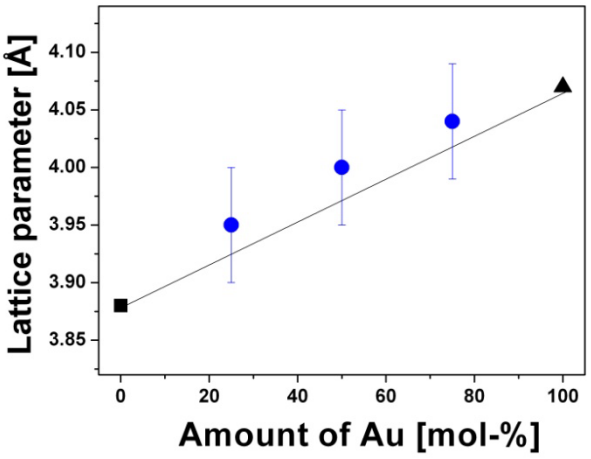

Figure 16: Dependence of the lattice parameters on the atomistic ratio of AuPd@SPB composite particles. The lattice parameters are observed by FFT-analysis of the HR-TEM micrographs.

From all these observations, the structure of randomly mixed nanoalloys for the bimetallic AuPd nanoalloys is assumed. More detailed analysis of the atomistic arrangement of these particles will be given by EXAFS in Chapter4.3.1.

Further analyses have been done by calculations on the electronic density of states (DOS). Recently, Kümmel and Leppert focused on similar calculations for AuPt nanoalloys.[153] In the present work they studied the electronic structure of AuPd nanoalloys. The first step was to test special electronic properties at different Au:Pd

ratios by calculations of the DOS. High DOS close to the Fermi edge would indicate electronically active systems. The results of these calculations are shown in Figure 17 on the left had side for different cluster size with varying Au:Pd ratios.

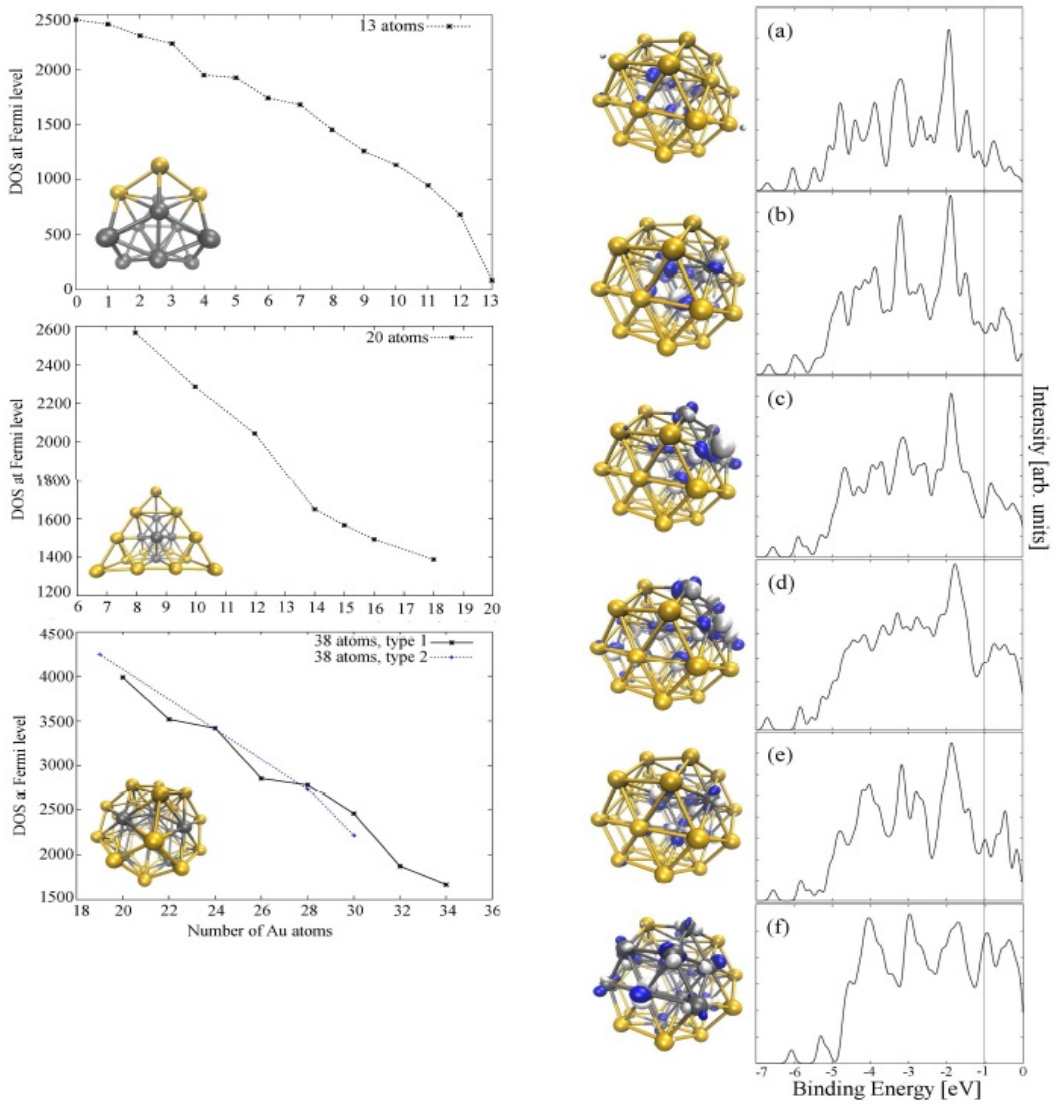

Figure 17: Density of states(DOS) calculations for different AuPd particle sizes and compositions: left hand side: DOS close to the Fermi level in dependence of the amount of gold for 13, 20 and 38 atomic clusters. For the 38 atomic clusters two types are analyzed: a randomly mixed alloy (type 1) and an alloy where Pd is located at the interior part of the facets (type 2). At the right hand side, the DOS for clusters consisting of 38 atoms are analyzed with different atomistic arrangements. Special emphasis is put on the highest occupied molecular orbital (HOMO) illustrated in the cluster schemes. The different clusters are (from top to bottom): (a): $Au_{32}Pd_6$, (b): $Au_{30}Pd_8$, (c)-(e): 3 different structures of $Au_{28}Pd_{10}$ and (f): $Au_{19}Pd_{19}$.[Phys. Chem. Chem. Phys., 2012, 14, 6487-6495.] - Reproduced by permission of the PCCP Owner Societies.

The calculations were started with a cluster size of 13 atoms which is a well-established cluster size for the calculations of Au clusters. Next, the particle size has been increased to 20 atoms to achieve similar atomistic arrangement as for the face-centered-cubic (fcc) formations for gold and palladium. Finally, the cluster size was increased to 38 atoms to form the shape of a truncated octahedron which is shown in Figure 17 (left, from top to bottom) with schematic insets of Au_3Pd_{10}, $Au_{16}Pd_4$ and $Au_{28}Pd_{10}$ clusters, respectively. For the $Au_{28}Pd_{10}$ cluster, two types have been calculated: a randomly mixed cluster (type1) and the energetically preferred cluster type where palladium is located at the interior part of the facets[154] (type 2).Both types show similar results for the DOS.From the calculations of the left hand side of Figure 17, it is clearly seen that the DOS (at the Fermi edge) decrease continuously with increasing amount of gold. Thus,some kind of electronically activation due to a certain Au:Pd ratio, *e.g.*, the 75:25 (Au:Pd) alloy composition which shows the highest catalytic activity, can be ruled out. In the next step, calculations on a cluster consisting of 38 atoms were performed by different arrangements of Au and Pd atoms. The different clusters are illustrated in Figure 17 (a-f) in a schematic fashion and the DOS of the different cluster types are shown beside them. In these calculations special emphasis is put on the highest occupied molecular orbital (HOMO) which represents the energetically high-lying part of the electronic density which is the most reactive one. The results of these calculations are as follows: The HOMO is closely associated with the Pd atoms which will be increased at the surface of the particle with increasing amount of palladium. The HOMO will be dominantly present at the surface of the particle which causes higher activity of the particles. By calculations of different atomistic arrangements of the two elements in the AuPd clusters, it finally turned out that the location of Pd atoms shows high impact on changes in the energetically high-lying part of the density. Thus, these calculations confirm the aspects that alloy systems are more active compared to neat metal nanoparticles and that the atomistic arrangement of elements in the alloy system is supposed to play the key role in the changes of the catalytic activity of AuPd nanoalloys.

4.2 Comparison of Catalytic Activities of Mono- and Bimetallic Nanoparticles

As mentioned in the introductory chapters of this thesis, one main application of metal nanoparticles is their use as catalysts. In this chapter, the catalytic activity of AuPd nanoalloys with different composition and their neat metal nanoparticles will be compared. As a model reaction, the reduction of 4-nitrophenol (Nip) to 4-aminophenol (Amp) by sodium borohydride in presence of metal nanoparticles which is schematically shown in Figure 18, has been chosen.

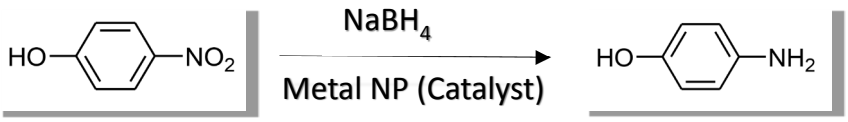

Figure 18: Reaction scheme for the reduction of 4-nitrophenol by sodium borohydride in presence of metal nanoparticles as catalysts.

Nip shows an absorption peak at 400 nm, while theabsorption peak of Amp is at 300 nm. Thus, this catalytic reaction can be monitored by UV-Vis spectroscopy, which is shown in Figure 19a.

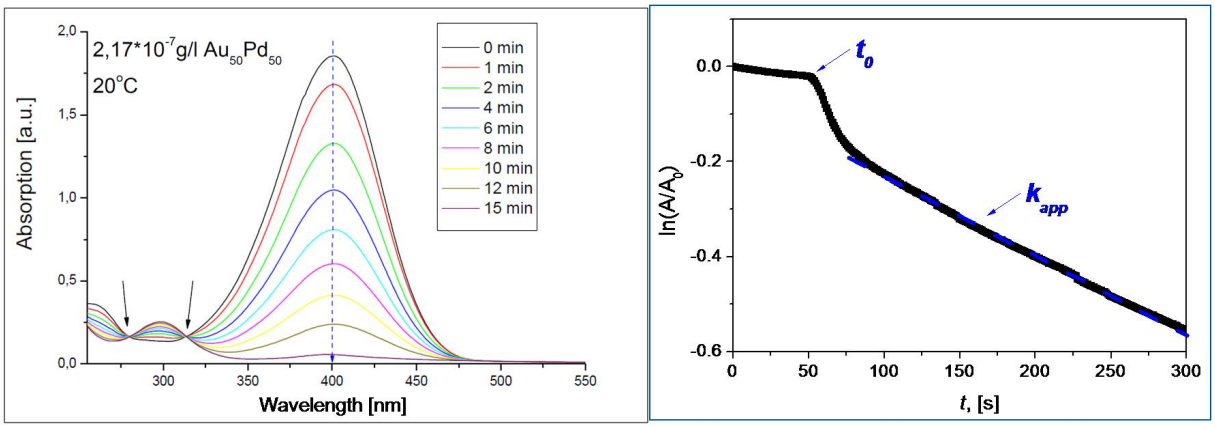

Figure 19: The reduction of Nip by BH_4^- monitored by UV-Vis displayed over a spectrum of 250 – 550 nm (left) and a representative absorption curve of the normalized absorbance vs. time (right).[Phys. Chem. Chem. Phys., 2012, 14, 6487-6495.] - Reproduced by permission of the PCCP Owner Societies.

The UV-Vis spectra in Figure 19 show a decreasing absorption maximum of Nip at 400 nm and simultaneously an increasing adsorption peak at 300 nm by Amp for the reduction of Nip by sodium borohydride. Furthermore, two isosbestic points, marked

with arrows in Figure 19, indicate that no side reaction occurs.

For further kinetic analysis, the absorption at a wavelength of 400 nm is monitored during the reaction. The absorption (A) at a certain reaction time (t) is normalized by the initial absorption (A_0) at $t = 0$. The dependence of $\ln(A/A_0)$ and t is shown in Figure 19. At the beginning, a short time period is visible without any change in the absorption. After this induction time (t_0), the reaction starts. After a certain time, a linear dependence occurs which represents the apparent rate constant (k_{app}) of the reaction.

Thefirst stage of the reaction is analyzed in terms of a pseudo first order reaction due to an excess of sodium borohydride in the reaction mixture. The total surface area of the catalyst in the reaction mixture has been precisely calculated by the particle diameter and the amount of metal particles in the composite particle which were determined by TEM and TGA, respectively.It is found that the apparent rate constant k_{app} is proportional to the total surface area S of the catalyst in the reaction mixture which is shown in Figure 20.

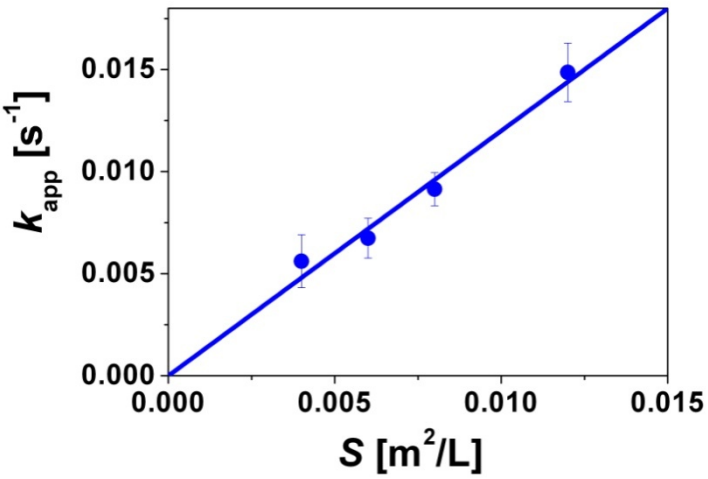

Figure 20: Dependence of the apparent rate constant k_{app} and the total surface area S of the $Au_{75}Pd_{25}$ nanoalloy particles as catalysts at concentrations of c(Nip) = 0.1 mmol/L and c(BH_4^-) = 10 mmol/L.

Thus, the kinetics of this pseudo first order reaction can be described as follows:[48,49]

$$\frac{dc_{Nip}}{dt} = -k_{app}c_{Nip} = -k_1 S c_{Nip} \quad (6)$$

where k_{app} is the apparent rate constant andc_{Nip} is the concentration of 4-nitrophenol.*S*is the surface of the nanoparticle in the reaction mixture normalized by the volume of the reactants and k_1 is the surface reduced rate constant. To compare the catalytic activity of different catalysts the rate constant has to benormalization by the surface of the catalyst. Thus,$k_1$should be employed for this comparison.Figure 21shows the catalytic activity of different AuPd alloy compositions and neat gold and palladium nanoparticles, represented by k_1.

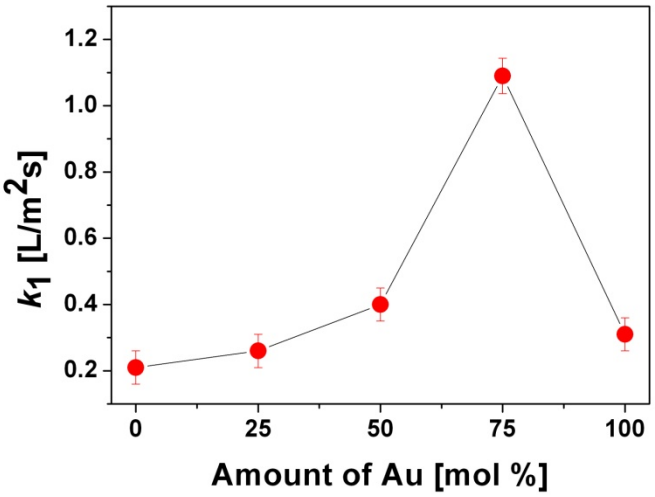

Figure 21: Dependence of the catalytic activity on the molar ratio for AuPd@SPB nanoalloys.[Phys. Chem. Chem. Phys., 2012, 14, 6487-6495.] - Reproduced by permission of the PCCP Owner Societies.

An alloy composition of 75 molar percent of gold and 25 molar percent palladium shows the highest catalytic activity by the screening of different alloy compositions, shown in Figure 21. The catalytic activity of this nanoalloy composition is approximately 5 times higher than those of the neat gold or palladium nanoparticles. This enhanced catalytic performance decreases with increasing amount of palladium. In the case of an alloy composition of 50 molar percent gold the catalytic activity is twice as much compared to palladium nanoparticles but not much higher than that of gold nanoparticles. The catalytic activity of a 25:75 (Au:Pd) composition is in the same range of its neat metal nanoparticles.The kinetics of the $Au_{75}Pd_{25}$@SPB alloy

system which shows the highest catalytic performance will be analyzed in more detail in the next chapter.

4.2.1 Langmuir-Hinshelwood Kinetics

Recently, the reaction mechanism of the reduction of Nip to Amp by sodium borohydride in the presence of SPB stabilized nanoparticles has been investigated by Wunder *et al*.[48,49] in previous work on gold and platinum nanoparticles. The reaction mechanism is shown in Figure 22in a schematic fashion, using the classical Langmuir-Hinshelwood model by following assumptions:The borohydride ions transfer a hydrogen species to the surface of the nanoparticle. Simultaneously, Nip adsorbs on the surface of the catalyst, as well. These two steps are reversible and modeled by a classical Langmuir isotherm. The diffusion of the two substrates to the surface of the catalyst and the adsorption/desorption process is assumed to be fast. Thus, the reaction of Nip to Amp is the rate determining step. Finally, the desorption of the product is assumed to be fast again and thus, can be neglected in the kinetic equation.[1]

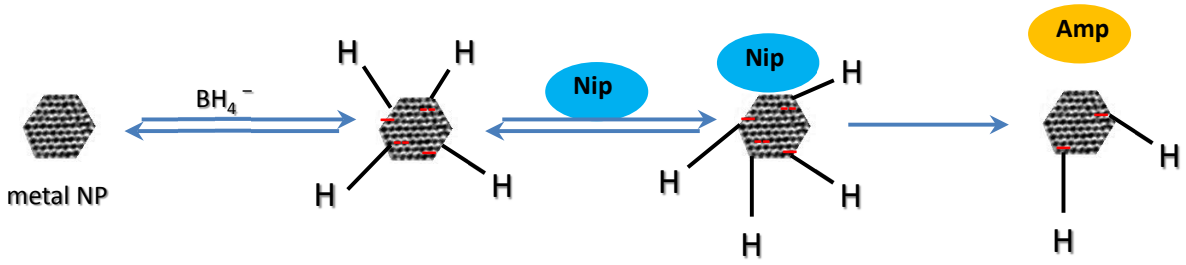

Figure 22: Schematic reaction model for the reduction of Nip by BH_4^- in presence of a metal nanoparticle.[1]

Thus, the apparent rate constant k_{app} of previous described model reaction can be expressed by following kinetic equation:

$$k_{app} = \frac{kSK_{Nip}^{n} c_{Nip}^{n-1} (K_{BH4} c_{BH4})^{m}}{\left(1 + (K_{Nip} c_{Nip})^{n} + (K_{BH4} c_{BH4})^{m}\right)^{2}} \quad (7)$$

where *k* is the molar rate constant, *S* is the surface of the catalyst in the reaction

mixture normalized by the volume of the reaction mixture, K_{Nip} and K_{BH4} are the adsorption constants for Nip and borohydride, respectively.c_{Nip} and c_{BH4} are the concentrations of Nip and BH_4^-, respectively. The exponents *n* and *m* represent the heterogeneity of the sorbents.

To apply previous described model to the reduction of Nip by BH_4^-in the presence of AuPd@SPB nanoalloys two datasets have to be performed: First, the reaction is analyzed at different concentrations of Nip (c_{Nip}) at constant concentrations of borohydride (c_{BH4}). For c_{BH4}, the two concentrations of 10 mmol/L and 5 mmol/L were chosen. c_{Nip} was varied between 0.02 mmol/L and 0.2 mmol/L. The results of this dataset are shown in Figure 23a. Subsequently, c_{BH4} was varied from 2 mmol/L to 20 mmol/L while c_{Nip} was set to 0.05 mmol/L and 0.1 mol/L, respectively. These measurements constitute the second dataset which is monitored in Figure 23c. Figure 23b and 23d display similar measurements on Pd@SPB nanoparticles which were performed to compare AuPd nanoalloys to their neat metal nanoparticles. The results of Au@SPB nanoparticles were taken from previous studies by Wunder *et al.*[48]

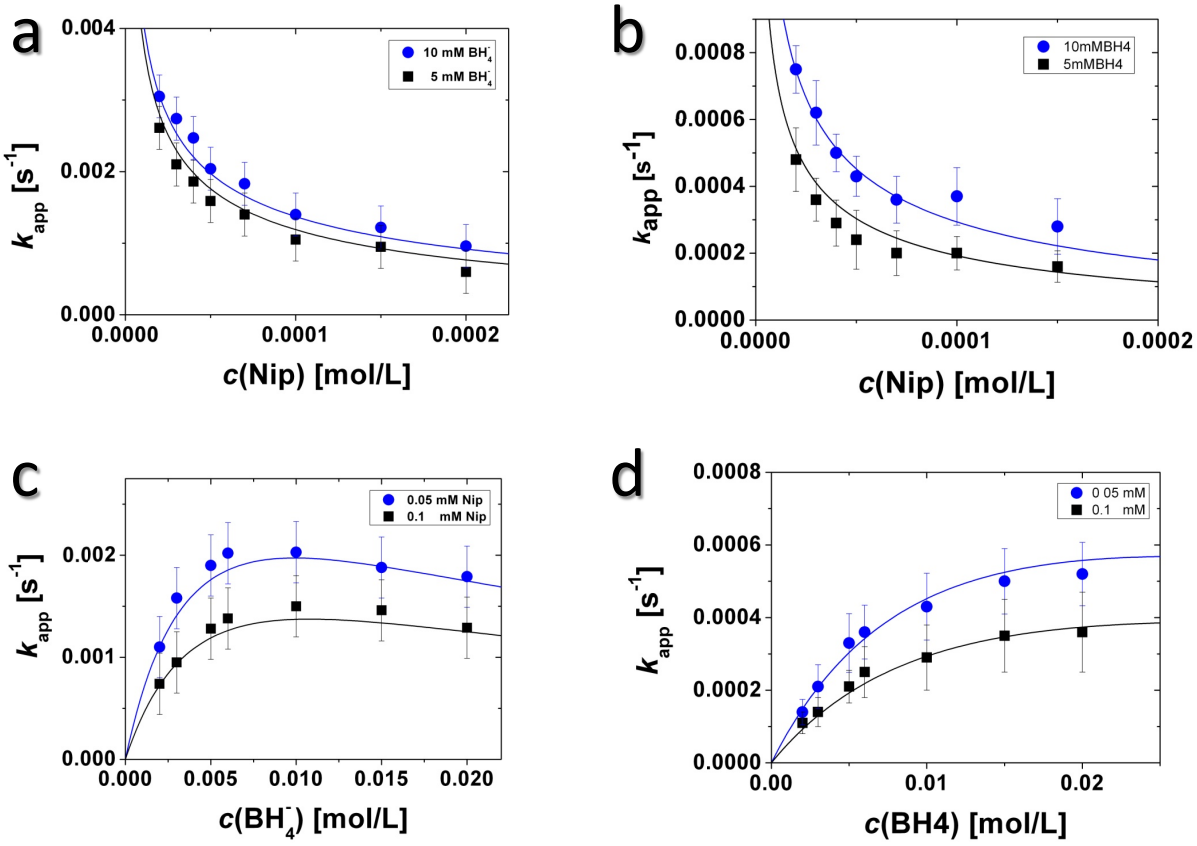

Figure 23: Dependence of the apparent rate constant on the concentration of Nip (a, b) and BH_4^- (c, d) for $Au_{75}Pd_{25}$@SPB (a, c) and Pd@SPB (b, d) composite particles. The experimental data are monitored by blue dots and black squares for different concentrations, respectively. The solid lines display the fits which were achieved by the Langmuir-Hinshelwood model.[Phys. Chem. Chem. Phys., 2012, 14, 6487-6495.] - Reproduced by permission of the PCCP Owner Societies.

The results of these measurements have been fitted by equation(7). The fits are displayed in Figure 23. During the fitting process, a high sensitivity to k, K_{Nip} and K_{BH4} is observed. Thus, precise values have been evaluated with narrow uncertainty. The results of the fits are summarized in Table 2 where AuPd, Au, Pd and Pt nanoparticles stabilized on SPB are compared to each other.

Table 2: Parameters determined by the Langmuir-Hinshelwood model compared for different catalysts. The reaction conditions, e.g., the concentrations of Nip and BH_4^-, were the same for all samples.[Phys. Chem. Chem. Phys., 2012, 14, 6487-6495.] - Reproduced by permission of the PCCP Owner Societies.

metal	k [mol/m^2 s]	K_{Nip} [L/mol]	K_{BH4} [L/mol]	$t_{0,sp}$[s]
$Au_{75}Pd_{25}$	(2.9 ± 0.3) x 10^{-3}	1450 ± 300	122 ± 15	685
Pd	(5.5 ± 0.5) x 10^{-5}	2300 ± 400	48 ± 5	741
Au[48]	(1.6 ± 0.6) x 10^{-4}	5500 ± 1000	58 ± 5	175
Pt[49]	(4.6 ± 0.6) x 10^{-4}	2300 ± 500	98 ± 10	400

From Table 2, it is evident that the $Au_{75}Pd_{25}$@SPB alloy system shows much better catalytic performance than the neat Au@SPB and Pd@SPB nanoparticles. The catalytic activity, represented by k, is nearly 20 times higher than that for Au@SPB nanoparticles. However, the adsorption for Nip is much weaker, compared to the other metal nanoparticles in Table 2, represented by K_{Nip}. On the other hand, there is a stronger adsorption of borohydride on the surface of the bimetallic nanoalloy, which is shown by higher values for K_{BH4}, compared to SPB stabilized Au, Pd and Pt nanoparticles.

The last column in Table 2shows evaluations on the induction periods (t_0) which have been observed for AuPd@SPB and Pd@SPB. These findings accord well to previous studies on Au@SPB and Pt@SPB nanoparticles.[48,49] The induction period is in the range of several seconds to minutes and is shown, *e.g.*, in the representative absorption curve in Figure 19.

This induction period is studied at different concentrations of Nip and BH_4^-. The results of Figure 24b show that t_0 is independent of the concentration of borohydride. Thus, BH_4^-or the hydrogen species from $BH_4^-$is not involved in the process that causes the induction period. In contrast, the concentration of Nip shows high impact on t_0 as it is summarized in Figure 24a. Thus, Nip is supposed to be the key

substrate that causes the process represented by t_0.

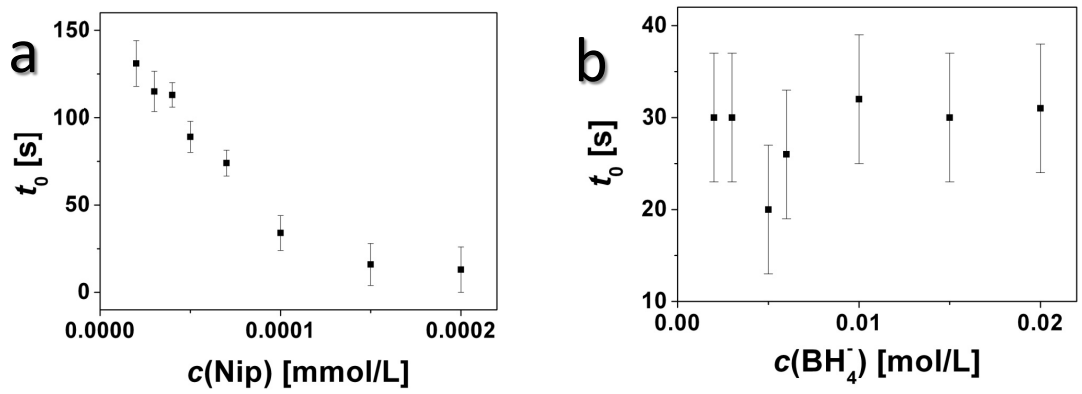

Figure 24: Dependence of t_0 on the concentration of Nip at 10 mmol/L borohydride (a) and ofborohydride at 0.1 mmol/L Nip (b).

In previous studies on Au@SPB nanoparticles similar results have beenobserved for the influence of BH_4^- and Nip concentrations on t_0.[48]Furthermore, the question of a diffusion controlled or a rate controlled reaction has been discussed in previous work.[48] This has been achieved by calculations on the second Damköhler number which is related to the reaction rate, the concentration of the reactant, the mass transport coefficient and the total area of the surface of the catalyst. If the second Damköhler number is below unity the reaction is rate controlled which is the case of SPB stabilized metal nanoparticles.[1,48] In addition, previous studies on Au@SPB nanoparticles revealed evidence for following process: $t_0$denotes the modification of the pristine surface of the catalyst to form active sites for the reduction of Nip.[1,48]Furthermore, $1/t_0$ is found to represent the rate of this surface restructuring process by approximation.[1]

The dependence of inverse t_0 values and the concentration of Nip for AuPd@SPB and further neat metal nanoparticles stabilized in SPB is displayed in Figure 25a. By extrapolation to c(Nip) = 0 mol/L, an intercept occurs which reveals a surface restructuring without any substrate, denoted as spontaneous surface restructuring$t_{0,sp}$. The linear dependence of $1/t_0$ and c(Nip) shows the substrate-induced surface restructuring (see Figure 25a). As displayed in Figure 25b,the substrate-induced surface restructuring scales linearly with θ_{Nip}^2, where θ_{Nip} is the degree of surface coverage by Nip. The square in θ_{Nip}^2 gives evidence that at

least two molecules of Nip need to adsorb at the surface of the catalyst to induce the surface restructuring and thus, activates the catalyst for the reaction.

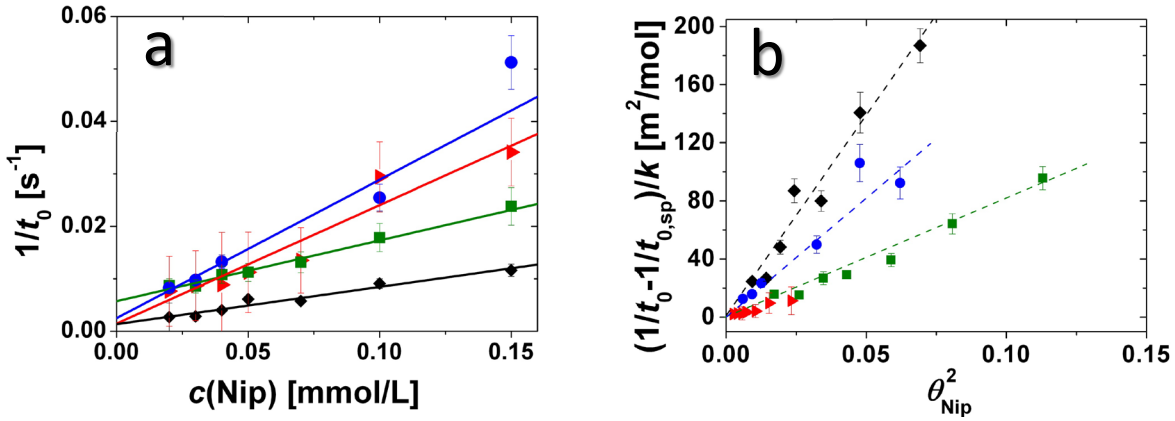

Figure 25: Dependence of the induction period on the concentration of nitrophenol (a) and on the surface coverage of the particle by nitrophenol (b). The different particles are as follows: redtriangles: AuPd; green squares: Au[48]; black diamonds: Pd; blue spheres: Pt[49].[Phys. Chem. Chem. Phys., 2012, 14, 6487-6495.] - Reproduced by permission of the PCCP Owner Societies.

The dependence of the inverse induction period and the degree of surface coverage by Nip is analyzed as follows: The inverse values of spontaneous surface restructuring are subtracted from the inverse values of surface restructuring shown in Figure 25a to obtain the substrate induced surface restructuring ($1/t_0 - 1/t_{0,sp}$). Subsequently, the latter is normalized by the molar rate constant k. The results of this analysis are shown in Figure 25b.They are compared to those of neat gold,[48] palladium and platinum[49]nanoparticles, stabilized in SPB. A linear dependence of $(1/t_0 - 1/t_{0,sp})/k$ are clearly observed for the neat metal nanoparticles as well as the nanoalloys shown in Figure 25b. For the different nanoparticles different slopes are found which indicates the difference in the effectivity of surface restructuring of diverse metals.The reason for this behavior is discussed as follows: The pristine surface of the metal nanoparticles and nanoalloys is inactive for the reduction of 4-nitrophenol by sodium borohydride. Thus, the nanoparticle needs to be activated. This kind of activation of the catalyst is achieved by the substrate Nip, *e.g.*, the substrate induced surface restructuring.

4.2.2 High Resolution – Transmission Electron Microscopy

The structure of metallic nanoparticles is one reason of differences in the catalytic activity as it has been published for AuPd nanoalloys, recently.[27]It is found that the catalytic activity is higher for rougher and more irregular surfaces of catalysts. This enhanced roughness goes hand in hand with higher numbers of corner sitesand thus, higher numbers of low coordinating atoms which are assumed as active sites.[155,156,157]In the present work, similar surface defects and steps are clearly visible for the AuPd@SPB nanoalloys which is presented in HR-TEM images in Figure 26.

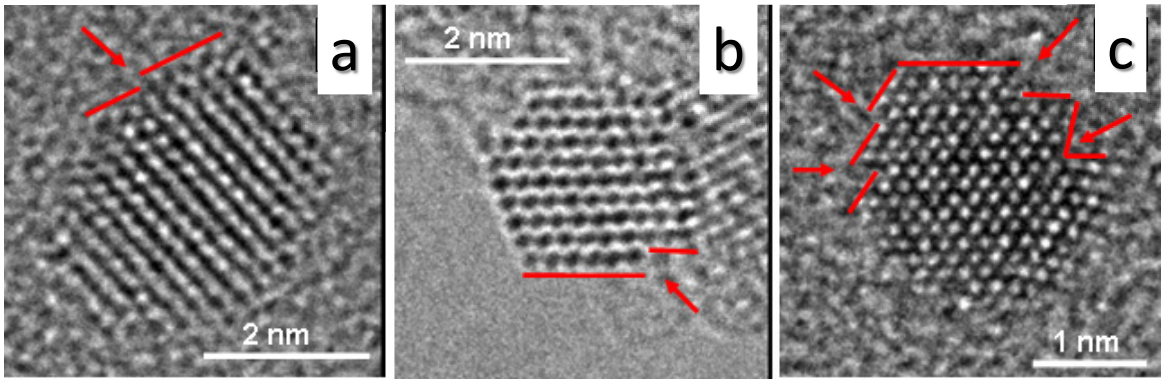

Figure 26: HR-TEM images of $Au_{25}Pd_{75}$@SPB (a), $Au_{50}Pd_{50}$@SPB (b) and $Au_{75}Pd_{25}$@SPB (c) nanoalloys. The red bars mark the steps at the edge of the particles.

These kinds of surface defects are observed in many particles of all AuPd@SPB compositions by HR-TEM micrographs as shown in Figure 27.

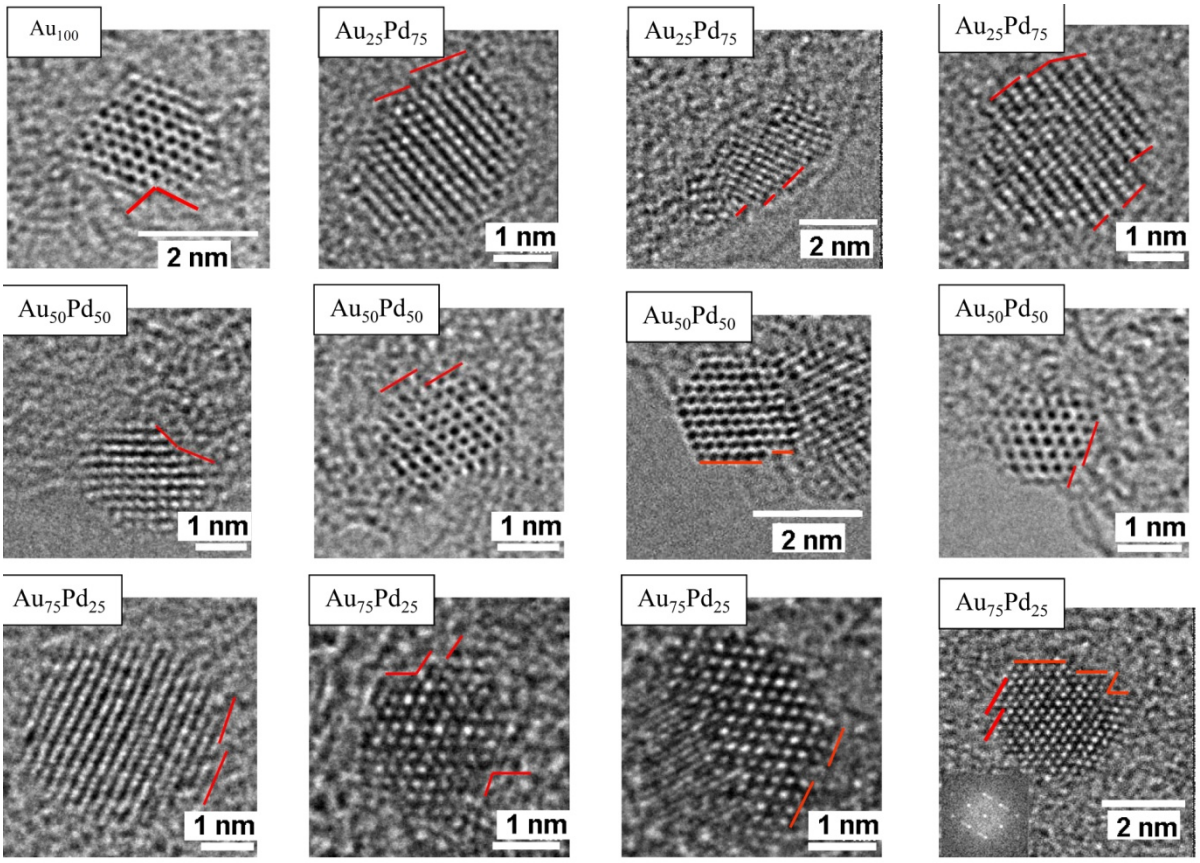

Figure 27: HR-TEM micrographs of AuPd nanoalloys of different compositions. The red bars mark the steps observed on the edge of the metallic nanoparticles.

In order to understand the correlation of the catalytic activity of different AuPd alloy compositions and the surface defects a semi-quantitative evaluation of these surface defects is done as follows: The surface defects appear as steps at the edge of the nanocrystals displayed in typical examples in Figure 27. The frequency of defects in the nanoparticles can be defined as the average number of steps per edge, which is given by the edge length of the crystal divided by the average length of steps. The edge length of the crystal is calculated theoretically from the surface area of a single nanoparticle assuming the shape of a truncated octahedron. The average length of steps is the length of steps divided by the number of steps at the edge, which can be evaluated from the HR-TEM micrographs. To make this calculation more comprehensible an example of that calculation for one micrograph of the $Au_{50}Pd_{50}$@SPB composition is given in Figure 28 and in the following paragraph.

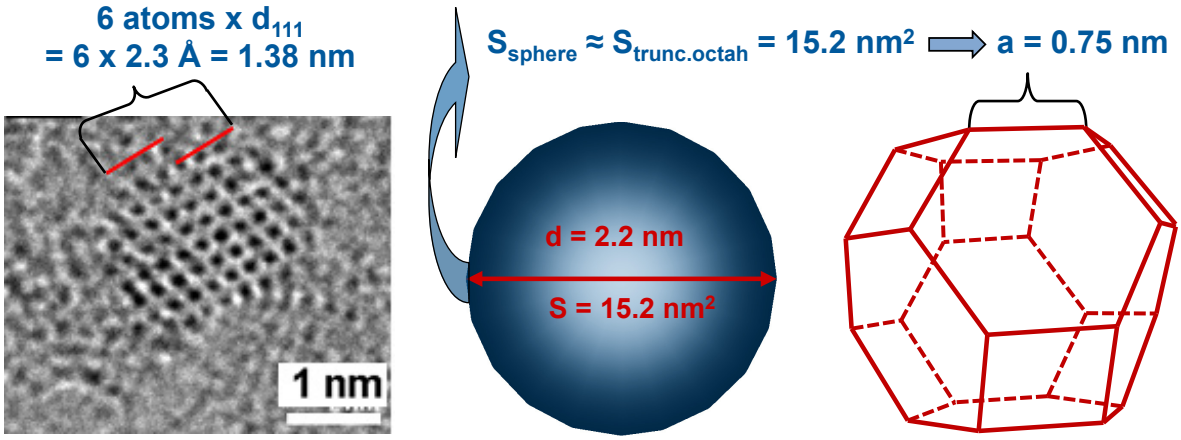

Figure 28: Example for the calculation of surface steps per edge for one micrograph of the $Au_{50}Pd_{50}$@SPB alloy composition.

In Figure 28 the defect is marked by two red lines. The total edge length covered by the red lines contains six atom columns in the pattern appearing as black dots. The total length can be calculated by six multiplied by 2.3 Å, the d_{111} value for the $Au_{50}Pd_{50}$ nanoparticle. Therefore, the length of steps for the $Au_{50}Pd_{50}$ crystal shown in Figure 28 is 1.38 nm.

Assuming the nanocrystal as a truncated octahedron, the length of one edge can be correlated to the surface by following equation:

$$S = (6 + 12\sqrt{3})a^2 \qquad (8)$$

where *S* is the surface area and *a* is the edge length of the truncated octahedron.

The surface area of a truncated octahedral is assumed to be equal to a spherical like particle, by approximation. The mean diameter of the $Au_{50}Pd_{50}$ alloy was evaluated by TEM analysis as 2.2 nm from which the surface area can be calculated as 15.2 nm^2. From equation (8) the edge length of the truncated octahedron can be calculated which is 0.75 nm in this example. Finally, the average number of steps per edge defined as edge length of a truncated octahedron divided by the average length of each step has been calculated as 0.54. An average number of 0.49 has been obtained for the $Au_{50}Pd_{50}$ sample by calculations from several tens of particles from the HR-TEM images.

The length of steps and the number of steps per edge have been calculated for tens of micrographs for every sample. The results of the average values are summarized in Table 3.

Table 3: Catalytic activity in relation to surface defect in AuPd nanoalloys.

Sample	d [a] [nm]	Average length of steps [b] [nm]	k_1 [L m^{-2} s^{-1}]	k_N [c] [L s^{-1} $particle^{-1}$]	Average number of steps per edge [d]
Pd	1.1	-	0.21	$7.98 * 10^{-19}$	-
$Au_{25}Pd_{75}$	1.7	1.17	0.26	$2.36 * 10^{-18}$	0.50
$Au_{50}Pd_{50}$	2.2	1.54	0.40	$6.08 * 10^{-18}$	0.49
$Au_{75}Pd_{25}$	2.5	1.13	1.09	$2.14 * 10^{-17}$	0.75
Au	2.8	1.69	0.31	$7.63 * 10^{-18}$	0.57

a) Diameter of generated metal nanoparticles measured from TEM images.
b) Average length of steps calculated from the HR-TEM images of the particles.
c) k_N: the catalytic rate constant normalized to the number of particles per unit volume.
d) Average number of steps per edge: edge length of a truncated octahedron divided by the average length of each step.

Table 3 compares thecatalytic activity (represented by k_1) as a correlation of the frequency of surface defects of different alloy compositions. The sixth column of Table 3 gathers the probability for a surface defect calculation as the average number of steps in the edge of a truncated octahedron. As shown in Figure 29, there is a distinct maximum for this probability for the $Au_{75}Pd_{25}$@SPB nanoalloy composition which shows the highest catalytic activity as expressed through the normalized rate constant k_N. Hence, this set of data strongly suggests that the catalytic activity of the nanoalloys is related to the number of surface defects.

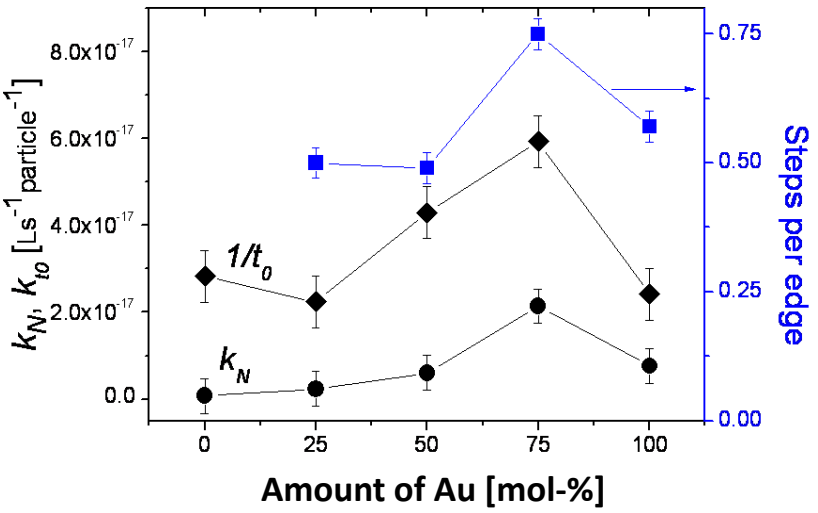

Figure 29: Catalytic efficiency as a function of the amount of gold in the nanoalloys. Circles: rate constants of AuPd@SPB composite particles normalized to the number of particles per unit volume (k_N), diamonds: induction time treated as a rate constant ($1/t_0$), which is normalized to the number of particles per unit volume, squares: average number of steps per edge.

Further evidence can be found from the analysis of the induction period t_0 that can be observed for the catalytic reduction of 4-nitrophenol as discussed in chapter 3.2.1. In this previous chapter it is shown that t_0 is related to a surface restructuring of the metal surface necessary to render the metal nanoparticles an active catalyst. Figure 29 displays $1/t_0$ against the mol fraction of Au in the nanoalloys. The reciprocal of the induction time is treated as a rate constant which is normalized to the number of particles per unit volume. A distinct maximum has been observed for the $Au_{75}Pd_{25}$ sample, which contains highest frequency of surface defects. This indicates that the surface defects in the sample are favor for the restructuring of the metal surface.

4.2.3 Adsorption Behavior of Support-Free Gold Nanoparticles

Support-free gold nanoparticles were produced in a one-step fabrication by laser ablation. The proceeding of this approach has been explained in detail in chapter 3.1.2. This approach has been developed by Barcikowski[37,38,158] and co-workers recently for the fabrication of nanoparticles of several metals.[37,38,93] These metal nanoparticles do not contain additives, *e.g.*, polymer

stabilizers.[38,94]Thus, the impact of the SPB carrier system on the catalytic behavior of metal nanoparticles can be analyzed by comparison of SPB stabilized metal nanoparticles and the support-free nanoparticles. A representative TEM image and the size distributionof gold nanoparticles, produced by laser ablation, are displayed in Figure 30.

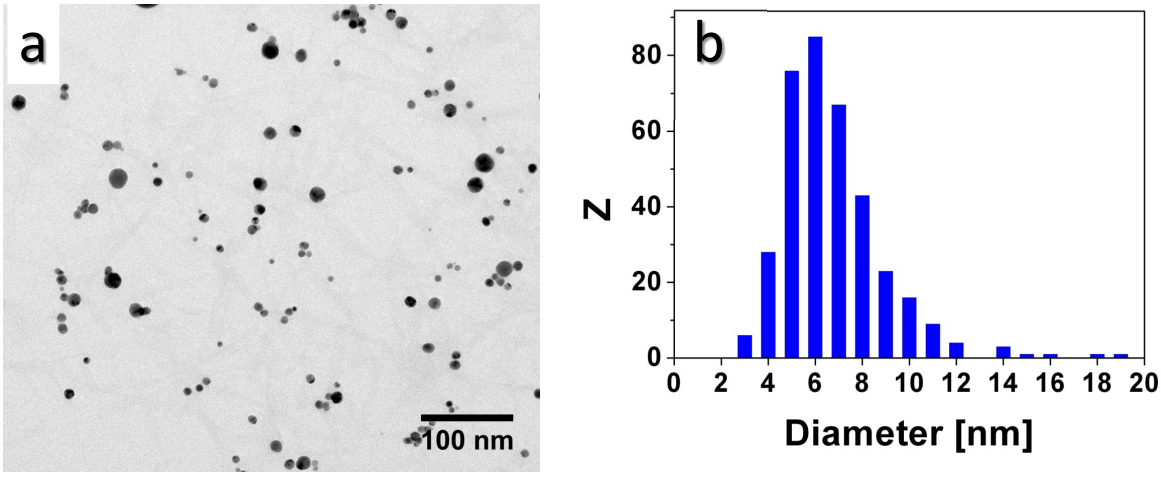

Figure 30: Representative TEM micrograph of support-free gold nanoparticles generated by laser ablation (a) and the particle size distribution of these gold nanoparticles (b).

The average size of these gold nanoparticles has been evaluated as 7.2 ± 2.1 nm from Figure 30b. The catalytic behavior of these particles has been studied by the reduction of 4-nitrophenol as well. Up to now no publication has been found where this model reaction has been applied to support-free metal nanoparticles. The UV-Vis absorption analysis of the model reaction applied to support-free gold nanoparticles accords well to previous studies on SPB supported metal nanoparticles: In the UV-Vis adsorption spectra (Figure 31a) a linear section of $\ln(A/A_0)$ vs. reaction time (marked by k_{app}) as well as an induction period (marked as t_0) has been observed. Furthermore, the apparent rate constant k_{app} scales linear to the total surface area of the catalyst which is displayed in Figure 31b.

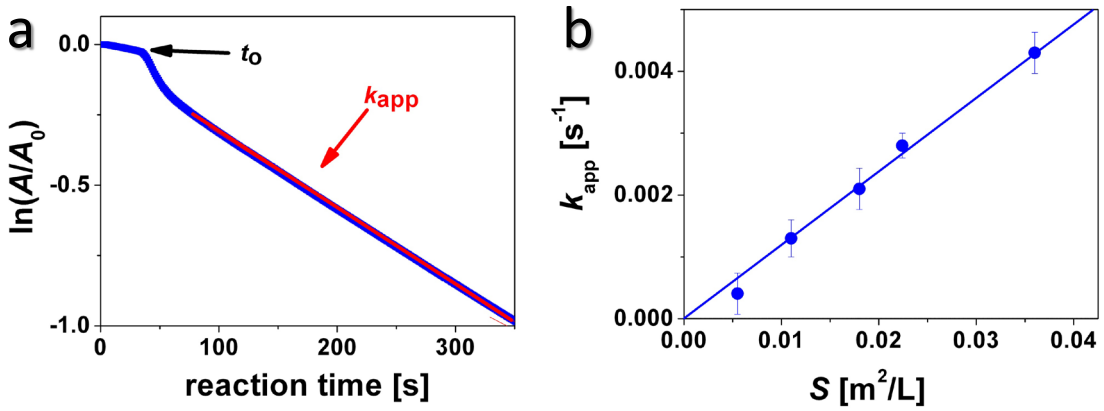

Figure 31: Representative normalized UV-Vis absorption spectrum of the reduction of Nip by BH_4^- in presence of support-free gold nanoparticles (a) and the dependence of the apparent rate constant on the surface area of the catalyst (b).

The surface reduced rate constant k_1 for the model reaction applied on support-free gold nanoparticles results from the slope of the curve in Figure 31b as 0.13 L/m^{2}s. The k_1 values for the reduction of Nip in presence of gold nanoparticles from literature which arestabilized by different support are compared to each other together with support-free gold nanoparticles in Table 4.

Table 4: Comparison of k_1 values of gold nanoparticle for the reduction of Nip by BH_4^- in the present work to results taken or recalculated from literature.

Support	**k_1 [L/m^{2}s]**	**Diameter [nm]**	**Reference**
Acetanilide	0.65	5.0	[159]
Polyelectrolyte brush	0.51	1.3	[47]
Poly(methyl methacrylate)	0.50	6.9	[160]
Polyelectrolyte brush	0.27	2.2	[48]
Polymer core-shell microgel	0.14	6.6 x 35 (rods)	[161]
support-free	**0.13**	**7.2**	**Present study**
β-D-Glucosidase	0.04	8.2	[162]
Polymer micelles	3.7×10^{-3}	3.3	[163]
Polymer brush	5.0×10^{-4}	4.2	[164]
Polyaniline nanofibers	1.9×10^{-5}	2.0	[165]
Citrate	5.2×10^{-6}	20	[166]

In Table 4gold catalysts stabilized by different support materials observed in literature and support-free gold nanoparticles are listed in the sequence highest catalytic activity to lowest. It is obvious that the support-free gold nanoparticles are active catalysts for the reduction of Nip. The catalytic activity of support-free gold catalysts is indexed somewhere in the middle compared to literature values. To gain deeper insight into the catalytic behavior of support-free gold nanoparticles, kinetic study has been done by applying the Langmuir-Hinshelwood model. The analysis has been performed under analogous conditions applied for AuPd@SPB nanoalloys and Pd@SPB nanoparticles in chapter 4.2.1. Figure 32 displays the two datasets obtained in the case of the support-free gold nanoparticles.

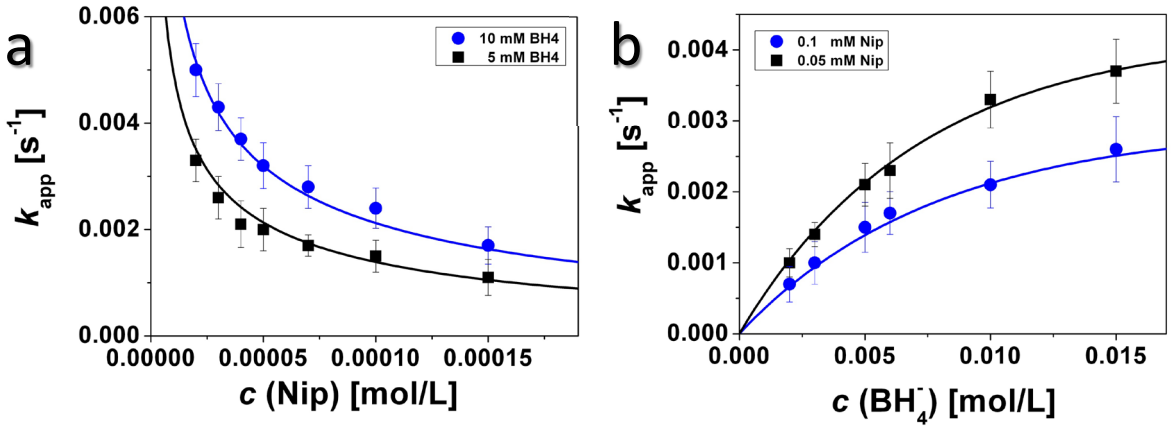

Figure 32: Dependence of the apparent rate constant on the concentration of Nip (a) and BH_4^- (b) for support-free gold nanoparticles.

The catalytic behavior of support-free gold nanoparticles accords to previous studies on SPB stabilized metal nanoparticles and nanoalloys. Thus, the Langmuir-Hinshelwood model has been applied for data fitting of the results in Figure 32. The parameters determined by Langmuir-Hinshelwood kinetics are presented in Table 5and compared to those obtained for SPB stabilized nanoparticles.

Table 5: Parameters determined by Langmuir-Hinshelwood kinetics and compared to previous studies. For each system in the table, exactly the same concentrations of Nip and BH_4^- have been used.

	metal	k [mol/m^2 s]	K_{Nip} [L/mol]	K_{BH4} [L/mol]	m	n	$t_{0,sp}$ [s]
	support-free Au	(2.0 ± 0.6) x 10^{-4}	1600 ± 400	45 ± 10	1	0.6	158
Ref[48]	Au@SPB	(1.6 ± 0.6) x 10^{-4}	5500 ± 1000	58 ± 5	1	0.6	175
Ref[49]	Pt@SPB	(4.6 ± 0.6) x 10^{-4}	2300 ± 500	98 ± 10	1	0.6	400
Chapter 4.2.1	Pd@SPB	(5.5 ± 0.5) x 10^{-5}	2300 ± 400	48 ± 5	1	0.6	741
Chapter 4.2.1	$Au_{75}Pd_{25}$@SPB	(2.9 ± 0.3) x 10^{-3}	1450 ± 300	122 ± 15	1	0.6	685

The molar rate constant of the support-free gold nanoparticles is (2.0 ± 0.6) x 10^{-4}mol/m^{2}s which is almost the same as that for Au@SPB nanoparticles. However, the adsorption constant of 4-nitrophenol ($K_{Nip)}$ is 1600 ± 400 L/mol which differs a lot from the one obtained for SPB supported gold nanoparticles as summarized in Table 5. This value is close to that for AuPd@SPB nanoalloys. K_{Nip} represents the adsorption strength of Nip to the surface of the catalyst. Thus, the adsorption of Nip to SPB stabilized gold nanoparticles is much stronger than that for unsupported gold nanoparticles. A supposed reason for thisis the electrostatic repulsion of the negatively charged surface of unsupported nanoparticles and the negatively charged Nip.

The adsorption constant of BH_4^-(K_{BH4}) for support-free gold nanoparticles is smaller than thoseofthe SPB stabilized nanoparticles discussed in this work (see Table 5). Comparing the unsupported gold nanoparticles to SPB supported gold and palladium nanoparticles similarK_{BH4} values are found. The K_{BH4} values of Pt@SPB and AuPd@SPB particles are almost twice as much as for unsupported gold nanoparticles. These values indicate lower adsorption strength for gold and palladium than for platinum and the alloy system studied in this work. For the discussion of K_{BH4} it needs to be noted that this step implicates the transfer of a hydrogen species from BH_4^- to the surface of the catalyst.This describes a multi-step process which is difficult to interpret.

The induction period (t_0) has been observed for support-free gold nanoparticles as well as shown in the representative spectrum in Figure 33b. The results for t_0 accord to those of previous studies, *e.g.*, $t_0$depends on the concentration of Nip but not on the concentration of BH_4^-. The induction period expresses the surface restructuring of the surface of the catalyst whichis supposed to activate the catalyst for the reaction.The inverse induction time period which represents the rate of this surface restructuring is displayed for different concentrations of Nip in Figure 33a for SPB supported and unsupported gold nanoparticles.

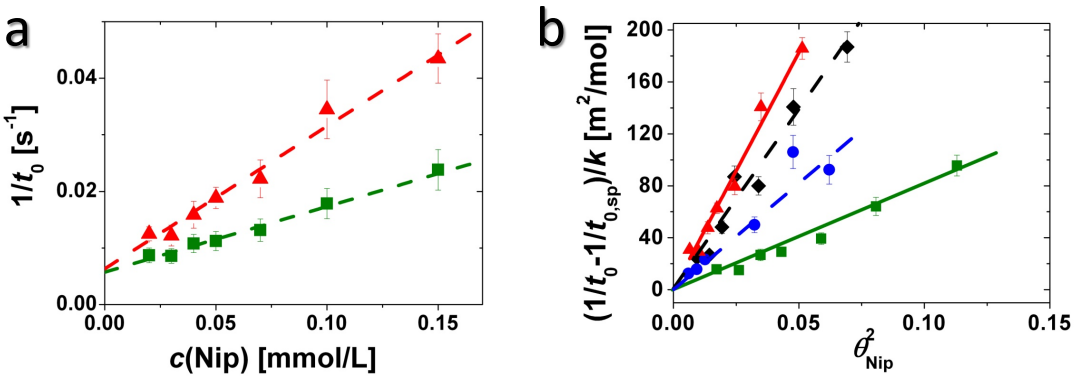

Figure 33: Dependence of the induction period on the concentration of Nip (a) and on the surface coverage by Nip (b). The symbols are as follows: red triangles: support-free gold nanoparticles, green squares: Au@SPB,[48]blue spheres: Pt@SPB,[49]black diamonds: Pd@SPB;

It can be clearly seen that the intercept for *c*(Nip) = 0 mmol/L in Figure 33a which denotes the value of the spontaneous surface restructuring ($1/t_{0,sp}$) is similar for supported as well as for support-free gold nanoparticles. In contrast the slope of the $1/t_0$ vs. *c*(Nip) curve is much higher for support-free nanoparticles than for nanoparticles stabilized by polymeric support. This slope depicts the substrate induced surface restructuring which is easier achieved for unsupported gold nanoparticles than for the SPB stabilized one. Finally, to compare these two systems with the previous SPB stabilized palladium and platinum nanoparticles, the inverse values for the spontaneous surface restructuring are subtracted from $1/t_0$ values and normalized by the molar rate constant *k* to obtain the rate of the substrate induced surface restructuring. The dependence of the latter on the square of the surface coverage by Nip (θ_{Nip}^2) is displayed in Figure 33b. A linear dependence of ((1/t0)-(1/t0,sp))/k and θ_{Nip}^2 is found in case of the support-free nanoparticles (as well

as for SPB stabilized nanoparticles) which indicates that at least two Nip molecules have to adsorb on the surface of the catalyst to induce the surface restructuring. The plot of Figure 33b demonstrates that the substrate induced surface restructuring proceeds fast in the case of support-free nanoparticles compared to gold, palladium and platinum stabilized by SPB. These findings finally lead to the result that the polymer system does not have influence on the molar rate constant for the reduction of Nip.However, it influences the substrate induced surface restructuring which needs to proceed previously to activate the catalyst for the reaction.

4.3 Extended X-Ray Absorption Fine Structure Analysis

As mentioned previously in chapter 3.5, EXAFS is one of the most important analyzing methods in this work. The evaluation of the atomistic arrangement of gold and palladium in the alloy systems and the lattice parameters of gold nanoparticles with different sizes has been analyzed by EXAFS measurements.

4.3.1 Structure of Bimetallic Gold-Palladium Nanoalloys

The determination of coordination numbers for each element is the key to evaluate the atomistic arrangement of bimetallic nanoalloys by EXAFS measurements.In addition, EXAFS offers access to electronic states, *e.g.*, the oxidation number, of each element. In the literature, only few publications show measurements on particles larger than 10 nm.[7,139] Most of them analyze small nanoalloys (1 – 7 nm size) by EXAFS measurements.[8,28,72,130,131,132,133,134,135,136,137,167]Sometimes measurements on bimetallic alloys have beenonly performed at the AuL_3 edge.[28,137,167]However, by measurements at both edges, total structural analysis is most likely achieved, as it is applied by most research groups.[8,72,130,131,132,133,134,135,136,139] By analysis at both absorption edges a Pd-O peak appears in addition to Pd-Pd and Pd-Au signals at the Pd K adsorption edge.[129]Measurements at the Au L_3 edge of the AuPdnanoalloys show signals which are generated by metallic Au-Au and Au-Pd bonds only.[129]

Furthermore EXAFS studies showing signals of partially oxidized palladium at the Pd K absorption edge of AuPd nanoalloys has been reported by Krumeich *et al.*[136] for particles supported by TiO_2. However, this Pd-O signal disappears for Al_2O_3 supported nanoalloys. This group also found aninhomogeneity in the arrangement of Au and Pd atoms that deviate from randomly mixed alloy structure. It turned out that Pd is slightly enriched at the particles surface while Au atoms are more enhanced at the core of the particle. However, only slight enrichments of each element areobserved. Core-shell structure can be ruled out.[136] Analogous results for slight element enrichments and Pd-O signals at the Pd K edge for different AuPd nanoalloy systems are reported in literature.[28,72,130,132,133,134,135,136]

In the present work, special emphasis is put on the evaluation of coordination numbers (CN) for gold and palladium. The CN of one absorption edge, *e.g.*, the Au L_3 edge, can be split into the CN of gold to palladium, *i.e.*, the number of Au-Pd bonds at the gold edge ($N_{Au\text{-}Pd}$)and the CN of gold to vicinal gold atoms, *i.e.*, the number of Au-Au bonds at the gold edge ($N_{Au\text{-}Au}$).Similarly,the nomenclature at the Pd K edge is as follows:$N_{Pd\text{-}Pd}$ for the number of Pd-Pd bonds and $N_{Pd\text{-}Au}$ for the number of Pd-Au bonds. At this point it should be mentioned once more that all values, *e.g.*, number of bonds, distances and CN are average values due to the collection of signals from thousands of particles during one EXAFS measurement.

In the present work the AuPd@SPB nanoalloys which have been studied in terms of their catalytic behavior previously were analyzed by EXAFS. The experimental chi(*k*) plots of AuPd nanoalloys are displayed in Figure 34 for the Au L_3absorption edge (a) and thePd K absorption edge (b).

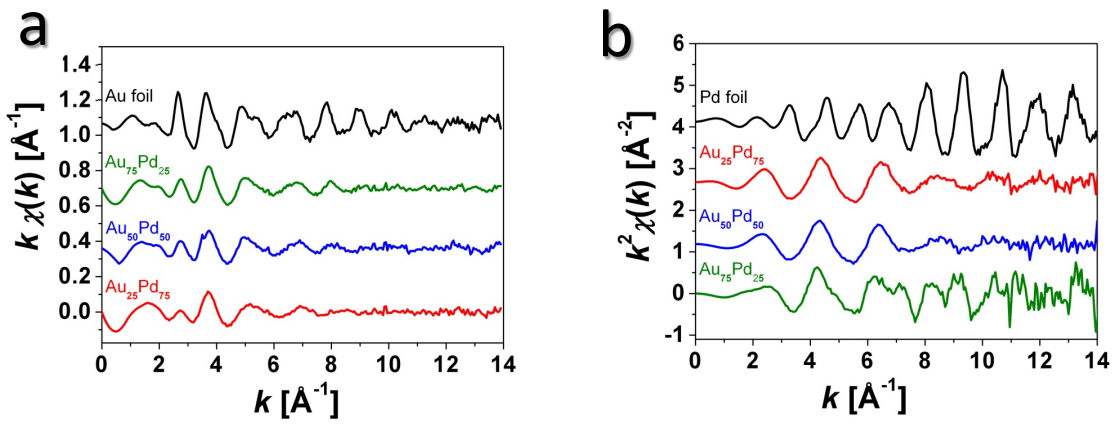

Figure 34: Chi(k) vs. k plots from the EXAFS measurements for different AuPd@SPB alloy compositions at the AuL_3 absorption edge (a) and at the Pd K absorption edge (b).[Faraday Discuss., 2013, Accepted Manuscript, DOI: 10.1039/C3FD20132E] - Reproduced by permission of The Royal Society of Chemistry.

From Figure 34 only slight differences in the different absorption spectra can be seen. Thus, the spectra have to be Fourier transformed (FT). First, the Au L_3 absorption edge will be discussed. The FT spectra are displayed in Figure 35 for the imaginary part (a) and the magnitude (b) of AuPd@SPB alloy compositions at the Au L_3 absorption edge. The amplitude for nanoalloys is smaller compared to that of the reference foil due to less CN for nanoparticles. In addition, a decrease of the amplitude is observed at the Au L_3 absorption edge with decreasing amount of gold and at the Pd K absorption edge with decreasing amount of palladium because of less CN for gold or palladium at the correspondent absorption edge.

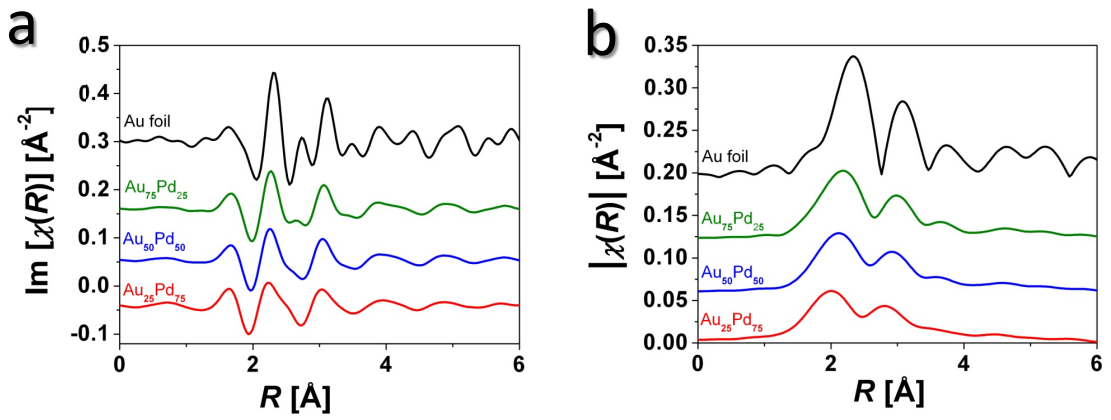

Figure 35: FT – chi(R) spectra of different AuPd@SPB alloy compositions at the Au L_3 absorption edge. The imaginary part (a) of the Fourier transformation and the magnitude (b) are displayed.[Faraday Discuss., 2013, Accepted Manuscript, DOI: 10.1039/C3FD20132E] - Reproduced by permission of The Royal Society of Chemistry.

A shift to smaller *R*-values and thus, to smaller atomic distances is clearly seen for increasing amount of palladiumin Figure 35. This reflects the Vegard's law, *i.e.*, the lattice parameters scale linear between those values for neat palladium and gold by the ratio of the AuPd alloy composition. At this point it should be mentioned that the *R*-values in the FT-spectra indicate the distances of nearest neighbor atoms but do not directly give the lattice parameter. All peaks are shifted to smaller distances due to the approximation that a finite oscillation in the EXAFS spectra is treated as an infinite oscillation by the Fourier transformation. Thus, the FT-spectra need to be fitted to determine parameters, *e.g.*, atomic distances and coordination numbers. In the present work the FEFF code[29] has been established to model the experimental data. The applied models are explained in the Experimental and Data Processing part of this thesis in chapter 6. The results of the fits are shown in Figure 36together with the experimental data.

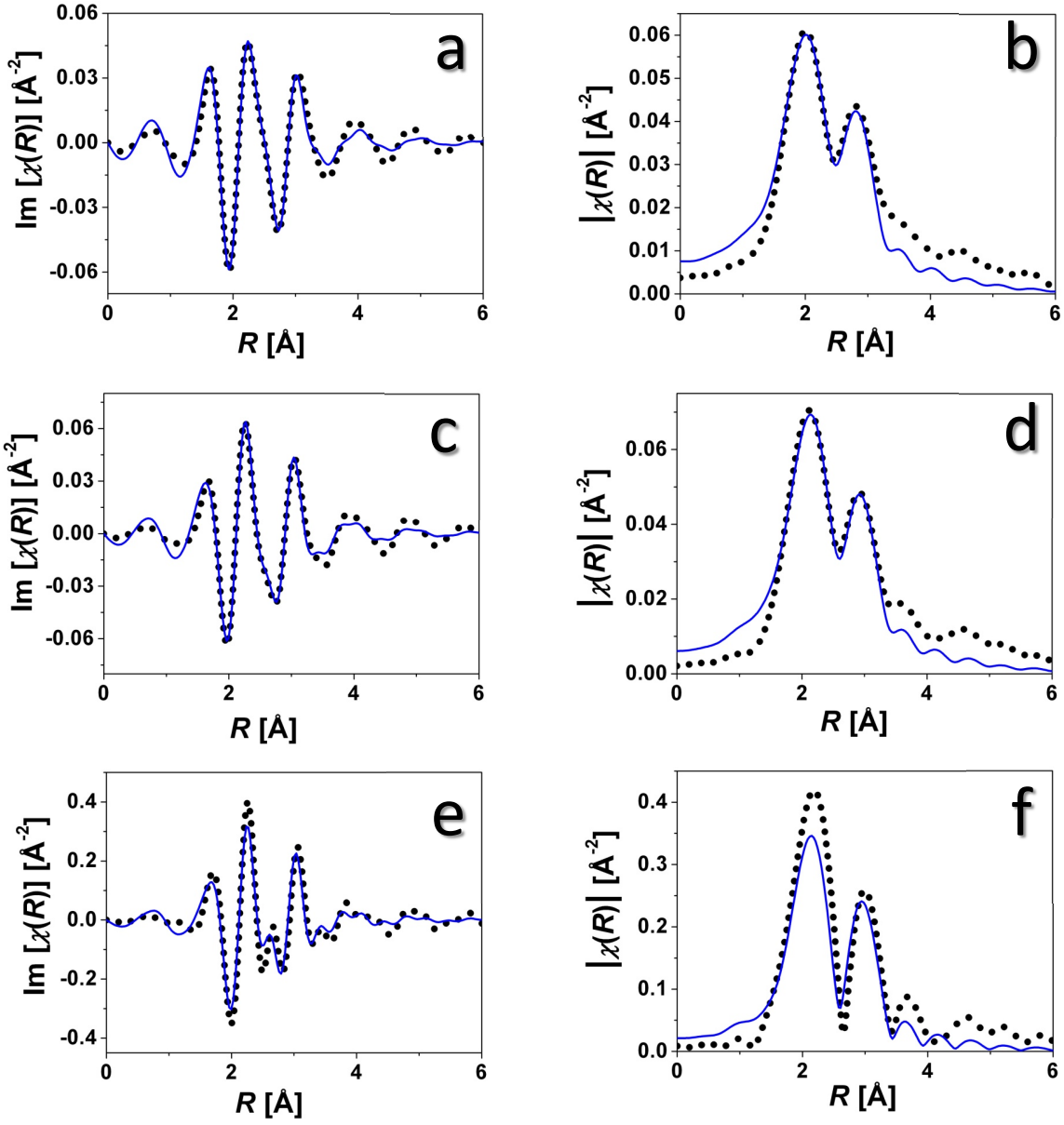

Figure 36: Fits and experimental data of the first coordination shell of $Au_{25}Pd_{75}$ (a, b), $Au_{50}Pd_{50}$ (c, d) and $Au_{75}Pd_{25}$ (e, f) nanoalloys displayed by the imaginary part (a, c, e) and the magnitude (b, d, f) of the FT spectra at the Au L_3 absorption edge. The fits are shown by blue lines and the experimental data by black dots, respectively.[Faraday Discuss., 2013, Accepted Manuscript, DOI: 10.1039/C3FD20132E] - Reproduced by permission of The Royal Society of Chemistry.

The fit results are summarized in Table 6 for measurements at the Au L_3 absorption edge.

Table 6:Results of the EXAFS fitting parameters. N = Coordination number, N_{total} = sum of N at one absorption edge, R = interatomic distance, σ^2 = Debye-Waller Factor, ΔE_0 = inner core correction.[Faraday Discuss., 2013, Accepted Manuscript, DOI: 10.1039/C3FD20132E] - Reproduced by permission of The Royal Society of Chemistry.

Sample	Edge	Pair	*N*	N_{total}	*R* [Å]	σ^2 [Å^{-2}]	ΔE_0 [eV]
Au-NP	AuL_3	Au-Au	7.5 ± 0.3	7.5 ± 0.5	2.821 ± 0.004	0.0122 ± 0.0005	1.6 ± 0.3
$Au_{75}Pd_{25}$	AuL_3	Au-Au	4.6 ± 0.3	5.7 ± 0.5	2.786 ± 0.005	0.0075 ± 0.0008	1.7 ± 0.5
	AuL_3	Au-Pd	1.1 ± 0.2		2.716 ± 0.005	0.0075 ± 0.0008	1.7 ± 0.5
$Au_{50}Pd_{50}$	AuL_3	Au-Au	3.9 ± 0.3	5.2 ± 0.5	2.766 ± 0.005	0.0075 ± 0.0010	0.6 ± 0.4
	AuL_3	Au-Pd	1.3 ± 0.2		2.696 ± 0.005	0.0075 ± 0.0010	0.6 ± 0.4
$Au_{25}Pd_{75}$	AuL_3	Au-Au	3.3 ± 0.2	4.6 ± 0.3	2.698 ± 0.005	0.0075 ± 0.0009	-3.4± 0.4
	AuL_3	Au-Pd	1.3 ± 0.1		2.628 ± 0.005	0.0075 ± 0.0009	-3.4± 0.4

To analyze the atomistic arrangement in bimetallic nanoalloys, special emphasis is put on the CN, *i.e.*, the number of bonds *N* in Table 6. For homogeneous AuPd nanoalloys, the ratio between $N_{Au\text{-}Au}$ and $N_{Au\text{-}Pd}$ must be equal to the atomistic ratio of Au:Pd. The results for *N* in Table 6 show that this condition is not fulfilled for the AuPd@SPB composite systems. Therefore strict statistically mixing of the two elements is excluded. Next, the possibility of a core-shell structure will be checked. In the case of a Au_{core}-Pd_{shell} structure the N_{total} values at the Au L_3 absorption edge have to show values close to 12, *e.g.*, 8 – 12. This condition is not fulfilled by the results of Table 6. Thus, the Au_{core}-Pd_{shell} structure can be excluded as well. In addition, the possibility of a core-shell structure where palladium is in the core and gold constitutes the particle shell would show small values for N_{total} at the Au L_3 absorption edge which is not given by the results in Table 6. Thus, the Pd_{core}-Au_{shell} structure is ruled out as well. The N_{total} values of the AuPd nanoalloys are between 4.6 and 5.7 which are lower than the value for the gold nanoparticle (7.5) which is interpreted by the particle size that decreases with the amount of palladium causing

higher numbers of surface atoms and less amount of gold which causes lower CN at the Au L_3 absorption edge.

In the case of homogeneously mixed alloys, *e.g.*, the $N_{Au\text{-}Au}$ value for an alloy composition of $Au_{50}Pd_{50}$ would be 2.6. In the present work it is 3.9 which gives evidence for a higher number of Au-Au bonds compared to a homogenous alloy structure. Thus, a slight enrichment of gold atoms in the center of the particle is supposed. The results for the $Au_{25}Pd_{75}$ alloy composition are similar. The evaluated$N_{Au\text{-}Au}$ is 3.3 instead of 1.2 which would result by a homogenous alloy structure. Thus, the evaluation gives evidence for an enrichment of gold atoms in the core of the particle as well. Comparing the $N_{Au\text{-}Au}$ values of a $Au_{50}Pd_{50}$ with a $Au_{25}Pd_{75}$ alloy composition the effect of a gold enriched core appears stronger in the $Au_{25}Pd_{75}$ alloy compared to the $Au_{50}Pd_{50}$ alloy. Finally, the $Au_{75}Pd_{25}$ alloy composition shows values of 4.6 for $N_{Au\text{-}Au}$ and 1.1 for $N_{Au\text{-}Pd}$ which is close to the theoretical values for a homogenous alloy of 4.3 ($N_{Au\text{-}Au}$) and 1.4($N_{Au\text{-}Pd}$).

The results for analyses of CNs at the Au L_3 absorption edge for the different alloy compositions are summed up as follows: A core-shell structure can definitely be ruled out for all nanoalloys in the present study. However, the $Au_{50}Pd_{50}$ and the $Au_{25}Pd_{75}$nanoalloys show slight enrichment of gold atoms in the core of the particles and of palladium at the surface. This effect is more obvious for the $Au_{25}Pd_{75}$ alloy compared to the $Au_{50}Pd_{50}$ alloy. The analysis for the $Au_{75}Pd_{25}$ alloy composition results in a structure that is close to a homogeneously mixed alloy.

As it can be clearly seen in Table 6, the interatomic distance (R) decreases with increasing amount of palladium due to smaller lattice parameters of palladium compared to gold and the decreasing lattice parameters with decreasing particle size. The latter effect is observed for various metal nanoparticles. This effect will be discussed for gold nanoparticles with different sizes in the following chapter 4.3.2. In addition, the values for σ^2 and ΔE_0 are in good agreement, keeping in mind that bulk models are applied to nanoparticles.

The measurements of AuPd@SPB nanoalloys at the Pd K absorption edge result in spectra that show more complicated features compared to those at the Au L_3 absorption edge. The FT spectra are shown in Figure 37. Comparing the AuPd@SPB

alloy systems to the palladium reference foil, the amplitude for the nanoparticles appears smaller which is obvious for small nanoparticles compared to bulk material. In addition, the amplitude of the alloy systems decreases with decreasing amount of palladium because of less amount of analyte in the sample. Concerning the peak position, the AuPd@SPB alloys show a high peak in the range of 1 – 2 Ågenerated by palladium atoms with an oxidation number of 2. However, the counterion of Pd^{2+} cannot be analyzed by EXAFS in this case. In this range of 1 – 2 Å only a small peak is present in the palladium foil spectrum. On the other hand, the main peak at the spectrum of the reference foil in the range of 2 – 3.5 Å which is the Pd-Pd peak results only in a small peak in case of the alloy systems.

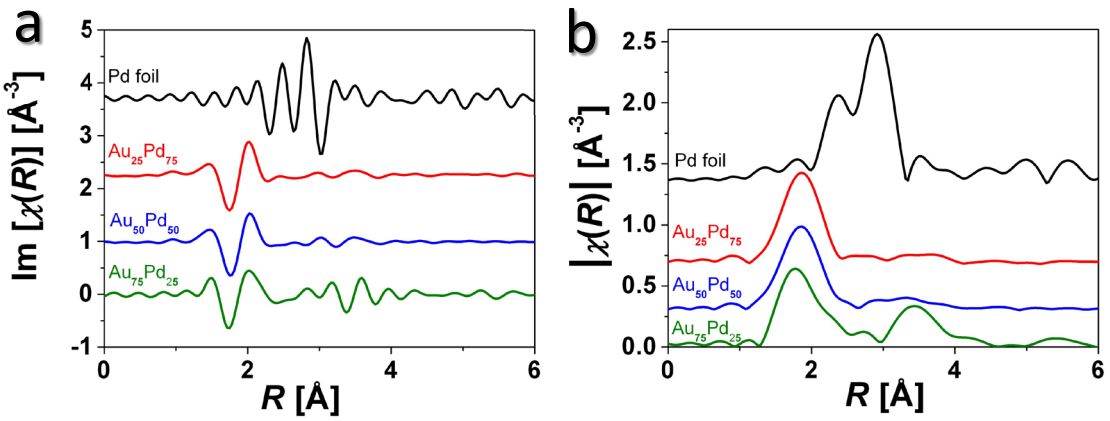

Figure 37: FT – chi(R) spectra of different AuPd@SPB alloy compositions at the Pd K absorption edge. The imaginary part (a) of the Fourier transformation and the magnitude (b) are displayed.[Faraday Discuss., 2013, Accepted Manuscript, DOI: 10.1039/C3FD20132E] - Reproduced by permission of The Royal Society of Chemistry.

The features of the nonmetallic palladium generate a strong peak between 1 – 2 Å compared to the Pd-Pd signal. Thus, qualitative evaluation is only achieved by fitting the experimental data with a theoretical model. The fit of each AuPd@SPB alloy system is displayed in Figure 38 together with the experimental data.

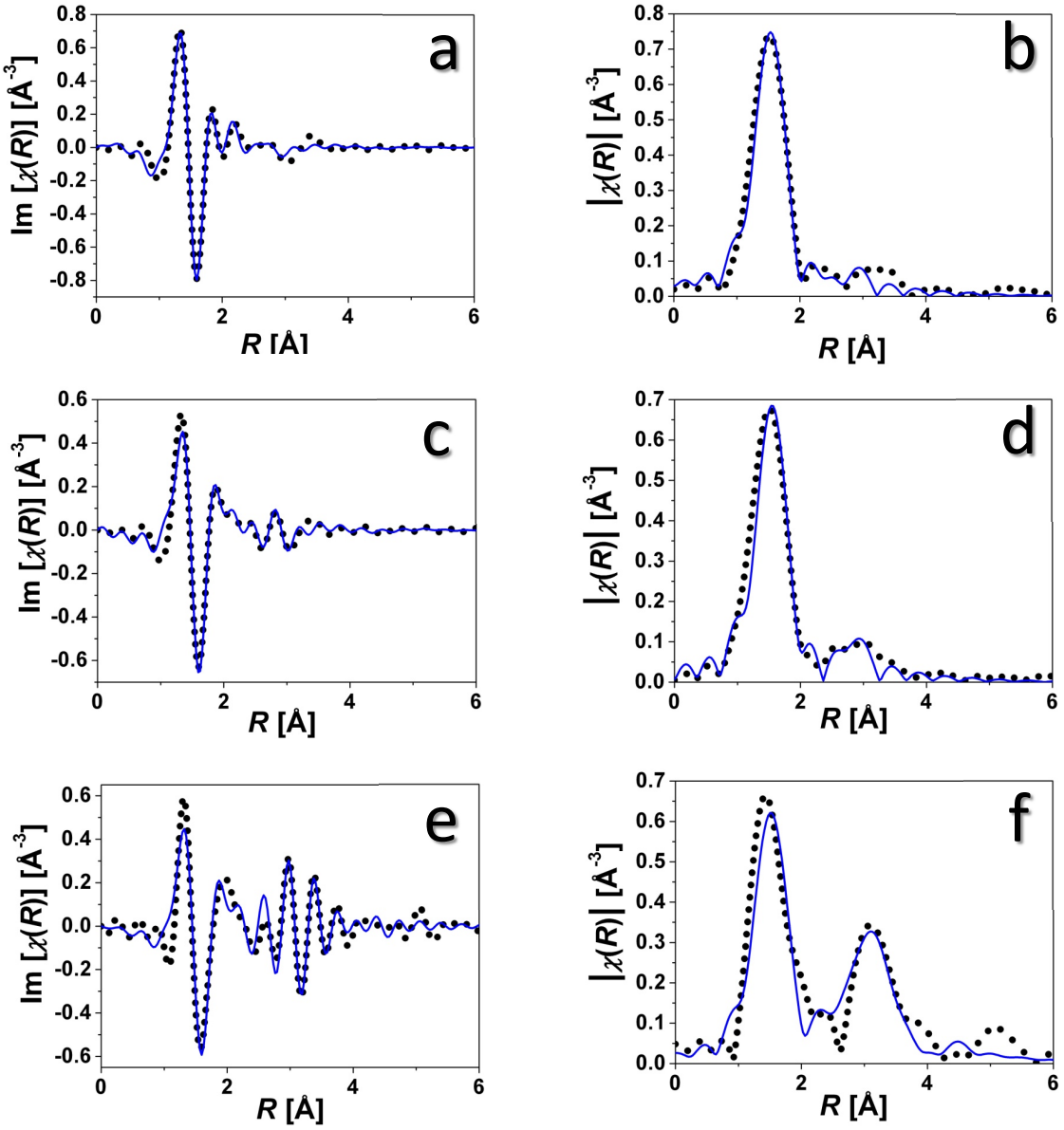

Figure 38: Fits and experimental data of the first coordination shell of $Au_{25}Pd_{75}$ (a, b), $Au_{50}Pd_{50}$ (c, d) and $Au_{75}Pd_{25}$ (e, f) nanoalloys displayed by the imaginary part (a, c, e) and the magnitude (b, d, f) of the FT spectra at the Pd K absorption edge. The fits are shown by blue lines and the experimental data by black dots, respectively.[Faraday Discuss., 2013, Accepted Manuscript, DOI: 10.1039/C3FD20132E] - Reproduced by permission of The Royal Society of Chemistry.

The parameters of the fits of AuPd@SPB nanoalloys at the Pd K absorption edge fromFigure 38 are summarized in Table 7 together with those of the Pd@SPB nanoparticle.

Table 7: Results of the EXAFS fitting parameters. N = Coordination number, N_{total} = sum of N at one absorption edge, R = interatomic distance, σ^2 = Debye-Waller Factor, ΔE_0 = inner core correction.[Faraday Discuss., 2013, Accepted Manuscript, DOI: 10.1039/C3FD20132E] - Reproduced by permission of The Royal Society of Chemistry.

Sample	Edge	Pair	N	N_{total}	R [Å]	σ^2 [Å^{-2}]	ΔE_0 [eV]
$Au_{75}Pd_{25}$	PdK	Pd-Pd	2.3± 0.3	7.3 ± 0.7	2.755 ± 0.044	0.0073 ± 0.0020	-4.9 ± 2.9
	PdK	Pd-Au	3.3± 0.2		2.791 ± 0.076	0.0073 ± 0.0020	-4.9 ± 2.9
	PdK	Pd^{2+}	1.7± 0.2		2.020 ± 0.022	0.0044 ± 0.0014	0.0 ± 0.6
$Au_{50}Pd_{50}$	PdK	Pd-Pd	0.4 ± 0.1	2.5 ± 0.4	2.764 ± 0.038	0.0073 ± 0.0030	0.5 ± 0.5
	PdK	Pd-Au	0.5 ± 0.2		2.789 ± 0.042	0.0073 ± 0.0030	0.5 ± 0.5
	PdK	Pd^{2+}	1.6 ± 0.1		2.051 ± 0.005	0.0014 ± 0.0008	0.5 ± 0.5
$Au_{25}Pd_{75}$	PdK	Pd-Pd	0.3 ± 0.1	2.2 ± 0.3	2.772 ± 0.004	0.0073 ± 0.0030	3.0 ± 0.4
	PdK	Pd-Au	0.4 ± 0.1		2.760 ± 0.004	0.0073 ± 0.0030	3.0 ± 0.4
	PdK	Pd^{2+}	1.5 ± 0.1		2.052 ± 0.004	0.0014 ± 0.0006	3.0 ± 0.4
Pd-NP	PdK	Pd-Pd	3.4 ± 0.2	5.4 ± 0.3	2.721 ± 0.004	0.0073 ± 0.0030	1.0 ± 0.4
	PdK	Pd^{2+}	2.0 ± 0.1		2.049 ± 0.003	0.0003 ± 0.0005	1.0 ± 0.4

First of all, attention should be paid to the neat palladium nanoparticles. The cluster size is approximately 1 nm which means that more than 70 % of the atoms are located at the surface of the particle. In the case that all of these surface atoms would be in the oxidation state of 2, N_{Pd2+} would be 70 % of N_{total} at the Pd K absorption edge for the neat palladium nanoparticle with a diameter of 1 nm. By the fitting parameters summarized in Table 7 it is clear that this condition is not fulfilled. Thus, the surface is not completely covered by Pd^{2+} and there is still a high amount of metallic palladium left. The small number of N_{total} is typical for such small nanoparticles. Furthermore the N_{total} values for the $Au_{50}Pd_{50}$ and $Au_{25}Pd_{75}$ alloys are small compared to those of palladium nanoparticles and the $Au_{75}Pd_{25}$ alloy system.

This means that a lot of palladium atoms are located at the surface for $Au_{50}Pd_{50}$ and $Au_{25}Pd_{75}$. Therefore a Pd_{core}-Au_{shell} structure is ruled out. Furthermore approximately 65 % ofN_{total} contributes to N_{Pd2+} for the $Au_{50}Pd_{50}$ and $Au_{25}Pd_{75}$ alloy system. This means that 65 % of the palladium atoms are in an oxidation state of 2 and only approximately 35 % of the palladium is metallic which is supposed to be located inside the particle. The argument for the latter aspect is the constant lattice pattern without any variation in contrast and atomic distance observed in the HR-TEM micrographs in chapter 4.1. Thus, the presence of Pd^{2+} is supposed at the surface of the particle only. Analyzing the N_{Pd-Pd} and N_{Pd-Au} values it is obtained from Table 7 that the ratio of N_{Pd-Pd} : N_{Pd-Au} does not at all reflect the ratio of Pd:Au in the alloy composition. Therefore a statistically mixing of homogeneous AuPd alloys is excluded for the $Au_{50}Pd_{50}$ and the $Au_{25}Pd_{75}$ alloy compositions. These findings accord well to the results from analyses at the Au L_3 absorption edge where slight enrichments of gold in the center and palladium at the surface of the particles are found. For the $Au_{75}Pd_{25}$ alloy composition the N_{total} value only differs little from the one at the Au L_3 absorption edge. The amount of Pd^{2+} is only approximately 30 % of the palladium atoms. Thus, much more metallic palladium atoms are present in contrast to the $Au_{50}Pd_{50}$ and the $Au_{25}Pd_{75}$ alloy compositions. In addition a higher amount of Pd-Pd bonds is found for the $Au_{75}Pd_{25}$ alloy composition by the parameters in Table 7 compared to Pd-Au bonds which suggests only very slight enrichment of palladium at the particle surface. These results for $Au_{75}Pd_{25}$ at the Pd K absorption edge confirm those found at the Au L_3 absorption edge. The final results for the atomistic arrangement of gold and palladium in AuPd@SPB alloys are illustrated in Figure 39in a schematic fashion and summed up as follows:

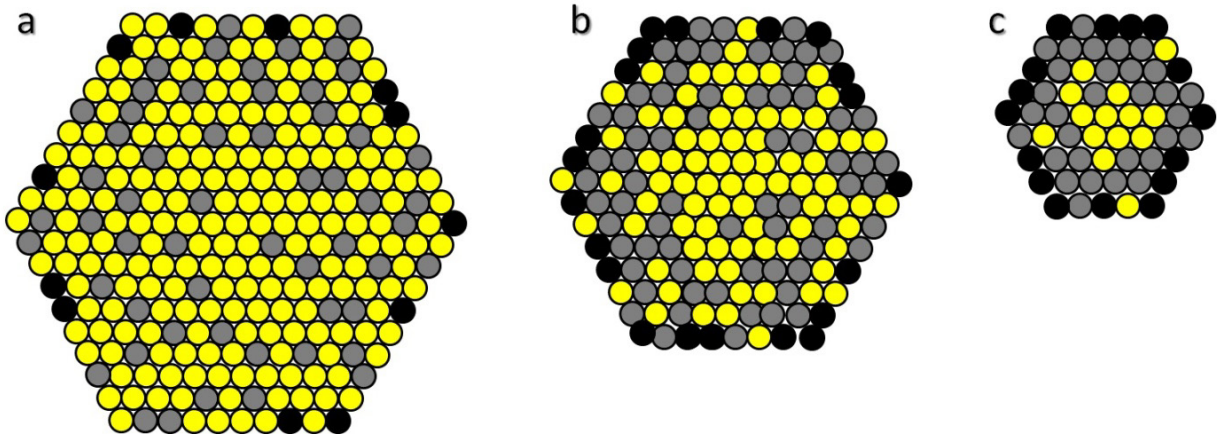

Figure 39: Scheme of the atomistic arrangement of $Au_{75}Pd_{25}$ (a), $Au_{50}Pd_{50}$ (b) and $Au_{25}Pd_{75}$(c) alloy systems stabilized in SPB. The yellow spheres represent gold atoms and the grey ones palladium, respectively. The black spheres illustrate the Pd^{2+} species. The illustration is schematic and does not reflect the exactly numbers of atoms of the different elements and atom species.

A core-shell structure can be excluded for all AuPd@SPB compositions in the present work. All compositions show slight enrichments of gold in the core and palladium at the surface. This effect is very weak in the case of the $Au_{75}Pd_{25}$ alloy system but becomes strong for the $Au_{25}Pd_{75}$ alloy composition. All compositions contain Pd^{2+} species which is supposed at the surface of the particles due to the well-defined constant lattice pattern observed in HR-TEM micrographs. The analyses of the atomistic arrangement of the $Au_{75}Pd_{25}$@SPB nanoalloy give evidence for an almost randomly mixed alloy system. These results are illustrated in a schematic fashion in Figure 39.Interestingly, this $Au_{75}Pd_{25}$@SPB alloy system shows the highest catalytic activity compared to other compositions which has been discussed in more detail in chapter 4.2.

4.3.2 Lattice Contraction of Gold Nanoparticles

The contraction of lattice parameters for small gold particles isa special behavior that differs nanoparticles in comparison to bulk material. In 1985 Balerna *et al.*[127] reported EXAFS studies on lattice parameters of gold nano clusters with different diameters in the range of 1.1 – 6.0 nm. An increase of lattice contraction has been found with decreasing particle size.[127]

Lattice contraction has been observed not only for small nanoparticles but also for thin metal films,[140] which are often made of noble metal layers like gold, produced by sputtering gold on a glass surface.[141] A significant change in the lattice parameter measured by XRD - measurements is reported for thin gold films less than 20 nm thickness.[141,142] For defined metal clusters, the coordination number could be predicted theoretically and additionally measured experimentally for instance by EXAFS studies. Benfield *et al.[138]* developed an ansatz for the calculations of the mean nearest-neighbor coordination number for gold nanoparticles.55 – atom fcc gold clusters show a coordination number of 7.9 instead of 12 as it is in the bulk gold.[138] These typical behaviors for the nano scale appear significant at less than 10 nm particle size[5] and increase extreme strongly at a range of approximately 3 nm.[168,169]However, shortening of bond length has been reported for gold nanoparticles, sometimes without paying attention to the dependence of different particle size.[28,72,170]

Nanda *et al.*[34] made a series of nanoparticles with different sizes, mainly gold nanoparticles, by evaporation. Free metal nanoparticles without polymeric stabilizers or carbon support can be prepared by this approach. Here, a linear dependence between the reciprocal of particle size and the lattice contraction was found. Furthermore surface energies and surface tension were calculated relating to the Kelvin effect. Both thermodynamical values were significant higher than that for bulk materials. [34,36,144,145,146,147,148] Xie *et al.*[149] developed a surface-to-volume depending ansatz to predict Nanda's experimental results theoretically.[149] As there is a direct dependence of inverse particle size and the surface-to-volume fraction, a lot of properties show this correlation.[6] Furthermore, a linear dependence between inverse particles size and surface energy was hard to find.[149] However, the influence of stabilizers and support materials can play a role to physical values as for instance bond length shortening.[150]

In the present study EXAFS analysis is used to evaluate the Au-Au bond length and to compare itwith different particle size and different particle support.Gold nanoparticles are stabilized bySPB and microgel. By variation of reaction conditions (temperature and injection speed of reducing agent), gold clusters in the size of

1.8 nm, 2.1 nm, and 2.7 nm diameter are synthesized respectively. In addition, gold nanoparticles of 4 nm diameter have been prepared using microgel as support.

For the smallestgold cluster (1.8 nm), the Fourier transform in the *R*-space is shown in Figure 40. A lattice contraction has been observed in Figure 40, which is marked by grey bars.

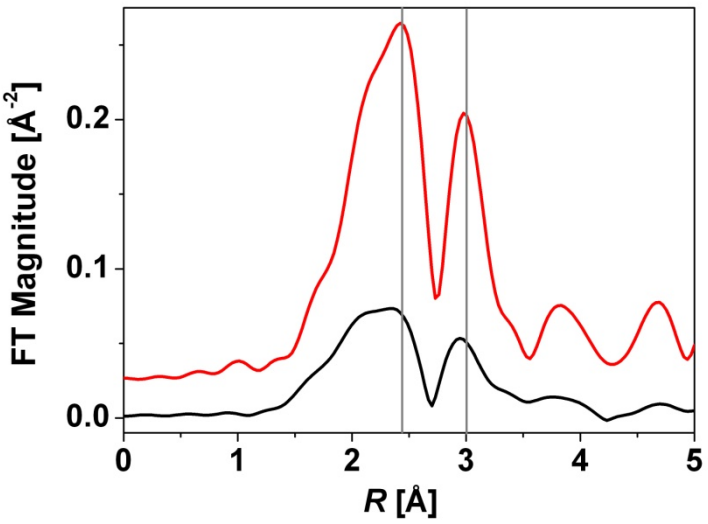

Figure 40: k^1-weighted magnitude of Fourier transform of the smallest gold particle with a diameter of 1.8 nm (black curve) and the reference foil (red curve). The grey bars mark the maxima of the reference foil.

This phenomenon can be found for all samples, where the contraction increases with decrease of the particle size. For further evaluation, the first coordination shell of all samples is fitted. In addition, the reference foil is fitted under same conditions. In case of the largest gold nanoparticle, the theoretical fit agrees well with the experimental data. Representative fits of SPB and microgel stabilized gold nanoparticles are shown as an example in Figure 41.

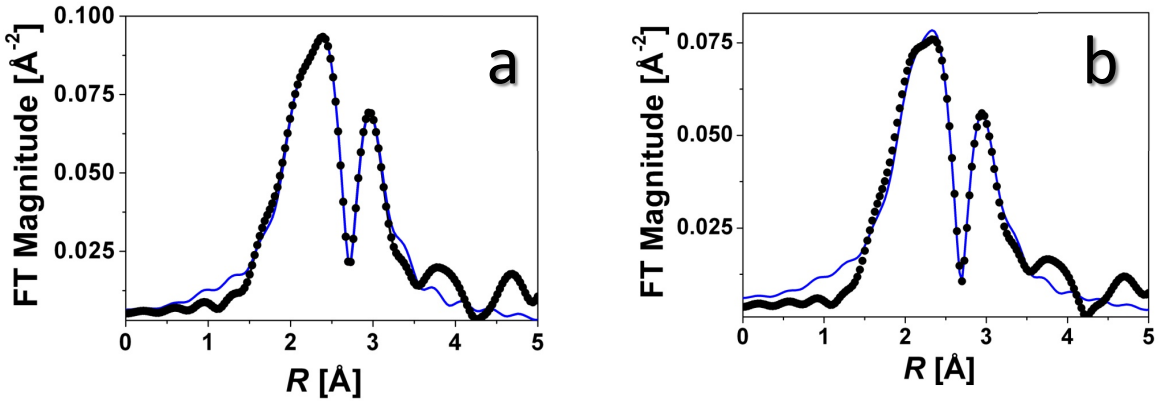

Figure 41: Fit for the 4 nm Au@gel nanoparticle (a) and for the 2.1 nm Au@SPB nanoparticle (b). Red dots: Fit; black lines: Experiment.

By comparison of lattice contraction according to the particle size a linear dependence is observed. The results are in good agreements with literature values as shown in Figure 42.

Balerna *et al.*[127] developed a model for the dependence of the lattice contraction on the particle size by studies on gold nanoparticles with different sizes. The highest lattice contraction (ca. 2.5 %) has been obtained for the smallest particle (1.1 nm diameter). It turned out that the shortening of interatomic bond length scales linear with the inverse particle size.

The attempt to explain this phenomenon is to calculate a surface tension of these nanoparticles by applying the liquid drop model by approximation. Thereby the linear dependence of the lattice contraction (ΔR) on the inverse particle size is discribed by following equation:

$$\Delta R = -\frac{4}{3} K R_b f \frac{1}{D} \qquad (9)$$

where ΔR is the change of the interatomic distance, Krepresents the bulk compressibility of the corresponding metal, $R_b$is the interatomic distance in the bulk material, f expresses the surface tension and D represents the particle diameter.

By equation (9), Balerna *et al.*[127] calculated a surface tension of nanoparticles in their study. Recently, Szczerba*et al.*[143] published EXAFS studies on gold

nanoparticles of different diameters. Two NIST (National Institute of Standards and Technology) references with 4.4 nm and 25.7 nm radius and a synthesized gold particle with 3.9 nm radius have been studied. The samples are citrate-stabilized and dispersed in water. For the particle with thesize of 3.9 nm a lattice contraction of 0.2 Å was calculated and 0.1 Å for the particle with a size of 4.4 nm. The large (25.7 nm) particle even shows a lattice expansion of approximately 0.1 Å. A linear dependence between reciprocal particle size and lattice contraction was observed similar to the results of Balerna*et al.*[127] and the surface tension could be calculated as
9.56 N m^{-1}.[143]

Present results and literature values of various sizes for gold nanoparticles are compared in good agreement and show different lattice contraction according to the particle size, where a linear dependence is observed. Sometimes,contraction of bond length in gold nanoparticles has been reported by other groups, when gold clusters and alloys are studied by EXAFS measurements, without paying attention to the correlation on the particle size.[28,72,170]The values of percental lattice contractionsfor different metal nanoparticle systemsare compared in Figure 42.

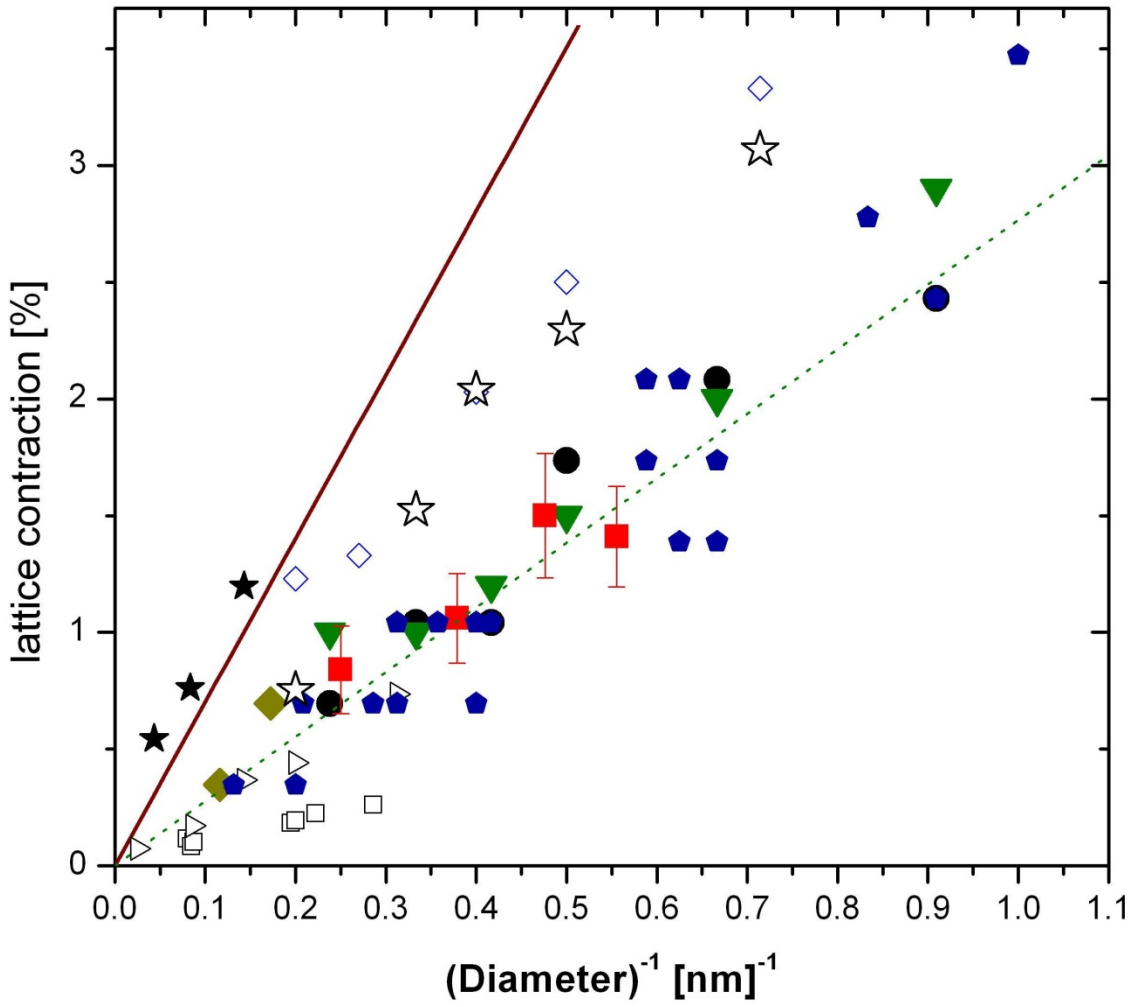

Figure 42: Comparison of different gold and palladium (stars) nanoparticles and the lattice contraction compared to their size: Open symbols represent electron diffraction measurements while filled symbols show results from EXAFS experiments. Filled triangles[127], spheres[127], diamonds[127] and squares (this study) show results of polymer stabilized particles. Filled pentagons[171] represent nanoparticles supported by SiO_2, Al_2O_3, TiO_2, CeO_2, Nb_2O_5 and ZrO_2. Open triangles[172] and squares[33] represent carbon supported particles. Open diamonds[173] show results of polymer stabilized gold nanoparticles. The green dashed line shows a mean square fit by a surface tension of 3.5 N m^{-1}. The red solid line represents a surface tension of 8.78 N/m, calculated by stabilizer-free gold nanoparticles.[34] Stars represent lattice contraction of palladium nanoparticles without stabilizing substrate measured by EXAFS (filled)[174] and embedded in polymer matrix evaluated by electron diffraction (open).[175]

The surface tension of gold nanoparticles calculated by the simple drop model is extremely high, namely in the dimension of approximately 3 to 10 N/m. Nada *et al.*[34] studied gold clusters of different particle sizes and calculated the surface

tension by size-dependent evaporation mode. Here, a surface tension of 8.78 N/m has been obtained. The work of Nada *et al.*[34] deals with free gold nanoparticles whereas most lattice parameters are observed by measurements on supported nanoparticles. Therefore the surface tension varies with different stabilizers in the range of 1.2 to 7.7 N/m.[33,34,148,172,173,176]

5. Conclusion and Outlook

The present work is concluded as follows:

1. Well-defined, facetted AuPd can be synthesized in spherical polyelectrolyte brushes (SPB) which has been demonstrated by HR-TEM, FFT and PXRD measurements. The nanoparticles show narrow size distributions in the range of 1 – 3 nm. These small AuPd nanoalloys can be synthesized in any Au:Pd ratio by employing SPB as stabilizer system. By theoretic calculations of the DOS it is found that the HOMO of the palladium atom changes depending on the location in the nanoalloy. Thus, the atomistic arrangement of the two different elements influences the electronic arrangement of AuPd nanoalloys.

2. The AuPd@SPB nanoalloys show higher catalytic activity compared to neat metal nanoparticles. By applying the reduction of 4-nitrophenol as benchmark reaction an alloy composition of 75 mol-% gold and 25 mol-% palladium shows the highest catalytic activity compared to different Au:Pd ratios. A correlation between this enhanced catalytic activity and the structural arrangement has been found as follows: HR-TEM analysis demonstrates that this $Au_{75}Pd_{25}$@SPB nanoalloy system contains thehighest number of surface defects compared to other Au:Pd ratios. The surface defects generate catalytically active sites on the surface of the catalyst which causes enhanced catalytic activity. Moreover, as determined by EXAFS measurements, this $Au_{75}Pd_{25}$@SPB nanoalloy system shows almost a randomly mixed alloy structure whereas slight enrichments of palladium at the surface of the nanoalloys and an increasing gold-gradient towards the center of the particles is found for the $Au_{50}Pd_{50}$@SPB and $Au_{25}Pd_{75}$@SPB nanoalloy systems. These findings are assumed to attribute to the higher catalytic activity of the $Au_{75}Pd_{25}$@SPB nanoalloy system.

3. The influence of the SPB system on the catalytic behavior is studied by comparison of support-free gold nanoparticles and SPB stabilized gold nanoparticles for the reduction of 4-nitrophenol. It turned out that the catalytic activity is similar in both cases which concludes that the SPB system does not influence the catalytic activity of the nanoparticles. Moreover, an induction period is observed for AuPd@SPB nanoalloys and support-freegold nanoparticles which accords to

previous studies on Au@SPB and Pt@SPB nanoparticles. This induction period represents a surface restructuring of the surface of the catalyst to activate the inactive pristine metal surface for the catalytic reaction. Comparison of this surface restructuring of support-free gold nanoparticles and SPB stabilized gold nanoparticles show that the restructuring process proceeds faster in the case of unsupported nanoparticles. Thus, the stabilizer system shows influence on the restructuring process in this case.

For possible future work in this research field further studies on support-free gold-palladium nanoalloys could be proposed to compare them to AuPd@SPB nanoalloys. In addition to that, synthesis and catalytic analysis of tri-metallic nanoalloy would probably draw high attention within the research community due to the benefits of three different metals concerning the promoting effect in terms of the catalytic activity.

6. Experimental and Data Processing

6.1 Analytical Methods

The metal content of the composite particles has been evaluated by TGA (thermo gravimetric analysis) using a Netsch STA 409PC LUXX®instrument. The suspension has been dried at 50 °C. Subsequently, approximately 15 mg of the sample has been used for TGA measurements by heating the sample to 800 °C where it has been kept for 1 h. The nitrogen flow during the measurement has been 30 mL/min. The heating rate has been 10 °C/min.

EDX (energy disperse X-ray) analysis has been performed at 200 keV in a Zeiss Libra 200 FE (200 keV) using a CM20 FEG equipped with a Noran Vantage system (Ge-detector) with about 2 nm beam diameter attached to a STEM equipment.

UV-Vis measurements have been performed by using a Lambda 650 spectrometer (Perkin Elmer) at a wavelength of 400 nm at 20 °C (using a Julabo F30-C thermostat) employing a Spectrosil® quartz glass cuvette (190 - 2700 nm, Roth).

HR-TEM images have been carried out at an objective-lens corrected FEI Titan 80-300 operating at an acceleration voltage of 300 keV.The aberration has been set to small negative values of the spherical aberration (below 200 nm).

For standard characterizations TEM images have been carried out by a CM30Philipsmicroscopeoperatingatanaccelerationvoltageof300keV.

6.2 Materials

Cetyltrimethylammonium bromide (CTAB)	Fluka
2-aminoethylmethacrylate hydrochloride (AEMH)	Polyscience
2,2’-azobis(2-amidinopropane)dihydrochloride (V50)	Aldrich
tetrachloroauric acid trihydrate	Aldrich
sodium tetrachloropalladate	Aldrich
4-nitrophenol	Aldrich

Styrene	BASF
Sodium borohydride	Merk
Pyridine	Aldrich
Irgacure	BASF
Methacryloyl chloride	Sigma

6.3 Synthesis of Spherical Polyelectrolyte Brushes

The polystyrene cores have been synthesized as follows: 3.6 g CTAB (Cetyltrimethylamonium bormide) has been dissolved in 530 g Millipore water at 30 °C. This solution has been stirred at 30 °C for 1 h to dissolve the CTAB completely. 138 g styrene has been purged with nitrogen for 10 min and added to the solution (which has been purged with nitrogen as well). 0.44 g V50 (2,2'-azobis(2-amidinopropane)dihydrochloride) has been dissolved in 27 g Millipore water and added to the reaction mixture. The reaction has been allowed to proceed for 2 h at 65 °C. Then 18.45 g HMEM solution (42 wt-%) diluted with 18.5 g aceton has been added to the reaction mixture and the reaction has been continued for 5.5 h at 65 °C. Afterwards,the reaction mixture has been stirred at room temperature overnight. The polystyrene cores have been purified by ultrafiltration with Millipore wateruntil the eluate reaches an electronic conductivity of 20 µS/cm. The core size has been determined by TEM.

The photo initiator (HMEM) has been synthesized as follows: 95 g Irgacure has been dissolved in 600 mL acetone at 30 °C. Afterwards the solution has been cooled to approximately 0 °C and 50 g pyridine has been added. Subsequently, 43.3 g methacryloyl chloride has been added in five steps: 12.5 g have been added at the beginning and after 1 h. After one additional hour 11.7 g have been added and after another hour 6.6 g. The reaction mixture has been stirred overnight. Afterwards, acetone has been removed (by a rotary evaporator) and the product has been purified by water extraction 8 times. Subsequently, further purification by a silicon column has been achieved using a solvent mixture of acetone : hexane (1:2).

Finally, 201.6 g of the previous synthesized polystyrene-HMEM cores (9.3 wt %)

have been diluted with 484 g Millipore water. A solution of 14.02 g the monomer AEMH (2-aminoethylmethacrylate hydrochloride) has been diluted in 50 g Millipore water and added to the polystyrene-HMEM suspension. The reaction mixture is polymerized in an UV-reactor for one hour. Detailed information about the polymerization by the UV-reactor is given in reference[55]and[177].

6.4 Synthesis of Metal Nanoparticles

The AuPd@SPB nanoalloys as well as neat metal nanoparticles have been synthesized as follows: The molar ratio between Au and Pd has been set by the ratio of the noble metal salts. Au@SPB and Pd@SPB nanoparticles have been synthesized by adding only one of the noble metal salts. The reaction solution as well as Millipore water has been purged by nitrogen to exclude oxygen during the reaction. The reaction mixture has been stirred during the whole reaction process. In a typical run, $HAuCl_4$ and Na_2PdCl_4 have been dissolved in 5 mL water, respectively. The SPB suspension has been diluted till a concentration of 0.1 wt-% (solid content) has been achieved. The $HAuCl_4$ solution has been added drop wise to 100 mL of this diluted SPB suspension. Afterwards the Na_2PdCl_4 has been added drop wise. The total amount of metal salt in the reaction mixture has always been 4.5×10^{-5} mol. The reaction has been cooled in an ice bath. After 2 h, $NaBH_4$ (0.011 g, dissolved in 10 mL Millipore water) has been added drop wise within 30 min. The solution turned form pale yellow into grey in the case of the synthesis of AuPd@SPB and Pd@SPB and red in the case of the Au@SPB synthesis. This color change has been visible from the first drop of $NaBH_4^{(aq)}$ on. The reaction mixture has been stirred for additional 3 h at approximately 0 °C and purified afterward by ultra-filtration with Millipore water until the eluate reached an electric conductivity of 2 µS/cm. In the case of Au@SPB nanoalloys with different sizes the reaction conditions have been changed as follows: for the small particles (1.8 nm) the injection of $NaBH_4^{(aq)}$ has been done slowly (twice the injection time for the same amount as previous (0.011 g)) and the amount of metal salt has been half of the amount of the standard method (0.0056 g $HAuCl_4$ instead of 0.011 g). The reaction has been carried out at a temperature of approximately 0 °C in the reaction mixture, too.A particle size of

approximately 2.1 nm has been achieved byfaster injection at room temperature. The amount of $NaBH_4$ has been 0.044 g. In the case of large gold nanoparticles (2.7 nm) the synthesis has been performed as described previously for the Au@SPB nanoparticles at the beginning of this paragraph.

6.5 CatalyticAnalysis

The catalysis measurements have been carried out at 20 °C. The specimen volume for the UV-Vis measurement has been 3 mL at every run. First, to a solution of 0.1 mol/L Nip (4-nitrophenol), 10 mol/L BH_4 (borohydride) a certain amount of catalyst has been added. The catalyst amount has been varied to find the dependence of k_{app} on the surface of the catalyst. Subsequently, the concentration of the catalyst has been kept constant at varying concentrations of Nip and BH_4. During constant concentrations of BH_4 (10 mmol/L and 5 mmol/L, respectively) following concentrations for Nip have been chosen (in [mmol/L]): 0.02, 0.03, 0.04, 0.05, 0.07, 0.10, 0.15 and 0.20. In the case of constant concentrations of Nip (0.1 mmol/L and 0.05 mmol/L, respectively) following concentrations for BH_4 have been chosen (in [mmol/L]): 2, 3, 5, 6, 10and 15. UV-Vis measurements have been performed at a wavelength of 400 nm.The total surface area in the reaction mixture has been calculated by the particle diameter (from TEM micrographs) by assuming spherical shape for the nanoparticles and the metal content of the composite particles from TGA. The density of the bimetallic nanoalloy system has been calculated by the equation $\rho(\mathrm{AuPd}) = (m_{Au} + m_{Pd}) / (m_{Au} / \rho_{Au} + m_{Pd} / \rho_{Pd})$ withρ_{Au} = 19.32 g/cm^3 and ρ_{Pd} = 12.02 g/cm^3.

6.6 EXAFS Measurements

EXAFS measurements were performed at three different beamlines: the KMC2 at BESSY (the former Berliner Elektronenspeicherring-Gesellschaft für Synchrotronstrahlung in Berlin, now Helmholtz-Zentrum Berlin), the BAMline at BESSY and the X – Beamline at DESY (Deutsches Elektronen-Synchrotron in

Hamburg). The measurements at the BAMline were carried out by cooperation partners at the BAM (Bundesanstalt für Materialforschung und –prüfung)

The samples have been freeze dried and filled in small holes (4 mm diameter) of a plastic plate which has been fixed on the sample stage at the beamline. The holes were sealed by Kapton®tape. The thickness of the samples has been 2 mm.

6.6.1 BESSY – KMC2

The energy range was set from 11400 to 12719 eV including the Au L_3 absorption edge at 11919 eV. The energy range was set by the monochromator. The monochromator used at KMC2 is a double Bragg(111) Si-Ge grandent concentration crystal with a germanium concentration of approximately 10 % varying along the crystal.

The geometry at the sample stage allowed measurements in transmission mode and fluorescence mode simultaneously. All measurements were carried out in transmission-mode and fluorescence mode. Therefore the sample has been placed in an angle of 45 ° to the X-ray beam and the fluorescence detector has been adjusted in an angle of 90 ° to the X-ray beam, respectively. The transmission signal has been collected by an Oxford Danfysik IC PLUS 50 ion chamber. The fluorescence signal has been detected by a X-Flash Silicon drift detector (SDD) from Bruker. However, the transmission mode signal for the samples did not show usable signal-to-noise ratios. Thus, the fluorescence signal has been used for data evaluation.

6.6.2 BESSY – BAMline

EXAFS measurements of bimetallic AuPd nanoalloys have been performed at the Pd Kedge (E_0 = 24350 eV) and additional at the Au L_3edge (E_0 = 11919 eV) at the BAMline at BESSY. As monochromator a double-crystal monochromator, DCM, Si(111) with an energy resolution of about 2 x 10^{-4} has been employed. The signals

have been collected in a standard 45° geometry mode employing an energy dispersive silicon drift detector. The incident beam intensity has been detected by an ion chamber.

6.6.3 DESY – HASYLAB: X – Beamline

The energy range has been chosen analogous to the parameters at the KMC2 beamline (11400 – 12719 eV, Au L_3 absorption edge: 11919 eV). The energy has been set by two Si(111) crystals as a double crystal monochromator. The spot size of the incident beam has been set to 2.5 x 1.0 mm (width x height).

Measurements have been carried out in transmission and fluorescence mode simultaneously. In addition the reference foil has been measured in transmission mode simultaneously by following setup:

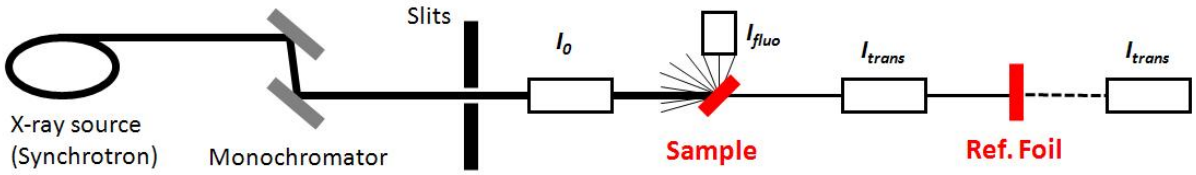

Figure 43: Schematic setup for EXAFS measurements at the X-beamline at DESY/HasyLab. The detectors are marked as follows: I_0 denotes the ion camber which detects the incident beam, I_{trans} detects the transmission signal from the sample or the reference foil, respectively. I_{fluo} collects the fluorescence signals.

The fluorescence signal has been collected by a multi(7)-element Si(Li) detector (CANBERRA, Analytical Instruments) placed in an angle of 90 ° to the X-ray beam. For the detection of the transmission signals, ion chambers have been used before and after the X-ray beam penetrated the sample and after the X-ray penetrated the reference foil (as shown in a schematic fashion in Figure 43). The transmission signal has been collected by (in-house made) ion chambers filled with following gas for measurements at the Au L_3 absorption edge: detection of the incident beam signal: argon (165 mbar); detection after the X-ray beam penetrated the sample: krypton (662 mbar); detection of the transmission signal of the reference foil: krypton (1 bar). At the Pd K absorption edge all three ion chamber have been filled with krypton of

following pressure: detection of the incident beam signal: 95 mbar; detection after the X-ray beam penetrated the sample: 627 mbar; detection of the transmission signal of the reference foil: 1 bar.The length of all ionization chambers is 10 cm. Furthermore Keithley 428 nanoAmpere meters have been employed to measure the current in the ion chambers.

6.7 EXAFS Data Evaluation

Data of EXAFS measurements have been fitted by the EXAFS equation (see equation(10)):

$$chi_i(k) = \frac{(N_i S_0^2) F_{eff,i}(k)}{kR_i^2} \sin\left[2kR_i + \varphi_i(k)\right] e^{-2\sigma_i^2 k^2} e^{\frac{-2R_i}{\lambda(k)}} \qquad (10)$$

where $chi_i(k)$ is the Fourier transformed oscillation region (after transformation to the k-vektor) of a certain absorber i. $F_{eff,i}(k)$, $\varphi_i(k)$ and $\lambda(k)$ are the effective scattering amplitude of the photoelectron, the phase shift of the photoelectron and the mean free path of the photoelectron, respectively. N_i represents the coordination number (CN). S_0^2 is the passive electron reduction factor and σ^2 is the mean square displacement of the bond length between the absorbing and scattering atom which represents the thermal disorder. R_i represents the half path length of the photoelectron.[29] The data reduction and fitting process has been performed by recommendations of S.D. Kelly[29] and B.K. Teo[30] where further detailed information about the theory of the EXAFS equation including information about the data reduction and fitting process can be found.

The evaluation and simulation of the spectra have been performed by using the codes ATOMS, AUTOBK, FEFF and FEFFIT.[29] For data fitting CIF (crystal identification file) of palladium and gold has been used for fitting the neat metal nanoparticles. For the AuPd nanoalloys the CIF has been modified as follows: Starting form an Au CIF, gold atoms have been replaced by palladium atoms while the interatomic distance (d_{AuPd}) has been calculated as ½(d_{AuAu} + d_{PdPd}). An example for the modified CIF as FEFF input file at the Au L_3 absorption edge is shown in

Figure 44.

```
                                        Unbenannt
* This feff6 input file was generated by Artemis 0.8.012
* Atoms written by and copyright (c) Bruce Ravel, 1998-2001

* -- * -- * -- * -- * -- * -- * -- * -- * -- * -- * -- * -- * -- * -- * -- *
*   total mu*x=1:     2.80 microns,  unit edge step:    19.13 microns
*   specific gravity = 19.310
* -- * -- * -- * -- * -- * -- * -- * -- * -- * -- * -- * -- * -- * -- * -- *
*   Normalization correction:    0.00042 ang^2
* -- * -- * -- * -- * -- * -- * -- * -- * -- * -- * -- * -- * -- * -- * -- *

* ---------------------------------------------------------------------
* The following crystallographic data were used:
*
* title        Gold
* title        Au
* title        Wyckoff, R. W. G.
* title         Second edition. Interscience Publishers, New York, New York
* title         Cubic closest packed, ccp, structure
* space = F m -3 m
* a =    4.07825       b =       4.07825       c =       4.07825
* alpha =       90.0   beta =   90.0   gamma =  90.0
* core =       Au      edge =  L3
* atoms
* ! elem   x          y          z       tag        occ
*   Au    0.00000    0.00000    0.00000  Au            1.00000
* ---------------------------------------------------------------------


TITLE Gold
TITLE Au
TITLE Wyckoff, R. W. G.
TITLE  Second edition. Interscience Publishers, New York, New York
TITLE  Cubic closest packed, ccp, structure

HOLE 4   1.0   *  Au L3 edge  (11919.0 eV), second number is S0^2

*         mphase,mpath,mfeff,mchi
CONTROL   1      1     1     1
PRINT     1      0     0     0

RMAX        4.48608

*CRITERIA     curved   plane
*DEBYE        temp     debye-temp
NLEG         4

POTENTIALS
*    ipot   Z  element
       0   79   Au
       1   79   Au
       2   46   Pd

ATOMS                          * this list contains 19 atoms
*   x          y          z      ipot  tag             distance
   0.00000    0.00000    0.00000  0 Au              0.00000
   1.98975    1.98975    0.00000  2 Pd_1            2.81400
  -2.03912    2.03912    0.00000  1 Au_1            2.88375
   1.98975   -1.98975    0.00000  2 Pd_1            2.81400
  -2.03912   -2.03912    0.00000  1 Au_1            2.88375
   1.98975    0.00000    1.98975  2 Pd_1            2.81400
  -1.98975    0.00000    1.98975  2 Pd_1            2.81400
   0.00000    2.03912    2.03912  1 Au_1            2.88375
   0.00000   -2.03912    2.03912  1 Au_1            2.88375
   1.98975    0.00000   -1.98975  2 Pd_1            2.81400
  -1.98975    0.00000   -1.98975  2 Pd_1            2.81400
   0.00000    2.03912   -2.03912  1 Au_1            2.88375
   0.00000   -2.03912   -2.03912  1 Au_1            2.88375
   4.07825    0.00000    0.00000  1 Au_2            4.07825
  -4.07825    0.00000    0.00000  1 Au_2            4.07825
   0.00000    4.07825    0.00000  1 Au_2            4.07825
   0.00000   -4.07825    0.00000  1 Au_2            4.07825
   0.00000    0.00000    4.07825  1 Au_2            4.07825
   0.00000    0.00000   -4.07825  1 Au_2            4.07825
END
```

Figure 44: Modified Au CIF for the model of the $Au_{50}Pd_{50}$@SPB EXAFS data.

Data at the Pd K absorption edge have been fitted analogous. In a Pd CIF the palladium atoms have been replaced by gold atoms and the distances have been changed by ½(d_{AuAu} + d_{PdPd}) equal to the modification for the data at the Au L_3 edge. In addition a second FEFF input file has been applied with Pd surrounded by four oxygen atoms to fit the Pd^{2+} signal. Here it should be mentioned again, that this model does not give evidence of O^{2-} as a counterion for Pd^{2+}. By EXAFS measurements in the present work it has not been possible to determine the counterion of Pd^{2+} the species.

7. Annex

7.1 Bibliography

[1] Herves, Pablo; Perez-Lorenzo, Moises; Liz-Marzan, Luis M.; Dzubiella, Joachim; Lu, Yan and Ballauff, Matthias (2012): Catalysis by metallic nanoparticles in aqueous solution: model reactions, Chemical Society Reviews. URL: http://dx.doi.org/10.1039/C2CS35029G

[2] Astruc, D. (2007): Nanoparticles and Catalysis, Wiley-VCH Verlag GmbH & Co. KGaA, Weinheim, ISBN: 978-3-527-31572-7.

[3] Ghosh, S. K. and Pal, T. (2007): Interparticle coupling effect on the surface plasmon resonance of gold nanoparticles: From theory to applications, Chemical Reviews (vol. 107), No. 11, pp. 4797-4862. URL: <Go to ISI>://WOS:000250970400008

[4] Daniel, M. C. and Astruc, D. (2004): Gold nanoparticles: Assembly, supramolecular chemistry, quantum-size-related properties, and applications toward biology, catalysis, and nanotechnology, Chemical Reviews (vol. 104), No. 1, pp. 293-346. URL: <Go to ISI>://WOS:000188217400009

[5] Sun, C. Q. (2007): Size dependence of nanostructures: Impact of bond order deficiency, Progress in Solid State Chemistry (vol. 35), No. 1, pp. 1-159. URL: <Go to ISI>://WOS:000243123000001

[6] Roduner, E. (2006): Size matters: why nanomaterials are different, Chemical Society Reviews (vol. 35), No. 7, pp. 583-592. URL: <Go to ISI>://WOS:000238475400001

[7] Ferrando, R.; Jellinek, J. and Johnston, R. L. (2008): Nanoalloys: From theory to applications of alloy clusters and nanoparticles, Chemical Reviews (vol. 108), No. 3, pp. 845-910. URL: <Go to ISI>://WOS:000253947800001

[8] Toshima, N. and Yonezawa, T. (1998): Bimetallic nanoparticles - novel materials for chemical and physical applications, New Journal of Chemistry (vol. 22), No. 11, pp. 1179-1201. URL: <Go to ISI>://WOS:000077548800014

[9] Emory, S. R. and Nie, S. (1998): Screening and enrichment of metal nanoparticles with novel optical properties, Journal of Physical Chemistry B (vol. 102), No. 3, pp. 493-497. URL: <Go to ISI>://WOS:000071802700002

[10] Colvin, V. L.; Schlamp, M. C. and Alivisatos, A. P. (1994): LIGHT-EMITTING-DIODES MADE FROM CADMIUM SELENIDE NANOCRYSTALS AND A SEMICONDUCTING POLYMER, Nature (vol. 370), No. 6488, pp. 354-357. URL: <Go to ISI>://WOS:A1994PA30400050

[11] Haruta, M.; Kobayashi, T.; Sano, H. and Yamada, N. (1987): Novel Gold Catalysts for the Oxidation of Carbon-Monoxide at a Temperature Far Below 0-Degrees-C, Chemistry Letters, No. 2, pp. 405-408. URL: <Go to ISI>://A1987G439800050

[12] Sun, T. and Seff, K. (1994): SILVER CLUSTERS AND CHEMISTRY IN ZEOLITES, Chemical Reviews (vol. 94), No. 4, pp. 857-870. URL: <Go to ISI>://WOS:A1994NT84800001

[13] Enache, D. I.; Edwards, J. K.; Landon, P.; Solsona-Espriu, B.; Carley, A. F.; Herzing, A. A.; Watanabe, M.; Kiely, C. J.; Knight, D. W. and Hutchings, G. J. (2006): Solvent-free oxidation of primary alcohols to aldehydes using Au-Pd/TiO2 catalysts, Science (vol. 311), No. 5759, pp. 362-365. URL: <Go to ISI>://WOS:000234938500039

[14] Hashmi, A. S. K. and Hutchings, G. J. (2006): Gold catalysis, Angewandte Chemie-International Edition (vol. 45), No. 47, pp. 7896-7936. URL: <Go to ISI>://000242781200008

[15] Hutchings, G. J. (2008): Nanocrystalline gold and gold-palladium alloy oxidation catalysts: a personal reflection on the nature of the active sites, Dalton Transactions, No. 41, pp. 5523-5536. URL: <Go to ISI>://WOS:000260023300001

[16] Hutchings, G. J. (1985): Vapor-Phase Hydrochlorination of Acetylene - Correlation of Catalytic Activity of Supported Metal Chloride Catalysts, Journal of Catalysis (vol. 96), No. 1, pp. 292-295. URL: <Go to ISI>://A1985ASX7000030

[17] Corma, A. and Garcia, H. (2008): Supported gold nanoparticles as catalysts for organic reactions, Chemical Society Reviews (vol. 37), No. 9, pp. 2096-2126. URL: <Go to ISI>://000259408300024

[18] Arcadi, A. (2008): Alternatice Synthetic Methodes through New Development in Catalsysis by Gold, Chemical Reviews (Washington, D. C.) (vol. 108), p. 60.

[19] Della Pina, C.; Falletta, E.; Prati, L. and Rossi, M. (2008): Selective oxidation using gold, Chemical Society Reviews (vol. 37), No. 9, pp. 2077-2095. URL: <Go to ISI>://000259408300023

[20] Della Pina, C.; Falletta, E. and Rossi, M. (2012): Update on selective oxidation using gold, Chemical Society Reviews (vol. 41), No. 1, pp. 350-369. URL: <Go to ISI>://WOS:000297654700018

[21] Gong, J. L. (2012): Structure and Surface Chemistry of Gold-Based Model Catalysts, Chemical Reviews (vol. 112), No. 5, pp. 2987-3054. URL: <Go to ISI>://WOS:000303698000012

[22] Yang, J.; Deng, S. Y.; Lei, J. P.; Ju, H. X. and Gunasekaran, S. (2011): Electrochemical synthesis of reduced graphene sheet-AuPd alloy nanoparticle composites for enzymatic biosensing, Biosensors & Bioelectronics (vol. 29), No. 1, pp. 159-166. URL: <Go to ISI>://WOS:000296174700025

[23] Tang, L. L.; Yu, G.; Si, W. W.; Ou, Y. J. and Qiao, L. J. (2011): Pd-Ag Alloy Dendritic Nanowires: Fabrication and Application in Hydrogen Sensor, Journal of Nanoscience and Nanotechnology (vol. 11), No. 11, pp. 10255-10261. URL: <Go to ISI>://WOS:000298765800160

[24] Dimitratos, N.; Lopez-Sanchez, J. A.; Anthonykutty, J. M.; Brett, G.; Carley, A. F.; Tiruvalam, R. C.; Herzing, A. A.; Kiely, C. J.; Knight, D. W. and Hutchings, G. J. (2009): Oxidation of glycerol using gold-palladium alloy-supported nanocrystals, Physical Chemistry Chemical Physics (vol. 11), No. 25, pp. 4952-4961. URL: <Go to ISI>://WOS:000267499400005

[25] Mayoral, A.; Deepak, F. L.; Esparza, R.; Casillas, G.; Magen, C.; Perez-Tijerina, E. and Jose-Yacaman, M. (2012): On the structure of bimetallic noble metal nanoparticles as revealed by aberration corrected scanning transmission electron microscopy (STEM), Micron (vol. 43), No. 4, pp. 557-564. URL: <Go to ISI>://WOS:000301702400010

[26] Deepak, F. L.; Casillas-Garcia, G.; Esparza, R.; Barron, H. and Jose-Yacaman, M. (2011): New insights into the structure of Pd-Au nanoparticles as revealed by aberration-corrected STEM, Journal of Crystal Growth (vol. 325), No. 1, pp. 60-67. URL: <Go to ISI>://WOS:000292666700012

[27] Kesavan, L.; Tiruvalam, R.; Ab Rahim, M. H.; bin Saiman, M. I.; Enache, D. I.; Jenkins, R. L.; Dimitratos, N.; Lopez-Sanchez, J. A.; Taylor, S. H.; Knight, D. W.; Kiely, C. J. and Hutchings, G. J. (2011): Solvent-Free Oxidation of Primary Carbon-Hydrogen Bonds in Toluene Using Au-Pd Alloy Nanoparticles, Science (vol. 331), No. 6014, pp. 195-199. URL: <Go to ISI>://WOS:000286433100037

[28] Liu, F.; Wechsler, D. and Zhang, P. (2008): Alloy-structure-dependent electronic behavior and surface properties of Au-Pd nanoparticles, Chemical Physics Letters (vol. 461), No. 4-6, pp. 254-259. URL: <Go to ISI>://WOS:000258395300018

[29] S. D. Kelly, D. Hesterberg, and B. Ravel (2008): Analysis of soils and minerals using X-ray absorption spectroscopy, Methods of Soil Analysis– Part 5. Mineralogical Methods, Soil Sci. Soc. Am., Madison.

[30] Teo, Boon Keng (1986): EXAFS : basic principles and data analysis ; with 17 tables, Inorganic chemistry concepts, Springer, Berlin [u.a.], ISBN: 35401583320387158332.

[31] Gu, Z. J.; Xiang, X.; Fan, G. L. and Li, F. (2008): Facile Synthesis and Characterization of Cobalt Ferrite Nanocrystals via a Simple Reduction-Oxidation Route, Journal of Physical Chemistry C (vol. 112), No. 47, pp. 18459-18466. URL: <Go to ISI>://WOS:000261056500027

[32] King, A. G. and Keswani, S. T. (1994): COLLOID MILLS - THEORY AND EXPERIMENT, Journal of the American Ceramic Society (vol. 77), No. 3, pp. 769-777. URL: <Go to ISI>://WOS:A1994NB05500025

[33] Mays, C. W.; Vermaak, J. S. and Kuhlmann.D (1968): ON SURFACE STRESS AND SURFACE TENSION .2. DETERMINATION OF SURFACE STRESS OF GOLD,

Surface Science (vol. 12), No. 2, pp. 134-&. URL: <Go to ISI>://WOS:A1968C184000003

[34] Nanda, K. K.; Maisels, A. and Kruis, F. E. (2008): Surface tension and sintering of free gold nanoparticles, Journal of Physical Chemistry C (vol. 112), No. 35, pp. 13488-13491. URL: <Go to ISI>://WOS:000258800700033

[35] Via, G. H.; Drake, K. F.; Meitzner, G.; Lytle, F. W. and Sinfelt, J. H. (1990): ANALYSIS OF EXAFS DATA ON BIMETALLIC CLUSTERS, Catalysis Letters (vol. 5), No. 1, pp. 25-33. URL: <Go to ISI>://A1990DC47500004

[36] Vanithakumari, S. C. and Nanda, K. K. (2008): A universal relation for the cohesive energy of nanoparticles, Physics Letters A (vol. 372), No. 46, pp. 6930-6934. URL: <Go to ISI>://WOS:000261757700023

[37] Barcikowski, S.; Menendez-Manjon, A.; Chichkov, B.; Brikas, M. and Raciukaitis, G. (2007): Generation of nanoparticle colloids by picosecond and femtosecond laser ablations in liquid flow, Applied Physics Letters (vol. 91), No. 8. URL: <Go to ISI>://WOS:000248984800087

[38] Wagener, P.; Schwenke, A. and Barcikowski, S. (2012): How Citrate Ligands Affect Nanoparticle Adsorption to Microparticle Supports, Langmuir (vol. 28), No. 14, pp. 6132-6140. URL: <Go to ISI>://WOS:000302514800030

[39] Gondal, M. A.; Saleh, T. A. and Drmosh, Q. A. (2012): Synthesis of nickel oxide nanoparticles using pulsed laser ablation in liquids and their optical characterization, Applied Surface Science (vol. 258), No. 18, pp. 6982-6986. URL: <Go to ISI>://WOS:000304004100041

[40] Zeng, H. B.; Du, X. W.; Singh, S. C.; Kulinich, S. A.; Yang, S. K.; He, J. P. and Cai, W. P. (2012): Nanomaterials via Laser Ablation/Irradiation in Liquid: A Review, Advanced Functional Materials (vol. 22), No. 7, pp. 1333-1353. URL: <Go to ISI>://WOS:000302346400003

[41] Amendola, V. and Meneghetti, M. (2009): Laser ablation synthesis in solution and size manipulation of noble metal nanoparticles, Physical Chemistry Chemical Physics (vol. 11), No. 20, pp. 3805-3821. URL: <Go to ISI>://WOS:000266065400001

[42] Semaltianos, N. G. (2010): Nanoparticles by Laser Ablation, Critical Reviews in Solid State and Materials Sciences (vol. 35), No. 2, pp. 105-124. URL: <Go to ISI>://WOS:000278705100002

[43] Muto, H.; Yamada, K.; Miyajima, K. and Mafune, F. (2007): Estimation of surface oxide on surfactant-free gold nanoparticles laser-ablated in water, Journal of Physical Chemistry C (vol. 111), No. 46, pp. 17221-17226. URL: <Go to ISI>://WOS:000251024500013

[44] Peng, X. H.; Pan, Q. M. and Rempel, G. L. (2008): Bimetallic dendrimer-encapsulated nanoparticles as catalysts: a review of the research advances, Chemical Society Reviews (vol. 37), No. 8, pp. 1619-1628. URL: <Go to ISI>://000257839100015

[45] Myers, V. S.; Weir, M. G.; Carino, E. V.; Yancey, D. F.; Pande, S. and Crooks, R. M. (2011): Dendrimer-encapsulated nanoparticles: New synthetic and characterization methods and catalytic applications, Chemical Science (vol. 2), No. 9, pp. 1632-1646. URL: <Go to ISI>://WOS:000293693700001

[46] Lu, Y. and Ballauff, M. (2011): Thermosensitive core-shell microgels: From colloidal model systems to nanoreactors, Progress in Polymer Science (vol. 36), No. 6, pp. 767-792. URL: <Go to ISI>://WOS:000291134100003

[47] Schrinner, M.; Polzer, F.; Mei, Y.; Lu, Y.; Haupt, B.; Ballauff, M.; Goldel, A.; Drechsler, M.; Preussner, J. and Glatzel, U. (2007): Mechanism of the formation of amorphous gold nanoparticles within spherical polyelectrolyte brushes, Macromolecular Chemistry and Physics (vol. 208), No. 14, pp. 1542-1547. URL: <Go to ISI>://000248393500006

[48] Wunder, S.; Lu, Y.; Albrecht, M. and Ballauff, M. (2011): Catalytic Activity of Faceted Gold Nanoparticles Studied by a Model Reaction: Evidence for Substrate-Induced Surface Restructuring, Acs Catalysis (vol. 1), No. 8, pp. 908-916. URL: <Go to ISI>://WOS:000293488300010

[49] Wunder, S.; Polzer, F.; Lu, Y.; Mei, Y. and Ballauff, M. (2010): Kinetic Analysis of Catalytic Reduction of 4-Nitrophenol by Metallic Nanoparticles Immobilized in Spherical Polyelectrolyte Brushes, Journal of Physical Chemistry C (vol. 114), No. 19, pp. 8814-8820. URL: <Go to ISI>://WOS:000277500000019

[50] Lu, Y.; Mei, Y.; Schrinner, M.; Ballauff, M. and Moller, M. W. (2007): In situ formation of Ag nanoparticles in spherical polyacrylic acid brushes by UV irradiation, Journal of Physical Chemistry C (vol. 111), No. 21, pp. 7676-7681. URL: <Go to ISI>://000246695400020

[51] Schrinner, M.; Ballauff, M.; Talmon, Y.; Kauffmann, Y.; Thun, J.; Moller, M. and Breu, J. (2009): Single Nanocrystals of Platinum Prepared by Partial Dissolution of Au-Pt Nanoalloys, Science (vol. 323), No. 5914, pp. 617-620. URL: <Go to ISI>://WOS:000262862800038

[52] Lu, Yan; Mei, Yu; Schrinner, Marc; Ballauff, Matthias and Moeller, Michael W. (2007): In situ formation of Ag nanoparticles in spherical polyacrylic acid brushes by UV irradiation, Journal of Physical Chemistry C (vol. 111), No. 21, pp. 7676-7681. URL: <Go to ISI>://WOS:000246695400020

[53] Schrinner, M.; Proch, S.; Mei, Y.; Kempe, R.; Miyajima, N. and Ballauff, M. (2008): Stable bimetallic gold-platinum nanoparticles immobilized on spherical polyelectrolyte brushes: Synthesis, characterization, and application for the oxidation of alcohols, Advanced Materials (vol. 20), No. 10, pp. 1928-1933. URL: <Go to ISI>://WOS:000256846300020

[54] Yu, M.; Lu, Y.; Schrinner, M.; Polzer, E. and Ballauff, M. (2007): Spherical polyelectrolyte brushes as carriers for catalytically active metal nanoparticles, Macromolecular Symposia (vol. 254), pp. 42-45. URL: <Go to ISI>://WOS:000249160900007

[55] Guo, X.; Weiss, A. and Ballauff, M. (1999): Synthesis of spherical polyelectrolyte brushes by photoemulsion polymerization, Macromolecules (vol. 32), No. 19, pp. 6043-6046. URL: <Go to ISI>://WOS:000082765900008

[56] Baletto, F. and Ferrando, R. (2005): Structural properties of nanoclusters: Energetic, thermodynamic, and kinetic effects, Reviews of Modern Physics (vol. 77), No. 1, pp. 371-423. URL: <Go to ISI>://WOS:000229544100008

[57] Remita, S.; Mostafavi, M. and Delcourt, M. O. (1996): Bimetallic Ag-Pt and Au-Pt aggregates synthesized by radiolysis, Radiation Physics and Chemistry (vol. 47), No. 2, pp. 275-279. URL: <Go to ISI>://WOS:A1996TK58100019

[58] Bonnemann, H.; Endruschat, U.; Tesche, B.; Rufinska, A.; Lehmann, C. W.; Wagner, F. E.; Filoti, G.; Parvulescu, V. and Parvulescu, V. I. (2000): An SiO(2)-embedded nanoscopic Pd/Au alloy colloid, European Journal of Inorganic Chemistry, No. 5, pp. 819-822. URL: <Go to ISI>://WOS:000087022200003

[59] Nutt, M. O.; Hughes, J. B. and Wong, M. S. (2005): Designing Pd-on-Au bimetallic nanoparticle catalysts for trichloroethene hydrodechlorination, Environmental Science & Technology (vol. 39), No. 5, pp. 1346-1353. URL: <Go to ISI>://WOS:000227257400030

[60] Su, Ren; Tiruvalam, Ramchandra; He, Qian; Dimitratos, Nikolaos; Kesavan, Lokesh; Hammond, Ceri; Lopez-Sanchez, Jose Antonio; Bechstein, Ralf; Kiely, Christopher J.; Hutchings, Graham J. and Besenbacher, Flemming (2012): Promotion of Phenol Photodecomposition over TiO2 Using Au, Pd, and Au–Pd Nanoparticles, Acs Nano (vol. 6), No. 7, pp. 6284-6292. URL: http://dx.doi.org/10.1021/nn301718v

[61] Wei, X.; Yang, X. F.; Wang, A. Q.; Li, L.; Liu, X. Y.; Zhang, T.; Mou, C. Y. and Li, J. (2012): Bimetallic Au-Pd Alloy Catalysts for N2O Decomposition: Effects of Surface Structures on Catalytic Activity, Journal of Physical Chemistry C (vol. 116), No. 10, pp. 6222-6232. URL: <Go to ISI>://WOS:000301509600032

[62] Shao, M. W.; Wang, H.; Zhang, M. L.; Ma, D. D. D. and Lee, S. T. (2008): The mutual promotional effect of Au-Pd bimetallic nanoparticles on silicon nanowires: A study of preparation and catalytic activity, Applied Physics Letters (vol. 93), No. 24. URL: <Go to ISI>://WOS:000261896400063

[63] Baddeley, C. J.; Ormerod, R. M.; Stephenson, A. W. and Lambert, R. M. (1995): SURFACE-STRUCTURE AND REACTIVITY IN THE CYCLIZATION OF ACETYLENE TO BENZENE WITH PD OVERLAYERS AND PD/AU SURFACE ALLOYS ON AU(111), Journal of Physical Chemistry (vol. 99), No. 14, pp. 5146-5151. URL: <Go to ISI>://WOS:A1995QR22800039

[64] Baddeley, C. J.; Tikhov, M.; Hardacre, C.; Lomas, J. R. and Lambert, R. M. (1996): Ensemble effects in the coupling of acetylene to benzene on a bimetallic surface: A study with Pd{111}/Au, Journal of Physical Chemistry (vol. 100), No. 6, pp. 2189-2194. URL: <Go to ISI>://WOS:A1996TU97500033

[65] Lee, A. F.; Baddeley, C. J.; Hardacre, C.; Ormerod, R. M.; Lambert, R. M.; Schmid, G. and West, H. (1995): STRUCTURAL AND CATALYTIC PROPERTIES OF NOVEL AU/PD BIMETALLIC COLLOID PARTICLES - EXAFS, XRD, AND ACETYLENE COUPLING, Journal of Physical Chemistry (vol. 99), No. 16, pp. 6096-6102. URL: <Go to ISI>://WOS:A1995QU82800053

[66] Landon, Philip; Collier, Paul J.; Papworth, Adam J.; Kiely, Christopher J. and Hutchings, Graham J. (2002): Direct formation of hydrogen peroxide from H2/O2 using a gold catalyst, Chemical Communications, No. 18, pp. 2058-2059. URL: http://dx.doi.org/10.1039/B205248M

[67] Staykov, Aleksandar; Kamachi, Takashi; Ishihara, Tatsumi and Yoshizawa, Kazunari (2008): Theoretical Study of the Direct Synthesis of H2O2 on Pd and Pd/Au Surfaces, The Journal of Physical Chemistry C (vol. 112), No. 49, pp. 19501-19505. URL: http://dx.doi.org/10.1021/jp803021n

[68] Han, Yi-Fan; Zhong, Ziyi; Ramesh, Kanaparthi; Chen, Fengxi; Chen, Luwei; White, Tim; Tay, Qiuling; Yaakub, Siti Nurbaya and Wang, Zhan (2007): Au Promotional Effects on the Synthesis of H2O2 Directly from H2 and O2 on Supported Pd−Au Alloy Catalysts, The Journal of Physical Chemistry C (vol. 111), No. 24, pp. 8410-8413. URL: http://dx.doi.org/10.1021/jp072934g

[69] Ksar, F.; Ramos, L.; Keita, B.; Nadjo, L.; Beaunier, P. and Remita, H. (2009): Bimetallic Palladium-Gold Nanostructures: Application in Ethanol Oxidation, Chemistry of Materials (vol. 21), No. 15, pp. 3677-3683. URL: <Go to ISI>://WOS:000268523300028

[70] Chen, Y. T.; Lim, H. M.; Tang, Q. H.; Gao, Y. T.; Sun, T.; Yan, Q. Y. and Yang, Y. H. (2010): Solvent-free aerobic oxidation of benzyl alcohol over Pd monometallic and Au-Pd bimetallic catalysts supported on SBA-16 mesoporous molecular sieves, Applied Catalysis a-General (vol. 380), No. 1-2, pp. 55-65. URL: <Go to ISI>://WOS:000278504300008

[71] Wang, D.; Villa, A.; Spontoni, P.; Su, D. S. and Prati, L. (2010): In Situ Formation of Au-Pd Bimetallic Active Sites Promoting the Physically Mixed Monometallic Catalysts in the Liquid-Phase Oxidation of Alcohols, Chemistry-a European Journal (vol. 16), No. 33, pp. 10007-10013. URL: <Go to ISI>://WOS:000282156700011

[72] Marx, S. and Baiker, A. (2009): Beneficial Interaction of Gold and Palladium in Bimetallic Catalysts for the Selective Oxidation of Benzyl Alcohol, Journal of Physical Chemistry C (vol. 113), No. 15, pp. 6191-6201. URL: <Go to ISI>://WOS:000265030200047

[73] Hosseini, M.; Barakat, T.; Cousin, R.; Aboukais, A.; Su, B. L.; De Weireld, G. and Siffert, S. (2012): Catalytic performance of core-shell and alloy Pd-Au nanoparticles for total oxidation of VOC: The effect of metal deposition, Applied Catalysis B-Environmental (vol. 111), pp. 218-224. URL: <Go to ISI>://WOS:000300528500024

[74] Brett, G. L.; Miedziak, P. J.; Dimitratos, N.; Lopez-Sanchez, J. A.; Dummer, N. F.; Tiruvalam, R.; Kiely, C. J.; Knight, D. W.; Taylor, S. H.; Morgan, D. J.; Carleya, A. F.

and Hutchings, G. J. (2012): Oxidative esterification of 1,2-propanediol using gold and gold-palladium supported nanoparticles, Catalysis Science & Technology (vol. 2), No. 1, pp. 97-104. URL: <Go to ISI>://WOS:000299011200012

[75] Chen, M. S. and Goodman, D. W. (2008): Promotional Effects of Au in Pd-Au Catalysts for Vinyl Acetate Synthesis, Chinese Journal of Catalysis (vol. 29), No. 11, pp. 1178-1186. URL: <Go to ISI>://WOS:000261810800022

[76] Han, Y. F.; Wang, J. H.; Kumar, D.; Yan, Z. and Goodman, D. W. (2005): A kinetic study of vinyl acetate synthesis over Pd-based catalysts: kinetics of vinyl acetate synthesis over Pd-Au/SiO2 and Pd/SiO2 catalysts, Journal of Catalysis (vol. 232), No. 2, pp. 467-475. URL: <Go to ISI>://WOS:000229565500022

[77] Chen, M. S.; Kumar, D.; Yi, C. W. and Goodman, D. W. (2005): The promotional effect of gold in catalysis by palladium-gold, Science (vol. 310), No. 5746, pp. 291-293. URL: <Go to ISI>://WOS:000232670100045

[78] Li, Zhenjun; Gao, Feng; Wang, Yilin; Calaza, Florencia; Burkholder, Luke and Tysoe, Wilfred T. (2007): Formation and characterization of Au/Pd surface alloys on Pd(1 1 1), Surface Science (vol. 601), No. 8, pp. 1898-1908. URL: http://www.sciencedirect.com/science/article/pii/S0039602807001549

[79] Yi, C. W.; Luo, K.; Wei, T. and Goodman, D. W. (2005): The Composition and Structure of Pd−Au Surfaces, The Journal of Physical Chemistry B (vol. 109), No. 39, pp. 18535-18540. URL: http://dx.doi.org/10.1021/jp053515r

[80] Wei, Tao; Wang, Jinhai and Goodman, D. Wayne (2007): Characterization and Chemical Properties of Pd−Au Alloy Surfaces†, The Journal of Physical Chemistry C (vol. 111), No. 25, pp. 8781-8788. URL: http://dx.doi.org/10.1021/jp067177l

[81] Sellidj, Abdelkrim and Koel, Bruce E. (1994): Electronic and CO chemisorption properties of ultrathin Pd films vapor deposited on Au(111), Physical Review B (vol. 49), No. 12, pp. 8367-8376. URL: http://link.aps.org/doi/10.1103/PhysRevB.49.8367

[82] Ruff, Martin; Takehiro, Naoki; Liu, Ping; Nørskov, Jens K. and Behm, R. Jürgen (2007): Size-Specific Chemistry on Bimetallic Surfaces: A Combined Experimental and Theoretical Study, Chemphyschem (vol. 8), No. 14, pp. 2068-2071. URL: http://dx.doi.org/10.1002/cphc.200700070

[83] Xu, Jing; White, Tim; Li, Ping; He, Chongheng; Yu, Jianguo; Yuan, Weikang and Han, Yi-Fan (2010): Biphasic Pd−Au Alloy Catalyst for Low-Temperature CO Oxidation, Journal of the American Chemical Society (vol. 132), No. 30, pp. 10398-10406. URL: http://dx.doi.org/10.1021/ja102617r

[84] Luo, K.; Wei, T.; Yi, C. W.; Axnanda, S. and Goodman, A. W. (2005): Preparation and characterization of silica supported Au-Pd model catalysts, Journal of Physical Chemistry B (vol. 109), No. 49, pp. 23517-23522. URL: <Go to ISI>://WOS:000233864300060

[85] Pérez-Lorenzo, Moisés (2012): Palladium Nanoparticles as Efficient Catalysts for Suzuki Cross-Coupling Reactions, The Journal of Physical Chemistry Letters (vol. 3), No. 2, pp. 167-174. URL: http://dx.doi.org/10.1021/jz2013984

[86] Hashmi, A. S. K. (2007): Gold-catalyzed organic reactions, Chemical Reviews (vol. 107), No. 7, pp. 3180-3211. URL: <Go to ISI>://WOS:000247926600008

[87] Mondloch, J. E.; Bayram, E. and Finke, R. G. (2012): A review of the kinetics and mechanisms of formation of supported-nanoparticle heterogeneous catalysts, Journal of Molecular Catalysis a-Chemical (vol. 355), pp. 1-38. URL: <Go to ISI>://WOS:000300601000001

[88] Roucoux, A.; Schulz, J. and Patin, H. (2002): Reduced transition metal colloids: A novel family of reusable catalysts?, Chemical Reviews (vol. 102), No. 10, pp. 3757-3778. URL: <Go to ISI>://WOS:000178548800019

[89] Schmid, Günter (2004): Nanoparticles : from theory to application, 1. repr. ed., Wiley-VCH, Weinheim, ISBN: 3527305076 (Gb.). URL: http://www.loc.gov/catdir/description/wiley041/2004298992.html

[90] Barcikowski, S.; Devesa, F. and Moldenhauer, K. (2009): Impact and structure of literature on nanoparticle generation by laser ablation in liquids, Journal of Nanoparticle Research (vol. 11), No. 8, pp. 1883-1893. URL: <Go to ISI>://WOS:000271107400003

[91] Barsch, N.; Jakobi, J.; Weiler, S. and Barcikowski, S. (2009): Pure colloidal metal and ceramic nanoparticles from high-power picosecond laser ablation in water and acetone, Nanotechnology (vol. 20), No. 44. URL: <Go to ISI>://WOS:000270562900017

[92] Singh, S. C. and Zeng, H. B. (2012): Nanomaterials and Nanopatterns Based on Laser Processing: A Brief Review on Current State of Art, Science of Advanced Materials (vol. 4), No. 3-4, pp. 368-390. URL: <Go to ISI>://WOS:000305048500002

[93] Barcikowski, S.; Hahn, A.; Guggenheim, M.; Reimers, K. and Ostendorf, A. (2010): Biocompatibility of nanoactuators: stem cell growth on laser-generated nickel-titanium shape memory alloy nanoparticles, Journal of Nanoparticle Research (vol. 12), No. 5, pp. 1733-1742. URL: <Go to ISI>://WOS:000277956800020

[94] Taylor, U.; Klein, S.; Petersen, S.; Kues, W.; Barcikowski, S. and Rath, D. (2010): Nonendosomal Cellular Uptake of Ligand-Free, Positively Charged Gold Nanoparticles, Cytometry Part A (vol. 77A), No. 5, pp. 439-446. URL: <Go to ISI>://WOS:000277174000005

[95] Astruc, D.; Lu, F. and Aranzaes, J. R. (2005): Nanoparticles as recyclable catalysts: The frontier between homogeneous and heterogeneous catalysis, Angewandte Chemie-International Edition (vol. 44), No. 48, pp. 7852-7872. URL: <Go to ISI>://WOS:000234007700005

[96] Campelo, J. M.; Luna, D.; Luque, R.; Marinas, J. M. and Romero, A. A. (2009): Sustainable Preparation of Supported Metal Nanoparticles and Their Applications in Catalysis, Chemsuschem (vol. 2), No. 1, pp. 18-45. URL: <Go to ISI>://WOS:000263095600003

[97] Mohr, Christian; Hofmeister, Herbert; Radnik, Jörg and Claus, Peter (2003): Identification of Active Sites in Gold-Catalyzed Hydrogenation of Acrolein, Journal of the American Chemical Society (vol. 125), No. 7, pp. 1905-1911. URL: http://dx.doi.org/10.1021/ja027321q

[98] Su, Fang-Zheng; Liu, Yong-Mei; Wang, Lu-Cun; Cao, Yong; He, He-Yong and Fan, Kang-Nian (2008): Ga–Al Mixed-Oxide-Supported Gold Nanoparticles with Enhanced Activity for Aerobic Alcohol Oxidation, Angewandte Chemie (vol. 120), No. 2, pp. 340-343. URL: http://dx.doi.org/10.1002/ange.200704370

[99] Milone, C.; Tropeano, M. L.; Gulino, G.; Neri, G.; Ingoglia, R. and Galvagno, S. (2002): Selective liquid phase hydrogenation of citral on Au/Fe2O3 catalysts, Chemical Communications, No. 8, pp. 868-869. URL: http://dx.doi.org/10.1039/B201542K

[100] Taarning, Esben; Madsen, Anders Theilgaard; Marchetti, Jorge Mario; Egeblad, Kresten and Christensen, Claus Hviid (2008): Oxidation of glycerol and propanediols in methanol over heterogeneous gold catalysts, Green Chemistry (vol. 10), No. 4, pp. 408-414. URL: http://dx.doi.org/10.1039/B714292G

[101] Biella, Serena and Rossi, Michele (2003): Gas phase oxidation of alcohols to aldehydes or ketones catalysed by supported gold, Chemical Communications, No. 3, pp. 378-379. URL: http://dx.doi.org/10.1039/B210506C

[102] Hutchings, Graham J. (2008): Nanocrystalline gold and gold palladium alloy catalysts for chemical synthesis, Chemical Communications, No. 10, pp. 1148-1164. URL: http://dx.doi.org/10.1039/B712305C

[103] Haruta, Masatake (2002): Catalysis of Gold Nanoparticles Deposited on Metal Oxides, CATTECH (vol. 6), No. 3, pp. 102-115. URL: http://dx.doi.org/10.1023/A:1020181423055

[104] Willis, N. G. and Guzman, J. (2008): Influence of the support during homocoupling of phenylboronic acid catalyzed by supported gold, Applied Catalysis a-General (vol. 339), No. 1, pp. 68-75. URL: <Go to ISI>://WOS:000255455300009

[105] Vannice, M. A. (2005): Kinetics of Catalytic Reactions, Springer Science + Buisness Media: Philadelphia.

[106] Wedler, G. (1997): Lehrbuch der Physikalischen Chemie, Wiles-VCH.

[107] Sips, R. (1948): On the Structure of a Catalyst Surface Journal of Chemical Physics (vol. 16), No. 5, pp. 490-495. URL: http://jcp.aip.org/resource/1/jcpsa6/v16/i5/p490_s1

[108] Sarkar, Sougata; Sinha, Arun Kumar; Pradhan, Mukul; Basu, Mrinmoyee; Negishi, Yuichi and Pal, Tarasankar (2011): Redox Transmetalation of Prickly Nickel Nanowires for Morphology Controlled Hierarchical Synthesis of Nickel/Gold Nanostructures for Enhanced Catalytic Activity and SERS Responsive Functional Material, Journal of Physical Chemistry C (vol. 115), No. 5, pp. 1659-1673. URL: <Go to ISI>://WOS:000286868600040

[109] Zeng, Jie; Zhang, Qiang; Chen, Jingyi and Xia, Younan (2010): A Comparison Study of the Catalytic Properties of Au-Based Nanocages, Nanoboxes, and Nanoparticles, Nano Letters (vol. 10), No. 1, pp. 30-35. URL: <Go to ISI>://WOS:000273428700006

[110] Zhou, X.; Xu, W.; Liu, G.; Panda, D. and Chen, P. (2010): Size-dependent catalytic activity and dynamics of gold nanoparticles at the single-molecule level, J Am Chem Soc (vol. 132), No. 1, pp. 138-46. URL: http://www.ncbi.nlm.nih.gov/pubmed/19968305

[111] Ertl, G. (2002): Dynamics of surface reactions, Faraday Discussions (vol. 121), pp. 1-15. URL: <Go to ISI>://WOS:000177283000001

[112] Imbihl, R.; Cox, M. P. and Ertl, G. (1986): Kinetic Oscillations in the Catalytic Cooxidation on Pt(100) - Experiments, Journal of Chemical Physics (vol. 84), No. 6, pp. 3519-3534. URL: <Go to ISI>://A1986A369700078

[113] Somorjai, Gabor A. and Li, Yimin (2010): Introduction to surface chemistry and catalysis, 2. ed., Wiley, Hoboken, NJ, ISBN: 9780470508237 (cloth). URL: http://www.gbv.de/dms/bowker/toc/9780470508237.pdf

[114] Imbihl, R. and Ertl, G. (1995): Oscillatory Kinetics in Heterogeneous Catalysis, Chemical Reviews (vol. 95), No. 3, pp. 697-733. URL: <Go to ISI>://A1995QX74300012

[115] Jakubith, S.; Rotermund, H. H.; Engel, W.; Vonoertzen, A. and Ertl, G. (1990): Spatiotemporal Concentration Patterns in a Surface-Reaction - Propagating and Standing Waves, Rotating Spirals, and Turbulence, Physical Review Letters (vol. 65), No. 24, pp. 3013-3016. URL: <Go to ISI>://A1990EL84000024

[116] Pasteur, A. T.; Dixonwarren, S. J. and King, D. A. (1995): Hydrogen Dissociation on Pt(100) - Nonlinear Power-Law in Hydrogen-Induced Restructuring, Journal of Chemical Physics (vol. 103), No. 6, pp. 2251-2260. URL: <Go to ISI>://A1995RM53900028

[117] Hopkinson, A.; Bradley, J. M.; Guo, X. and King, D. A. (1993): Nonlinear island growth dynamics in adsorbate-induced restructuring of quasihexagonal reconstructed Pt{100} by CO, Phys Rev Lett (vol. 71), No. 10, pp. 1597-1600. URL: http://www.ncbi.nlm.nih.gov/pubmed/10054448

[118] van Beurden, P.; Bunnik, B. S.; Kramer, G. J. and Borg, A. (2003): Mechanism and dynamics of the CO-induced lifting of the Pt(100) surface reconstruction, Physical Review Letters (vol. 90), No. 6, p. 066106. URL: <Go to ISI>://WOS:000181015900031

[119] van Beurden, P. and Kramer, G. J. (2004): Atomistic mechanisms for the (1x1)reversible arrow hex surface phase transformations of Pt(100), Journal of Chemical Physics (vol. 121), No. 5, pp. 2317-2325. URL: <Go to ISI>://WOS:000222680900034

[120] Ochoa, M. A.; Zhou, X. C.; Chen, P. and Loring, R. F. (2011): Interpreting single turnover catalysis measurements with constrained mean dwell times, Journal of Chemical Physics (vol. 135), No. 17. URL: <Go to ISI>://WOS:000296733300024

[121] Bleloch, Andrew and Lupini, Andrew (2004): Imaging at the picoscale, Materials Today (vol. 7), No. 12, pp. 42-48. URL: http://www.sciencedirect.com/science/article/pii/S136970210400570X

[122] Hawkes, P. W. (2009): Aberration correction past and present, Philosophical Transactions of the Royal Society a-Mathematical Physical and Engineering Sciences (vol. 367), No. 1903, pp. 3637-3664. URL: <Go to ISI>://WOS:000269569400002

[123] Williams, David B. and Carter, C. Barry (1996): Transmission electron microscopy : a textbook for materials science, Springer, New York, NY [u.a.], ISBN: 030645324X (pbk. (set))

[124] Kawasaki, T.; Ichihashi, M.; Matsutani, T.; Kimura, Y. and Ikuta, T. (2008): Aberration analysis of Cs-corrector system with twin hexapoles and transfer lens doublet in scanning transmission electron microscope by simple ray tracing based on geometrical optics, Surface and Interface Analysis (vol. 40), No. 13, pp. 1732-1735. URL: <Go to ISI>://WOS:000262170000035

[125] Winter, H.; Durham, P. J.; Temmerman, W. M. and Stocks, G. M. (1986): Electronic density of states and the x-ray photoelectron spectra of the valence band of Cu-Pd alloys, Physical Review B (vol. 33), No. 4, pp. 2370-2379. URL: http://link.aps.org/doi/10.1103/PhysRevB.33.2370

[126] West, Anthony R. (1992): Grundlagen der Festkörperchemie, Verlag Chemie.

[127] Balerna, A.; Bernieri, E.; Picozzi, P.; Reale, A.; Santucci, S.; Burattini, E. and Mobilio, S. (1985): A STRUCTURAL INVESTIGATION ON SMALL GOLD CLUSTERS BY EXAFS, Surface Science (vol. 156), No. JUN, pp. 206-213. URL: <Go to ISI>://WOS:A1985AMF8200025

[128] Bunker, Grant (2010): Introduction to XAFS, Cambridge University Press.

[129] Fang, Y. L.; Miller, J. T.; Guo, N.; Heck, K. N.; Alvarez, P. J. J. and Wong, M. S. (2011): Structural analysis of palladium-decorated gold nanoparticles as colloidal bimetallic catalysts, Catalysis Today (vol. 160), No. 1, pp. 96-102. URL: <Go to ISI>://WOS:000286454100013

[130] Evangelisti, C.; Schiavi, E.; Aronica, L. A.; Caporusso, A. M.; Vitulli, G.; Bertinetti, L.; Martra, G.; Balerna, A. and Mobilio, S. (2012): Bimetallic Gold-Palladium vapour derived catalysts: The role of structural features on their catalytic activity, Journal of Catalysis (vol. 286), pp. 224-236. URL: <Go to ISI>://WOS:000300141300023

[131] Teng, X. W.; Wang, Q.; Liu, P.; Han, W.; Frenkel, A.; Wen, W.; Marinkovic, N.; Hanson, J. C. and Rodriguez, J. A. (2008): Formation of Pd/Au nanostructures from Pd nanowires via galvanic replacement reaction, Journal of the American Chemical Society (vol. 130), No. 3, pp. 1093-1101. URL: <Go to ISI>://WOS:000252426300055

[132] Knecht, M. R.; Weir, M. G.; Frenkel, A. I. and Crooks, R. M. (2008): Structural rearrangement of bimetallic alloy PdAu nanoparticles within dendrimer templates to yield core/shell configurations, Chemistry of Materials (vol. 20), No. 3, pp. 1019-1028. URL: <Go to ISI>://WOS:000252970800032

[133] Weir, M. G.; Knecht, M. R.; Frenkel, A. I. and Crooks, R. M. (2010): Structural Analysis of PdAu Dendrimer-Encapsulated Bimetallic Nanoparticles, Langmuir (vol. 26), No. 2, pp. 1137-1146. URL: <Go to ISI>://WOS:000273403400071

[134] Dash, P.; Bond, T.; Fowler, C.; Hou, W.; Coombs, N. and Scott, R. W. J. (2009): Rational Design of Supported PdAu Nanoparticle Catalysts from Structured Nanoparticle Precursors, Journal of Physical Chemistry C (vol. 113), No. 29, pp. 12719-12730. URL: <Go to ISI>://WOS:000268139800018

[135] Ketchie, W. C.; Murayama, M. and Davis, R. J. (2007): Selective oxidation of glycerol over carbon-supported AuPd catalysts, Journal of Catalysis (vol. 250), No. 2, pp. 264-273. URL: <Go to ISI>://WOS:000249564600008

[136] Krumeich, F.; Marx, S.; Baiker, A. and Nesper, R. (2011): Characterization of AuPd Nanoparticles by Probe-Corrected Scanning Transmission Electron Microscopy and X-ray Absorption Spectroscopy, Zeitschrift Fur Anorganische Und Allgemeine Chemie (vol. 637), No. 7-8, pp. 875-881. URL: <Go to ISI>://WOS:000292334400011

[137] Liu, F. and Zhang, P. (2010): Tailoring the local structure and electronic property of AuPd nanoparticles by selecting capping molecules, Applied Physics Letters (vol. 96), No. 4. URL: <Go to ISI>://WOS:000274179900065

[138] Benfield, R. E. (1992): MEAN COORDINATION NUMBERS AND THE NONMETAL METAL TRANSITION IN CLUSTERS, Journal of the Chemical Society-Faraday Transactions (vol. 88), No. 8, pp. 1107-1110. URL: <Go to ISI>://WOS:A1992HQ25500005

[139] Harada, M.; Asakura, K. and Toshima, N. (1993): CATALYTIC ACTIVITY AND STRUCTURAL-ANALYSIS OF POLYMER-PROTECTED AU/PD BIMETALLIC CLUSTERS PREPARED BY THE SUCCESSIVE REDUCTION OF HAUCL4 AND PDCL2, Journal of Physical Chemistry (vol. 97), No. 19, pp. 5103-5114. URL: <Go to ISI>://WOS:A1993LB80300042

[140] Hazra, D.; Datta, S.; Mondal, M.; Ghatak, J.; Satyam, P. V. and Gupta, A. K. (2008): Thickness dependent lattice expansion in nanogranular Nb thin films, Journal of Applied Physics (vol. 103), No. 10. URL: <Go to ISI>://WOS:000256303800056

[141] Kolska, Z.; Riha, J.; Hnatowicz, V. and Svorcik, V. (2010): Lattice parameter and expected density of Au nano-structures sputtered on glass, Materials Letters (vol. 64), No. 10, pp. 1160-1162. URL: <Go to ISI>://WOS:000277325700011

[142] Siegel, J.; Lyutakov, O.; Rybka, V.; Kolska, Z. and Svorcik, V. (2011): Properties of gold nanostructures sputtered on glass, Nanoscale Research Letters (vol. 6). URL: <Go to ISI>://WOS:000290525700020

[143] Szczerba, W.; Riesemeier, H. and Thunemann, A. F. (2010): Bond length contraction in gold nanoparticles, Analytical and Bioanalytical Chemistry (vol. 398), No. 5, pp. 1967-1972. URL: <Go to ISI>://WOS:000283244500017

[144] Nanda, K. K.; Maisels, A. and Kruis, F. E. (2011): Evolution of crystallinity of free gold agglomerates and shape transformation, Rsc Advances (vol. 1), No. 4, pp. 568-572. URL: <Go to ISI>://WOS:000295869400002

[145] Nanda, K. K.; Maisels, A.; Kruis, F. E.; Fissan, H. and Stappert, S. (2003): Higher surface energy of free nanoparticles, Physical Review Letters (vol. 91), No. 10. URL: <Go to ISI>://WOS:000185485700029

[146] Nanda, K. K.; Maisels, A.; Kruis, F. E.; Fissan, H. and Stappert, S. (2004): Comment on "Higher surface energy of free nanoparticles" - Reply, Physical Review Letters (vol. 92), No. 17. URL: <Go to ISI>://WOS:000221179200072

[147] Nanda, K. K.; Maisels, A.; Kruis, F. E. and Rellinghaus, B. (2007): Anomalous thermal behavior of gold nanostructures, Epl (vol. 80), No. 5. URL: <Go to ISI>://WOS:000251647900017

[148] Vanithakumari, S. C. and Nanda, K. K. (2006): Phenomenological predictions of cohesive energy and structural transition of nanoparticles, Journal of Physical Chemistry B (vol. 110), No. 2, pp. 1033-1037. URL: <Go to ISI>://WOS:000234699200060

[149] Xie, D.; Wang, M. P. and Cao, L. F. (2005): A simplified model to calculate the higher surface energy of free-standing nanocrystals, Physica Status Solidi B-Basic Solid State Physics (vol. 242), No. 8, pp. R76-R78. URL: <Go to ISI>://WOS:000230564800004

[150] MacDonald, M. A.; Chevrier, D. M.; Zhang, P.; Qian, H. F. and Jin, R. C. (2011): The Structure and Bonding of Au(25)(SR)(18) Nanoclusters from EXAFS: The Interplay of Metallic and Molecular Behavior, Journal of Physical Chemistry C (vol. 115), No. 31, pp. 15282-15287. URL: <Go to ISI>://WOS:000293419700022

[151] Simoes, M.; Baranton, S. and Coutanceau, C. (2009): Electrooxidation of Sodium Borohydride at Pd, An, and Pd(x)Au(1-x) Carbon-Supported Nanocatalysts, Journal of Physical Chemistry C (vol. 113), No. 30, pp. 13369-13376. URL: <Go to ISI>://WOS:000268233800065

[152] Okamoto, Subramanian, Kacpraz (1992): Binary Alloy Phase Diagrams, 2nd ed. ASM International Materials Park, PH, Vol.1.

[153] Leppert, L. and Kummel, S. (2011): The Electronic Structure of Gold-Platinum Nanoparticles: Collecting Clues for Why They Are Special, Journal of Physical Chemistry C (vol. 115), No. 14, pp. 6694-6702. URL: <Go to ISI>://WOS:000289215400069

[154] Pittaway, F.; Paz-Borbon, L. O.; Johnston, R. L.; Arslan, H.; Ferrando, R.; Mottet, C.; Barcaro, G. and Fortunelli, A. (2009): Theoretical Studies of Palladium-Gold Nanoclusters: Pd-Au Clusters with up to 50 Atoms, Journal of Physical Chemistry C (vol. 113), No. 21, pp. 9141-9152. URL: <Go to ISI>://WOS:000266390100020

[155] Gaspari, R.; Pignedoli, C. A.; Fasel, R.; Treier, M. and Passerone, D. (2010): Atomistic insight into the adsorption site selectivity of stepped Au(111) surfaces, Physical Review B (vol. 82), No. 4. URL: <Go to ISI>://WOS:000280174200003

[156] Tao, F. and Salmeron, M. (2011): In Situ Studies of Chemistry and Structure of Materials in Reactive Environments, Science (vol. 331), No. 6014, pp. 171-174. URL: <Go to ISI>://WOS:000286433100030

[157] Barnard, A. S. and Chang, L. Y. (2011): Thermodynamic Cartography and Structure/Property Mapping of Commercial Platinum Catalysts, Acs Catalysis (vol. 1), No. 2, pp. 76-81. URL: <Go to ISI>://WOS:000289456900002

[158] Jakobi, J.; Menendez-Manjon, A.; Chakravadhanula, V. S. K.; Kienle, L.; Wagener, P. and Barcikowski, S. (2011): Stoichiometry of alloy nanoparticles from laser ablation of PtIr in acetone and their electrophoretic deposition on PtIr electrodes, Nanotechnology (vol. 22), No. 14. URL: <Go to ISI>://WOS:000287970000009

[159] Murugadoss, A. and Chattopadhyay, A. (2008): Surface area controlled differential catalytic activities of one-dimensional chain-like arrays of gold nanoparticles, Journal of Physical Chemistry C (vol. 112), No. 30, pp. 11265-11271. URL: <Go to ISI>://000257927100030

[160] Kuroda, Kyoko; Ishida, Tamao and Haruta, Masatake (2009): Reduction of 4-nitrophenol to 4-aminophenol over Au nanoparticles deposited on PMMA, Journal of Molecular Catalysis a-Chemical (vol. 298), No. 1-2, pp. 7-11. URL: <Go to ISI>://WOS:000262882100002

[161] Lu, Y.; Yuan, J. Y.; Polzer, F.; Drechsler, M. and Preussners, J. (2010): In Situ Growth of Catalytic Active Au - Pt Bimetallic Nanorods in Thermoresponsive Core - Shell Microgels, Acs Nano (vol. 4), No. 12, pp. 7078-7086. URL: <Go to ISI>://WOS:000285449100007

[162] Liu, J. C.; Qin, G. W.; Raveendran, P. and Kushima, Y. (2006): Facile "green" synthesis, characterization, and catalytic function of beta-D-glucose-stabilized Au nanocrystals, Chemistry-a European Journal (vol. 12), No. 8, pp. 2132-2138. URL: <Go to ISI>://WOS:000236090400002

[163] Wang, Y.; Wei, G. W.; Zhang, W. Q.; Jiang, X. W.; Zheng, P. W.; Shi, L. Q. and Dong, A. J. (2007): Responsive catalysis of thermoresponsive micelle-supported gold

nanoparticles, Journal of Molecular Catalysis a-Chemical (vol. 266), No. 1-2, pp. 233-238. URL: <Go to ISI>://000245672000035

[164] Zhang, Mingming; Liu, Li; Wu, Chenglin; Fu, Guoqi; Zhao, Hanying and He, Binglin (2007): Synthesis, characterization and application of well-defined environmentally responsive polymer brushes on the surface of colloid particles, Polymer (vol. 48), No. 7, pp. 1989-1997. URL: <Go to ISI>://WOS:000245532100020

[165] Han, Jie; Li, Liya and Guo, Rong (2010): Novel Approach to Controllable Synthesis of Gold Nanoparticles Supported on Polyaniline Nanofibers, Macromolecules (vol. 43), No. 24, pp. 10636-10644. URL: <Go to ISI>://WOS:000285429400063

[166] Panigrahi, S.; Basu, S.; Praharaj, S.; Pande, S.; Jana, S.; Pal, A.; Ghosh, S. K. and Pal, T. (2007): Synthesis and size-selective catalysis by supported gold nanoparticles: Study on heterogeneous and homogeneous catalytic process, Journal of Physical Chemistry C (vol. 111), No. 12, pp. 4596-4605. URL: <Go to ISI>://WOS:000245084100021

[167] Couves, J. W. and Meehan, P. (1995): COMBINED XANES AND EXAFS ANALYSIS OF SUPPORTED BIMETALLIC CATALYSTS, Physica B (vol. 208), No. 1-4, pp. 665-667. URL: <Go to ISI>://WOS:A1995QP96100264

[168] Qi, W. H. and Wang, M. P. (2005): Size and shape dependent lattice parameters of metallic nanoparticles, Journal of Nanoparticle Research (vol. 7), No. 1, pp. 51-57. URL: <Go to ISI>://WOS:000228501800005

[169] Huang, Z. X.; Thomson, P. and Di, S. L. (2007): Lattice contractions of a nanoparticle due to the surface tension: A model of elasticity, Journal of Physics and Chemistry of Solids (vol. 68), No. 4, pp. 530-535. URL: <Go to ISI>://WOS:000246739300008

[170] Tsunoyama, H.; Sakurai, H.; Ichikuni, N.; Negishi, Y. and Tsukuda, T. (2004): Colloidal gold nanoparticles as catalyst for carbon-carbon bond formation: Application to aerobic homocoupling of phenylboronic acid in water, Langmuir (vol. 20), No. 26, pp. 11293-11296. URL: <Go to ISI>://WOS:000225816800003

[171] Miller, J. T.; Kropf, A. J.; Zha, Y.; Regalbuto, J. R.; Delannoy, L.; Louis, C.; Bus, E. and van Bokhoven, J. A. (2006): The effect of gold particle size on Au-Au bond length and reactivity toward oxygen in supported catalysts, Journal of Catalysis (vol. 240), No. 2, pp. 222-234. URL: <Go to ISI>://WOS:000237689900014

[172] Solliard, C. and Flueli, M. (1985): SURFACE STRESS AND SIZE EFFECT ON THE LATTICE-PARAMETER IN SMALL PARTICLES OF GOLD AND PLATINUM, Surface Science (vol. 156), No. JUN, pp. 487-494. URL: <Go to ISI>://WOS:A1985AMF8200059

[173] Lamber, R.; Wetjen, S.; Schulzekloff, G. and Baalmann, A. (1995): METAL-CLUSTERS IN PLASMA POLYMER MATRICES - COLD CLUSTERS, Journal of Physical Chemistry (vol. 99), No. 38, pp. 13834-13838. URL: <Go to ISI>://WOS:A1995RW49900014

[174] Lin, C. M.; Hung, T. L.; Huang, Y. H.; Wu, K. T.; Tang, M. T.; Lee, C. H.; Chen, C. T. and Chen, Y. Y. (2007): Size-dependent lattice structure of palladium studied by x-ray absorption spectroscopy, Physical Review B (vol. 75), No. 12. URL: <Go to ISI>://WOS:000245330200103

[175] Lamber, R.; Wetjen, S. and Jaeger, N. I. (1995): SIZE DEPENDENCE OF THE LATTICE-PARAMETER OF SMALL PALLADIUM PARTICLES, Physical Review B (vol. 51), No. 16, pp. 10968-10971. URL: <Go to ISI>://WOS:A1995QW28400078

[176] Cluskey, P. D.; Newport, R. J.; Benfield, R. E.; Gurman, S. J. and Schmid, G. (1993): AN EXAFS STUDY OF SOME GOLD AND PALLADIUM CLUSTER COMPOUNDS, Zeitschrift Fur Physik D-Atoms Molecules and Clusters (vol. 26), pp. S8-S11. URL: <Go to ISI>://WOS:A1993ME19000004

[177] Ballauff, M. (2007): Spherical polyelectrolyte brushes, Progress in Polymer Science (vol. 32), No. 10, pp. 1135-1151. URL: <Go to ISI>://WOS:000250640200001

7.2 List of Figures

7.3 List of Tables

7.4 Abbreviations

SPB	Spherical Polyelectrolyte Brushes
AuPd@SPB	gold-palladium nanoalloys stabilized in SPB
Au@SPB	gold nanoparticles stabilized in SPB; (analogous Pd@SPB and Pt@SPB for Pd and Pt nanoparticles, respectively.)
TEM	transmission electron microscopy
HR-TEM	high resolution transmission electron microscopy
XAS	X-ray absorption spectroscopy
EXAFS	extended X-ray absorption fine structure
PAEMH	poly(2-aminoethyl methacrylate hydrochloride)
PSS	poly(styrene sulfonate)
UV-Vis	ultraviolet – visible (spectroscopy)
A	absorption
A_0	initial absorption
t	time
t_0	induction period
$t_{0,sp}$	spontaneous surface restructuring
FT	Fourier transform
FFT	fast Fourier transform
$<NN>$	mean coordination number
$N^{-1/3}$	inverse particle radius
N	total number of atoms
A-A bonds	bonds between atoms of the element *A*
B-B bonds	bonds between atoms of the element *B*
A-B bonds	bonds between the elements *A* and *B*

θ	surface coverage ($\theta_A\theta_B$ surface coverage by *A* and *B*)
θ_{Nip}	surface coverage by 4-nitrophenol
K	equilibrium constant (K_A and K_A for *A* and *B*, respectively)
[*A*]	concentration of *A*
[*B*]	concentration of *B*
r	reaction rate
k	kinetic constant
k_1	surface reduced rate constant
k_n	catalytic rate constant normalized by the number of particles per unit volume
S	surface
k_{app}	apparent rate constant
n, m	Freundlich exponents
r	radius
C_s	spherical aberration constant
α	angle of electron rays before crossing the lens
DOS	density of states
LUMO	lowest unoccupied molecule orbital
HOMO	highest occupied molecule orbital
CN	coordination number
fcc	face centered cubic
$N_{Me1\text{-}Me2}$	number of bonds between Me1 (metal 1) and Me2 (metal 2) at the Me1 absorption edge
$N_{Me1\text{-}Me1}$	number of bonds between atoms of Me1 (metal 1) at the Me1 absorption edge
$N_{Me2\text{-}Me1}$	number of bonds between Me1 (metal 1) and Me2 (metal 2) at the Me2 absorption edge

$N_{Me2\text{-}Me2}$	number of bonds between atoms of Me2 (metal 2) at the Me2 absorption edge
N_{total}	sum of all numbers of bonds at one absorption edge
AEMH	2-aminoethylmethacrylate hydrochloride
$HAuCl_4$	tetrachloroauric acid
Na_2PdCl_4	sodium tetrachloropalladate
$NaBH_4$	sodium borohydride
BH_4^-	borohydride
Nip	4-nitrophenol
Amp	4-aminophenol
PXRD	powder X-ray diffraction
EDX	energy disperse X-ray spectroscopy
Au_{core}-Pd_{shell}	alloy structure where Au is the core and Pd is the shell
Pd_{core}-Au_{shell}	alloy structure where Pd is the core and Au is the shell
$Au_{75}Pd_{25}$	AuPd nanoalloy of the molar ratio 75:25 (Au:Pd)
$Au_{50}Pd_{50}$	AuPd nanoalloy of the molar ratio 50:50 (Au:Pd)
$Au_{25}Pd_{75}$	AuPd nanoalloy of the molar ratio 25:75 (Au:Pd)
TGA	thermal gravimetric analysis
c(Nip), c_{Nip}	concentration of 4-nitrophenol
c(Amp), c_{Amp}	concentration of 4-aminophenol
K_{Nip}	adsorption constant of 4-nitrophenol
K_{BH4}	adsorption constant of 4-aminophenol
R	interatomic distance
σ^2	Debye-Waller factor
ΔE_0	inner core correction
wt-%	weight percent

mol-%	molar percent
d	diameter
I	intensity of beam
I_0	intensity of the incident beam

7.5 Publications

“Catalytic Activity of Nanoalloys from Gold and Palladium” J. Kaiser, L. Leppert, H. Welz, F. Polzer, S. Wunder, N. Wanderka, M. Albrecht, T. Lunkenbein, J. Breu, S. Kummel, Y. Lu and M. Ballauff,*Phys. Chem. Chem. Phys.*, **2012**, 14, 6487-6495.

“Thermosensitive Au-PNIPA Yolk-Shell Nanoparticles with Tunable Selectivity for Catalysis” S. Wu, J. Dzubiella, J. Kaiser, M. Drechsler, X. H. Guo, M. Ballauff and Y. Lu, *Angew. Chem.-Int. Edit.*, **2012**, 51, 2229-2233.

“Recoverable Platinum Nanocatalysts Immobilized on Magnetic Spherical Polyelectrolyte Brushes” S. Wu, J. Kaiser, X. H. Guo, L. Li, Y. Lu and M. Ballauff, *Ind. Eng. Chem. Res*, **2012**, 51, 5608-5614.

“Synthesis and Characterization of Monodisperse Thermosensitive Dumbbell-Shaped Microgels”F. Chu, M. Siebenbürger,F.Polzer,C. Stolze,J. Kaiser,M. Hoffmann, N.Heptner,J. Dzubiella,M. Drechsler,Y. Lu and M. Ballauff, *Macromol. Rapid Commun.*,**2012**, 33 (12), 1084-1084.

Talks at Conferences:

“EXAFS studies on gold-palladium nanoalloys stabilized on spherical polyelectrolyte brushes”*HyMa (Hybrid Materials), Strasbourg,* **March 2011.**

“Studies on Gold-Palladium Nanoalloys Stabilized on Spherical Polyelectrolyte Brushes” *ECIS (European Colloid and Interface Society), Berlin,***September 2012.**

“Catalytic Activity of Gold-Palladium Nanoalloys immobilized in Spherical Polyelectrolyte Brushes”*ICC (International Congress on Catalysis),* **July, 2012.**

8. Acknowledgement

This work only has been possible with the help of many people. They have inspired me and often brought me back on my way.

First of all, I would like to thank my supervisor Prof. Dr. Matthias Ballauff for the opportunity to work in his group, for the fascinating topic, for advice, support, motivation and scientific guidance.

Furthermore I would like to thank my group leader Dr. Yan Lu. During my whole work she has always been supporting me with helpful discussions and solutions about any questions concerning scientific as well as organizational topics.

Moreover, I would like to thank Dr. Martin Albrecht for HR-TEM measurements and Dr. Nelia Wanderka and Andreas Ott for TEM measurements. Especially for the kind introduction to TEM measurements I would like to thank Dr. Nelia Wanderka.

Great thanks go to the people who supported me during EXAFS measurements and data evaluation. Especially my colleagues Stefanie Wunder, Fangfang Chu,Dr. Yan Lu, Dr. Gerald Zehl and Andreas Kratzig who attended several days for EXAFS measurements in Hamburg at DESY at several beam-times. I would like thank the beamline scientists Dr. Michael Murphy (DESY, X-beamline), Dr. Vladimir Vidal (BESSY, KMC2) and the cooperation partners at the BAM, Dr. Wojciech Szczerba, Dr. Heinrich Riesemeier, Dr. Uwe Reinholz and Dr. Martin Radtke (BESSY, BAMline). Special thanks go to Dr. Wojciech Szczerba and Dr. Gerald Zehl for great support during EXAFS data evaluation.

For fabrication of support-free gold nanoparticles and discussions about this topic I would like to thank Dr. Philipp Wagener and Prof. Dr. Stephan Barcikowski from the University of Duisburg-Essen.

Furthermore I would like to thank the cooperation partners at the University of Bayreuth: Linn Leppert and Prof. Dr. Stephan Kümmel for the DOS calculations and the theory studies about AuPd nanoalloys, Dr. Thomas Lunkenbein for PXRD analyses and Hannes Welz for pre-work on AuPd@SPB nanoalloys.

I would like to thank all my colleagues at the Helmholtz-Zentrum Berlin for providing a very pleasant working environment, especially the colleagues who shared the same office with me together: Dr. Miriam Siebenbürger and Stefanie Wunder. Special thanks go to Stefanie Wunder for discussions about catalysis and for TGA measurements.

Of course, great thanks go to my family! To my parents, Rita and Klaus for support during my whole life and making all that possible. Furthermore I would like to thank my brothers, Peter and Theo, my sister in law Manuela and my nephew Daniel for mental support and for a nice time whenever I have been with them. Infinite thanks go to my girlfriend Eva-Maria Bauer for moving with me to Berlin and for great mental support and patience. Furthermore I would like to thank my friends Stephan Dankesreiter, Johannes Franz, Andreas Kerscher, Nicole Welsch, André Althoff and Thorsten Pröhl.Thank you for all the fun we had togetherbesides work and for keeping me grounded.

9. Declaration / Selbstständigkeitserklärung

Hiermit erkläre ich die vorliegende Arbeit selbst verfasst und nur unter Zuhilfenahme der angegebenen Hilfsmittel angefertigt zu haben.

Ferner erkläre ich, dass ich nicht anderweitig mit oder ohne Erfolg versucht habe, eine Dissertation einzureichen oder mich einer Doktorprüfung zu unterziehen.

Berlin, den 25.09.2012

Julian Kaiser